Bachelor Thesis

Degree Project in
Geological Sciences, 15 hp

Model-based evaluation of the ocean circulation and climate of the mid-Cretaceous

Nils Chabloz

Stockholm 2026

Department of Geological Sciences
Stockholm University
SE-106 91 Stockholm

Abstract

The mid-Cretaceous was a warm greenhouse interval characterised by the absence of large ice sheets, weak latitudinal temperature gradients, high atmospheric CO_2 and recurrent Oceanic Anoxic Events (OAEs). This thesis evaluates the ocean circulation and climate of three mid-Cretaceous stages, the Barremian (∼127 Ma), the Albian (∼106 Ma) and the Cenomanian (∼96 Ma), through coupled ocean-atmosphere simulations performed with the CESM1.2 model and compared against a pre-industrial control. Atmospheric CO_2 is fixed at 854 ppm across the three Cretaceous runs, so that inter-stage differences arise from non-CO_2 forcings, primarily palaeogeography. The simulations reproduce a warming from the Barremian to the Cenomanian despite constant CO_2, indicating a palaeogeographic contribution to the mid-Cretaceous warming trend. The simulated mid-Cretaceous ocean operates in a circulation regime considerably different from the pre-industrial: deep water forms along the Antarctic coast rather than in the North Atlantic, no Antarctic Circumpolar Current develops in the absence of a continuous circumpolar band, and a broad equatorial current connects the Tethys and Pacific Oceans. The deep ocean is globally older and less ventilated, with a saline, poorly ventilated proto-North Atlantic providing conditions favourable to the development of OAEs. Over the wide equatorial Pacific, stronger easterlies drive enhanced upwelling, a dip in equatorial sea surface temperature and a low-level anti-Hadley cell. The simulated poles nevertheless retain snow and sea ice, contradicting proxy evidence for ice-free poles. These results identify continental configuration as the primary control on inter-stage climate differences during the mid-Cretaceous.

Acknowledgements

I would like to thank my supervisor Agatha de Boer (Department of Geological Sciences, Stockholm University) for her continued guidance and feedback throughout this project, and Martin Renoult (Department of Geological Sciences, Stockholm University) for providing the model runs and essential information concerning the model. I am truly grateful to Lisa Robertson for taking time for proofreading and for providing corrections. Finally, I would like to thank Gunilla Cevey and Charlotte Roure for their never-ending support.

Table of Contents

List of Figures

1 Introduction

Spanning 143.1 to 66.0 million years ago ("International Chronostratigraphic Chart", 2026), the Cretaceous was the longest period of the Phanerozoic Eon. It was a time of considerably warmer climate than the present day, characterised by recurrent greenhouse conditions (Lunt et al., 2016; O'Brien et al., 2017; Scotese et al., 2021), and ended with one of the great mass extinctions: the Cretaceous-Palaeogene (K-Pg) extinction event (Scotese et al., 2021). The climate of this period was greatly different from today's, with, for instance, the presence of tropical plants and dinosaurs on Antarctica (Cantrill & Poole, 2012). The mid-Cretaceous witnessed the formation of the Atlantic Ocean as the break-up of Pangaea continued. At the same time, the Pacific Ocean was connected to the Tethys, and Australia was still linked to Antarctica. Changes in ocean circulation, such as variations in mixed-layer depth or overturning stream function, have been linked to large regional temperature anomalies across stages (Lunt et al., 2016). The mid-Cretaceous deep-water production differed greatly from today (Ladant et al., 2020), affecting the whole ocean circulation. Different models show different locations for deep-water formation that can be explained by different factors, such as the model palaeogeography (Lunt et al., 2016). This thesis presents a comparison of the inter-stage evolutions and differences between the Barremian ($\sim$127 Ma), the Albian ($\sim$106 Ma), the Cenomanian ($\sim$96 Ma) and a pre-industrial control (1850 CE). This analysis is guided by three questions: why is the mid-Cretaceous a period of interest, how does its climate compare with that of the present day, and how do the simulations compare with the existing literature? To the author's knowledge, this is among the highest resolution ocean-atmosphere coupled simulations of the stages of interest to date, which may provide insights into the mechanisms of the mid-Cretaceous climate, the interactions between the atmosphere and the oceans, and a foundation for future studies. Understanding those dynamics is an important part of evaluating the climate response to changes in ocean and atmospheric behaviours. In this thesis, we will first explore the results of the atmosphere, with its thermal (Section 4.1) and wind patterns (Section 4.2). We then proceed with an analysis of the ocean state in Section 5. In Section 5.1 we evaluate oceanic temperature patterns, then examine precipitation, evaporation, and salinity of the oceans in Section 5.2. Section 5.3 investigates the mixed layer depth, and oceanic gyres are evaluated in Section 5.4, followed by the ideal age of the oceans in Section 5.5. Finally, the thesis completes the analysis with a summary and interpretation of the main insights in Section 6.

2 Methods

2.1 The CESM simulations

The simulations were provided by Martin Renoult (Department of Geological Sciences, Stockholm University, Stockholm, Sweden), and they were produced following a protocol described for Miocene simulations in Renoult et al. (Accepted). The land-sea mask is provided by Getech Plc. The climate of the four periods of interest were simulated using the Community Earth System Model version 1.2 (CESM1.2) climate model, a model combining the ocean POP2 model with a 1° horizontal grid and 60 vertical levels, the atmosphere CAM4 model with a horizontal grid of 1.9° by 2.5° with 26 vertical layers, the CICE4 sea-ice model, the RTM river run-off model and the CLM2 land model. The CESM1.2 model allows for easier geographical adaptations of land and sea distribution, allowing the simulations to represent the continental layout of the Barremian, Albian, Cenomanian and pre-industrial. The three mid-Cretaceous simulation's CO_2 levels are set to a greenhouse concentration of 854 parts per million (ppm), three times the estimated concentration for the pre-industrial reference simulation. The solar forcing is 1346.32, 1348.28, 1349.4, and 1360.9 W/m^2 for the Barremian, Albian, Cenomanian and pre-industrial respectively. Setting the CO_2 concentration at the same level for the mid-Cretaceous simulations highlights the non-CO_2 forcings of the climate. Each of the mid-Cretaceous simulations was run for 3000 simulated years to reach a state of near equilibrium. The time slices have two output files in the NetCDF format, which is "commonly used to store and access multi-dimensional gridded data" (Loeb & Gnegy, 2024): one containing atmospheric variables and the other containing oceanic variables. These variables are averages over the last 100 years of the simulation in order to get a climatological mean state.

2.2 Data plotting

All data processing and visualisation were carried out in Python 3 within Jupyter notebooks, using a dedicated Conda environment. The core libraries used were `Xarray` for loading and handling the NetCDF datasets, `NumPy` for numerical operations, `Matplotlib` and `CartoPy` for map projections and spatial plots, `Cmocean` for colourmaps, and `Pandas` for statistics. Spatial distributions of ocean variables were visualized using a custom Python function, designed to produce standardized four-panel figures for cross-simulation comparison. Each panel corresponds to one of the four time slices: the Barremian (∼127 Ma), Albian (∼106 Ma), and Cenomanian (∼96 Ma) simulations, and the pre-industrial control (PI Control, 1850 CE). For each simulation, the target variable is extracted from its ocean dataset, optionally sliced at a specified depth level for three-dimensional fields, and converted to physically meaningful units if required (for example, mixed-layer depth variables are scaled from centimetres to metres). A cyclic point is appended to both the ocean variable and the corresponding atmospheric land fraction field to avoid longitudinal errors caused by global projections. Fields are rendered in an adapted projection centred on 180° or 0° longitude using either `contourf` or `pcolormesh`. The coastline geometry is derived from each simulation's land fraction field (`LANDFRAC`), ensuring that the displayed coastlines reflect the palaeogeographic configuration of the corresponding period. A single shared colorbar is placed with all panels to facilitate direct visual comparison across simulations. An adapted version of this function was made to show the atmospheric variables, based on the same principle.

3 Background

3.1 The Mid-Cretaceous

Barremian	Albian	Cenomanian
~19.5 °C	~21 °C	~24 °C

Table 1: Global average temperature from proxy data, adapted from Scotese et al. (2021). The author obtained these values by combining estimates of the changes in pole-to-Equator temperature from lithologic indicators of climate and estimates of tropical changes in temperature from oxygen isotopes

Our period of interest, the mid-Cretaceous, is globally described by its warm greenhouse climate, the absence of large ice sheets, weak latitudinal temperature gradients, high CO_2 concentrations (with the highest values during the mid-Cretaceous, ranging from 1000 to 2000 ppm) and was characterised by warm deep oceans (Huber et al., 1995; O'Brien et al., 2017; Scotese et al., 2021). The first Cretaceous time slice of interest is the Barremian, ranging from 125 to 121 million years ago ("International Chronostratigraphic Chart", 2026). Estimates of sea surface temperature from proxy records, reconstructed from $\delta^{18}O$ and TEX_{86}, a geochemical proxy based on the response of the membrane lipids of marine pelagic prokaryotes preserved in sediments, ranges from 35-40 °C for lower latitudes (<30°) to 25-30 °C for higher latitudes (>48°), and estimations of ~35 °C for the proto-North Atlantic for the Barremian (O'Brien et al., 2017). During the second interval of this study, the Albian (113 to 100 million years ago) ("International Chronostratigraphic Chart", 2026) sea surface temperatures are estimated to have peaked at approximately 32-33 °C. The early Albian was characterized by at least three Oceanic Anoxic Events (OAEs): the North Atlantic to Western Tethys "Paquier" anoxic event (OAE1b) (~111 Ma), the "Amadeus" event (OAE1c) and, later, the "Breistroffer" global anoxic event (OAE1d) (~99 Ma) (Scotese et al., 2021; Wilson & Norris, 2001). These events reflect episodes of widespread low levels of oxygen in the ocean, leading to the deposition of organic-rich black shales in the sedimentary record, and are thought to result from a combination of high temperatures, enhanced nutrient levels and reduced ventilation of deeper water masses (Donnadieu et al., 2016). At higher latitudes (48°

and above), proxy data indicates a minimum sea surface temperature of over 13 °C, with average estimates of approximately 15-20 °C for these higher latitudes and approximately 25 °C for latitudes below 30° (O'Brien et al., 2017). Finally, the Cenomanian, an age spanning 100 to 93 million years ago ("International Chronostratigraphic Chart", 2026), was the warmest Cretaceous interval and formed part of the Cenomanian-Turonian Thermal Maximum (~94-93 Ma), with global atmospheric temperature peaking at 28 °C, a minimal pole-to-equator gradient, and no ice sheets (Scotese et al., 2021). The warmest sea surface temperatures also occur during the late Cenomanian, with maximum SSTs over 35 °C and proxy data indicating low latitude temperatures of 30-35 °C and high latitude temperatures of 20-25 °C (O'Brien et al., 2017). The Cenomanian was characterized by the Cenomanian-Turonian OAE (OAE 2) (approximately 93 Ma) (Wilson & Norris, 2001), one of the most significant disruptions in the carbon cycle in Earth's history, with proxies suggesting anoxia in the Tethys and the Atlantic Ocean (Takashima et al., 2011).

3.2 Continental configuration

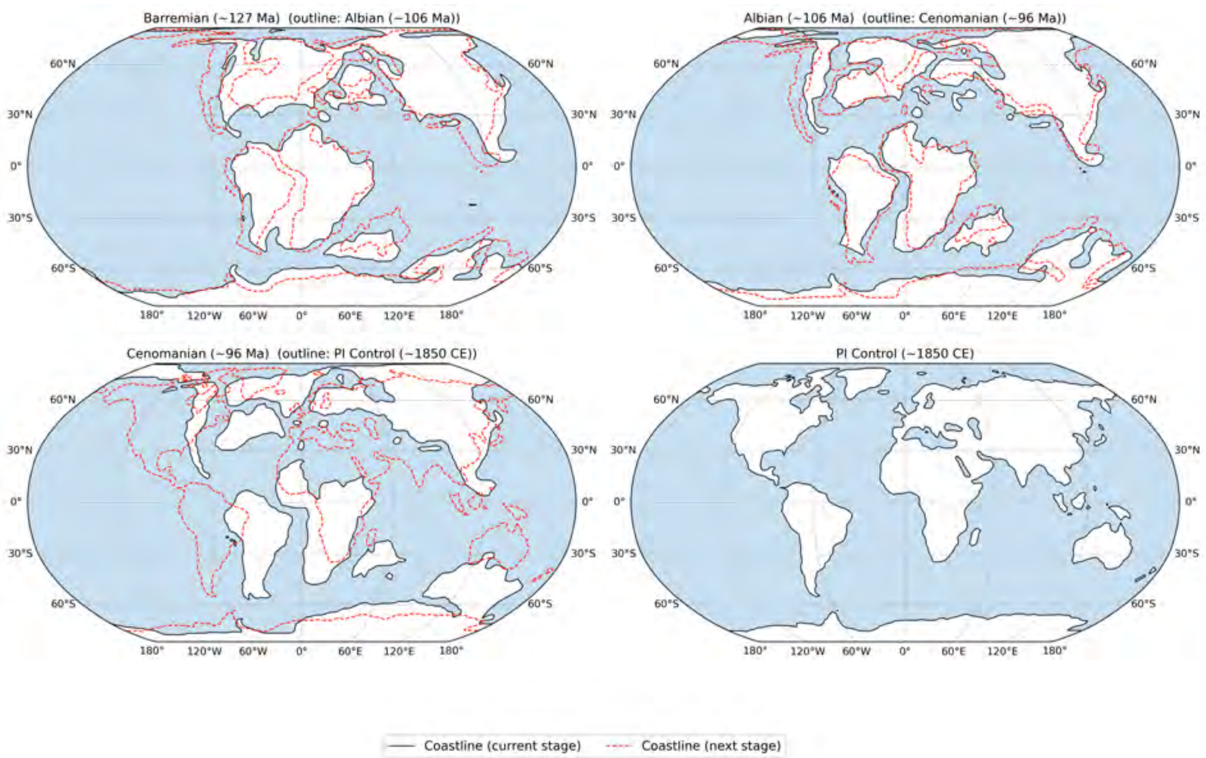

Figure 1: Simulated continental configuration of the Barremian (~127 Ma), Albian (~106 Ma), Cenomanian (~96 Ma) and PI control (1850 CE). The dashed red lines show the coastlines of the next period.

The Barremian, the Albian and the Cenomanian span approximately 30 million years of mid-Cretaceous history, during which continental configuration underwent significant change. All three stages occur during the later stages of Pangaea's break-up, with Gondwana, North America, Eurasia, and Antarctica representing the principal land masses of the Barremian as shown in (Figure 1). Across the studied interval, Gondwana progressively fragmented as South America and Africa separated, while North America was divided by the Western Interior Seaway (Miall & Catuneanu, 2019). Throughout all three intervals, substantial Gondwana landmasses occupied the southern mid-latitudes, preventing the formation of a continuous circumpolar seaway, one of the most significant differences in longitudinal ocean distribution compared to PI. The Tethys maintained a broad equatorial connection with the Pacific Ocean, though the geometry of this seaway changed as Laurasia continued to fragment and the proto-Atlantic widened, progressively reducing the northern latitudes land fraction from the Barremian to the Cenomanian, around 40°N (Figure 2). Proto-Australia was attached to Antarctica throughout this period, although it slowly started to migrate northward. India and Madagascar were still connected and located to the south-east of Gondwana (later Africa).

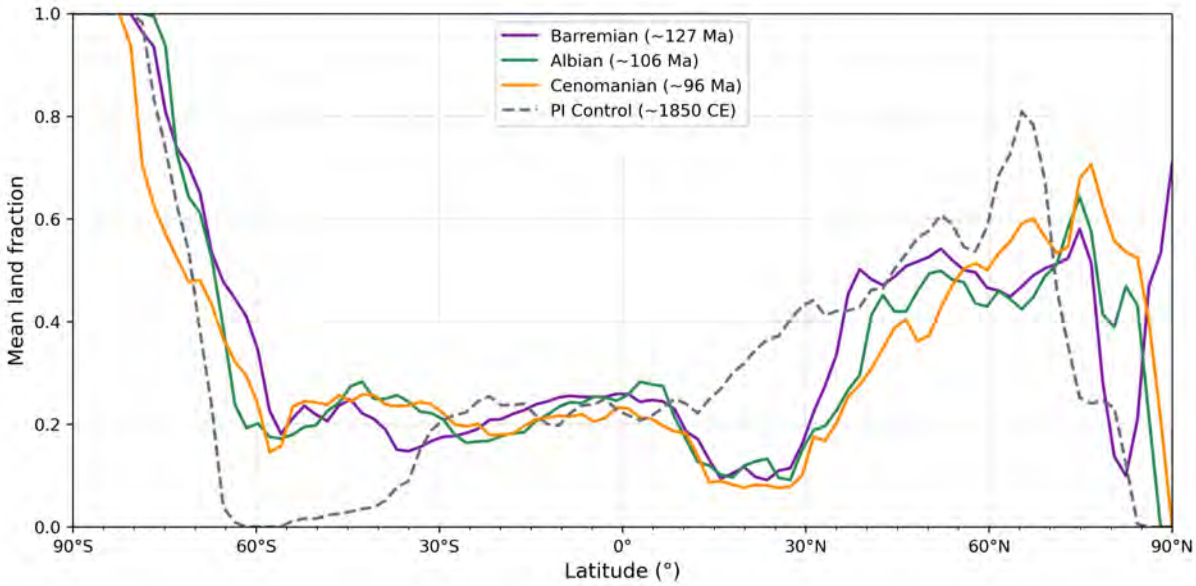

Figure 2: Simulated zonal-mean land fraction for the Barremian (∼127 Ma), Albian (∼106 Ma), Cenomanian (∼96 Ma) and PI control (1850 CE).

4 Global atmospheric and climatic state

4.1 Atmospheric temperatures

Barremian	Albian	Cenomanian	pre-industrial
16 °C	17.5 °C	17.8 °C	13.4 °C

Table 2: Simulated global mean atmospheric temperature at 992 hPa

The global mean atmospheric temperatures at 992 hPa are used here for the near surface air temperature and are shown in Table 2. The simulations show a 1.5 °C warming from the Barremian to the Albian and a 0.3 °C warming from the Albian to the Cenomanian, reflecting the general warming trend of the mid-Cretaceous greenhouse state.

Atmospheric CO_2 concentrations differ between the pre-industrial and mid-Cretaceous runs, but there is still warming across the constant CO_2 mid-Cretaceous slices, that cannot therefore be explained by the CO_2 nor the small solar changes. The simulated atmospheric temperatures at 992 hPa are shown in Figure 3. Notably, there still are differences between the mid-Cretaceous time slices, even though CO_2 is held constant across the three stages, implying that other factors, such as ocean circulation or changes in palaeogeography (Lunt et al., 2016), may drive changes in the climate that we are going to explore later. The zonal-mean per latitude shows the equator-to-pole temperature

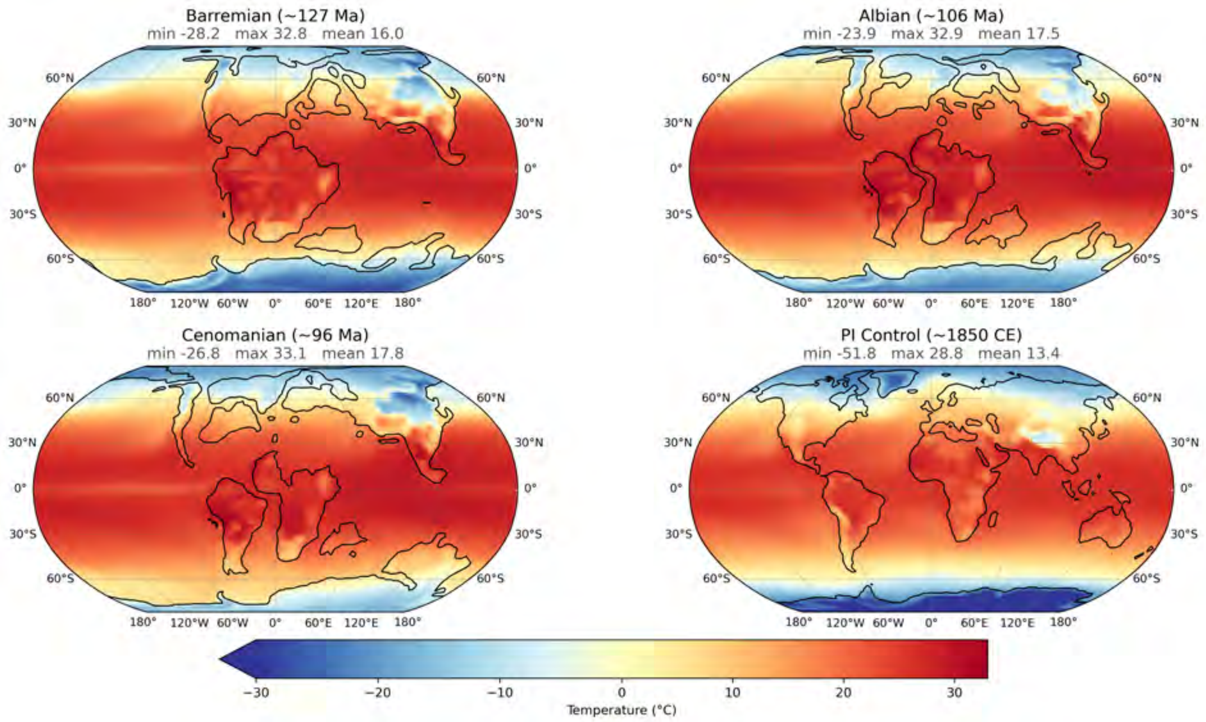

Figure 3: Simulated atmospheric temperature at 992 hPa (surface equivalent) for the Barremian (∼127 Ma), Albian (∼106 Ma), Cenomanian (∼96 Ma) and PI control (1850 CE).

profile (Figure 4), an important component of the global climate state, also allowing us to rapidly evaluate the global model's response to warming. Proxy evidence suggests the Cretaceous was characterised by a lower meridional temperature gradient compared to today, with polar latitudes being significantly warmer (Barron & Washington, 1985; Huber et al., 1995). The simulations show negative temperatures at the poles, especially the South high latitudes, for the mid-Cretaceous time slices. We still observe some warming across the stages at 90°S, with the Barremian roughly at -28 °C, the Albian about -21 °C and the Cenomanian around -15 °C. Overall, the 0 °C crossing migrates polewards in the Southern Hemisphere, consistent with the global warming trend of the mid-Cretaceous. The higher temperatures can be found in the tropics for the three simulated periods. The zonal-mean maxima are located around 15°S and 15°N for the mid-Cretaceous stages. The Barremian zonal-mean maximum is approximately 26 °C, the Albian peaks near 28 °C and the Cenomanian around 27 °C. Notably, the equator-to-pole gradient temperature

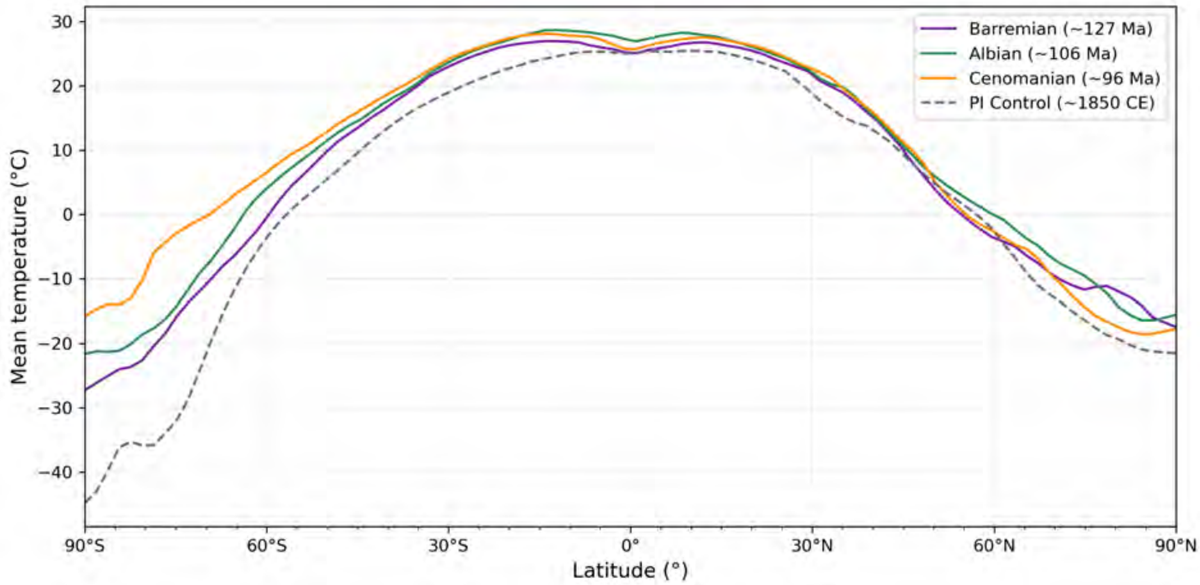

Figure 4: Simulated zonal-mean atmospheric temperature at 992 hPa for the Barremian (∼127 Ma), Albian (∼106 Ma), Cenomanian (∼96 Ma) and PI control (1850 CE).

profile has a "moustache-like" shape, maxing at the tropics and dipping at the equator, where the Cenomanian and the Barremian drop close to the PI level. The higher northern latitudes show less change between the stages than the southern ones, with PI still being the coldest at around -22 °C. However, high latitude warming during the mid-Cretaceous stages is limited, with the Barremian and the Albian being very similar at around -18 °C, and the Cenomanian being the coldest of the mid-Cretaceous periods in the northern high latitudes. Overall, the simulated stages show warmer global temperatures and rising from the Barremian to the Cenomanian, but the simulated polar temperatures are still strongly negative and show a stronger pole-to-equator temperature gradient response than what the proxy suggest (O'Brien et al., 2017; Scotese et al., 2021)

Temperature extremes are situated over land (Figure 5) and differences in temperature at high latitudes between the simulations are tightly coupled to land fraction, specifically, the air is much colder over land than over ocean. This continentality is pronounced at high latitudes with the coldest temperatures, and at the tropics, with high-temperature peaks. The simulations show warm extremes over Africa, South America and South Asia, and extreme colds mainly over Antarctica. There is a high positive signal for the mid-Cretaceous and the pre-industrial periods only for the high southern latitudes, which can be explained by the presence of Antarctica covering the whole South Pole, while the other latitudes show a weaker, less significant signal. The PI shows much colder mid southern latitudes to the South Pole.

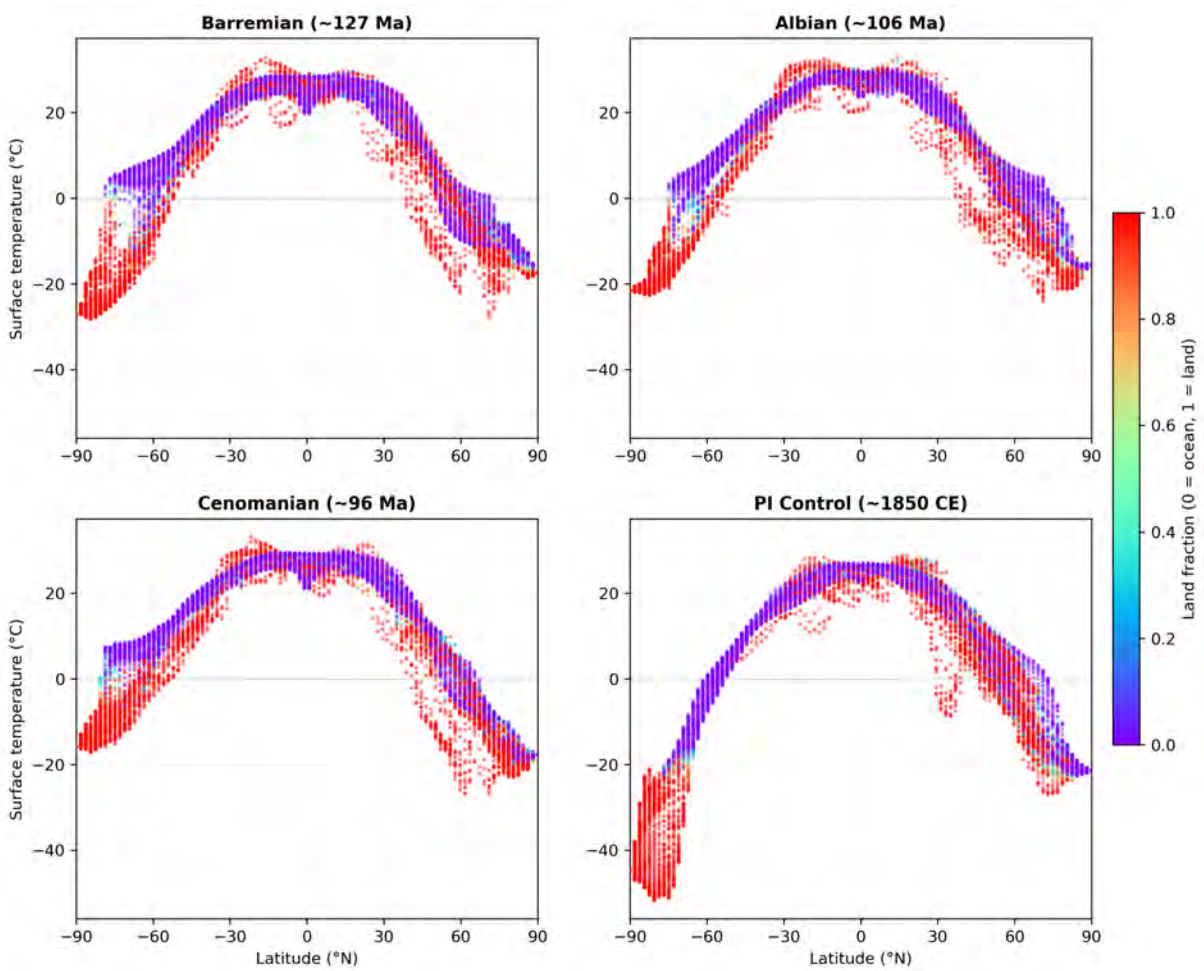

Figure 5: Atmospheric surface temperature for latitudes, categorized by land fraction (0 = ocean, 1 = land) for the Barremian (∼127 Ma), Albian (∼106 Ma), Cenomanian (∼96 Ma) and PI control (1850 CE). Each point represents a single grid cell.

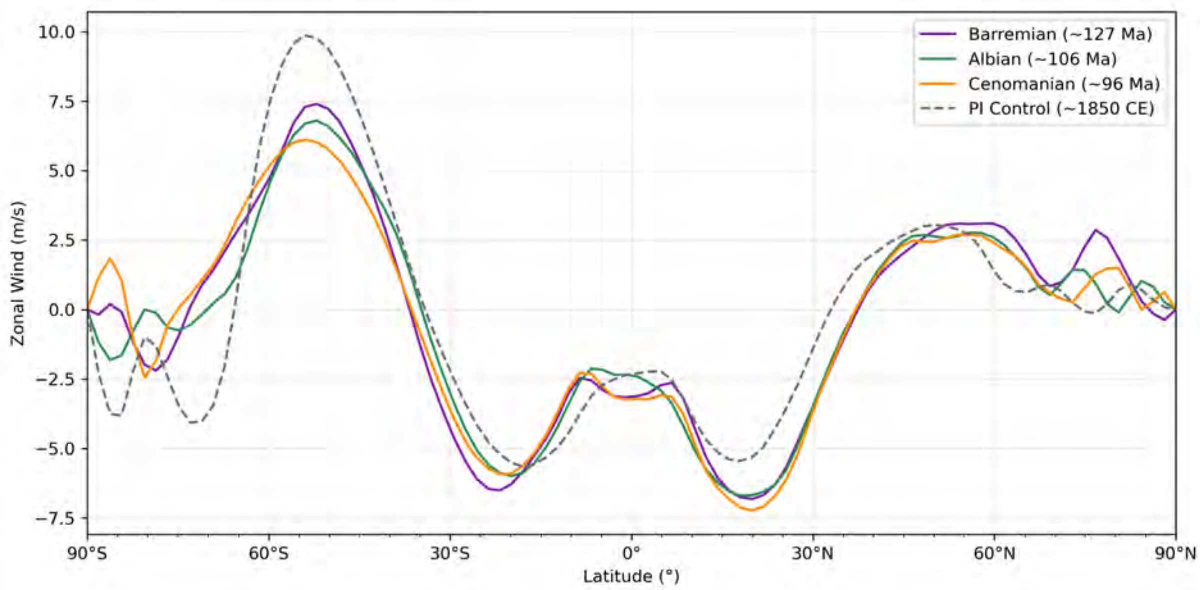

Figure 6: Simulated atmospheric zonal wind averaged by latitude for the Barremian (∼127 Ma), Albian (∼106 Ma), Cenomanian (∼96 Ma) and PI control (1850 CE).

4.2 Atmospheric circulation

Simulated zonal winds (Figure 6) are generally stronger than meridional winds (Figure 9) because of strong meridional temperature gradients (Figure 4). The equatorial easterlies and mid-latitudes westerlies are reproduced in the Cretaceous runs. The most distinctive inter-stage signal in the surface zonal wind is found in the Southern Hemisphere mid-latitude westerly belt (Figure 6), where the PI shows a strong asymmetry between the Northern Hemisphere, with weaker westerlies (∼3 m/s), and the Southern Hemisphere, with much stronger westerlies (∼10 m/s). The Cretaceous time slices have a weaker gradient. The PI control reaches a strong westerly peak at near 10 m/s, at around -50°S, whereas the Barremian peaks at ∼7.5 m/s, the Albian at ∼6.5 m/s and the Cenomanian at ∼6m/s.

At the southern high latitudes, the Barremian and Cenomanian both show predominantly westerlies, though the Cenomanian westerlies extend to higher latitudes, while the Albian and PI follow a similar curve shape to each other. Between roughly 35°S and 35°N, all four runs share a broad band of easterly dominated zonal winds. Within this band, the Cretaceous maps (Figure 7) show two weak equatorial westerly patches, one to the west of Gondwana and one to the east over the ocean between Gondwana and Southern Asia. The PI has similar weak westerlies, west of South America, Africa, and India. Winds are

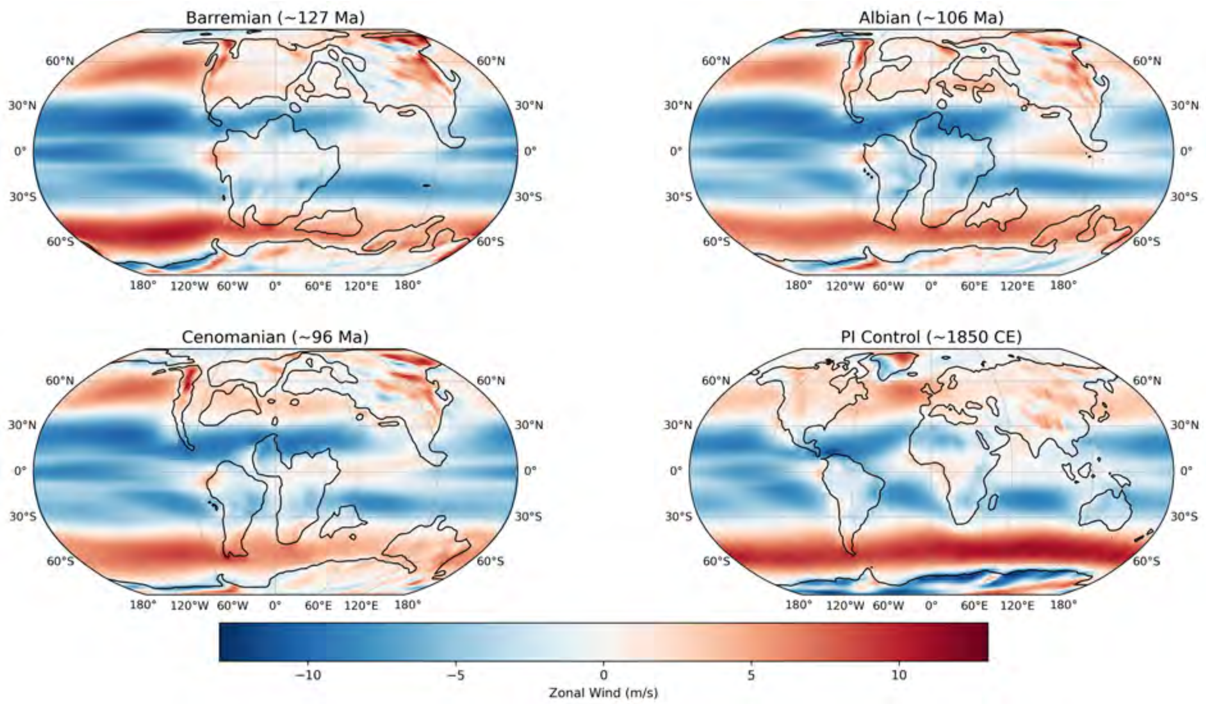

Figure 7: Simulated atmospheric zonal wind at 992 hPa for the Barremian (∼127 Ma), Albian (∼106 Ma), Cenomanian (∼96 Ma) and PI control (1850 CE).

strongly influenced by temperature and land–sea distribution. By comparing the wind distribution with the continental configuration (Figure 7), the less uniform distribution of westerlies and easterlies is observed over continents, as illustrated with the proto-Rocky Mountains formation and the north China orogenic belt that, which, during the Cretaceous periods, were greatly dominated by strong westerlies. Continental drift also changes wind distribution as a main driver for climate change (Lunt et al., 2016; Ruddiman, 2014). The wide Pacific of the mid-Cretaceous show a stronger and wider easterly pattern (Fig-

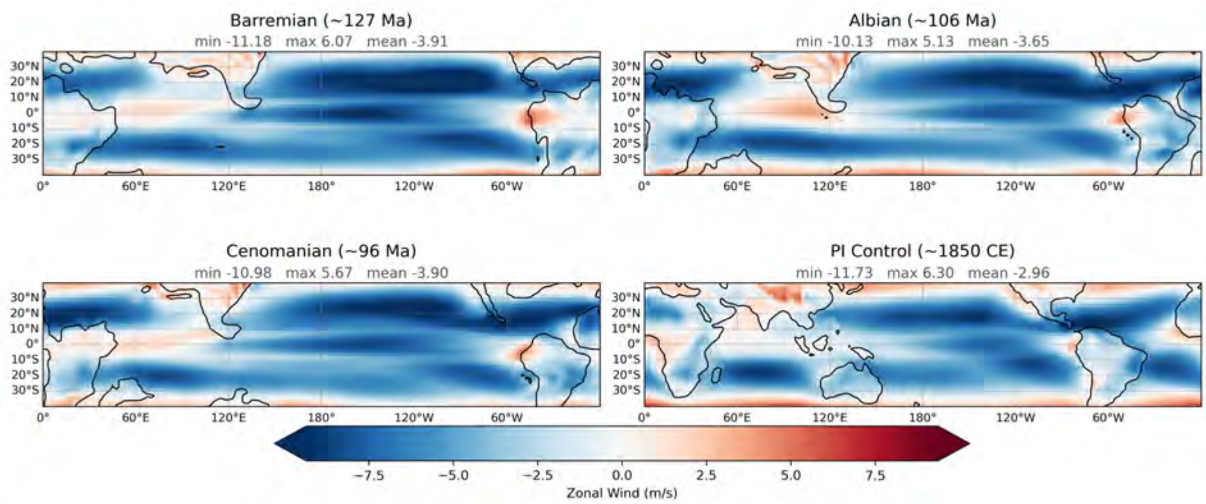

Figure 8: Simulated atmospheric zonal wind at 992 hPa between 40°S and 40°N for the Barremian (∼127 Ma), Albian (∼106 Ma), Cenomanian (∼96 Ma) and PI control (1850 CE).

ure 8), that is particularly wide in the Barremian and in the Cenomanian (ranging from 120°E eastward across the dateline to 60°W). This equatorial strong zonal wind implications are addressed in Section 5.4. A counter-cell at the equator (Figure 9), between the Southern and Northern Hemisphere Hadley cells, running opposite to the Hadley cell is observed in the mid-Cretaceous and not present in the pre-industrial. Meridional winds also differ between the mid-Cretaceous and the pre-industrial, with weaker South Polar cells in the Barremian, Albian and Cenomanian.

4.3 Land snow cover and sea ice distribution

The snow cover (Figure 10) is a major component of the surface albedo and has strong effect on temperatures (Ruddiman, 2014). In the Southern high latitudes, the Antarctic continent was largely covered in snow in our simulations, until ∼70°S, during the Barremian. The Albian shows less snow coverage than the Barremian, although it is still notably present. The Cenomanian is the Cretaceous stage that stands out, with considerably less snow coverage on Antarctica. The general pattern is a Southern snow decrease across the Cretaceous runs. In the Northern high latitudes, the Barremian shows snow coverage on the West coast of North America, on the proto-Rocky Mountains range, north of Eurasia and at the pole. The Albian simulation has similar snow coverage, and the Cenomanian, although being the warmest period of the three, has the most snow coverage at high latitudes. This, however, is due to the southward shifting of the Northern

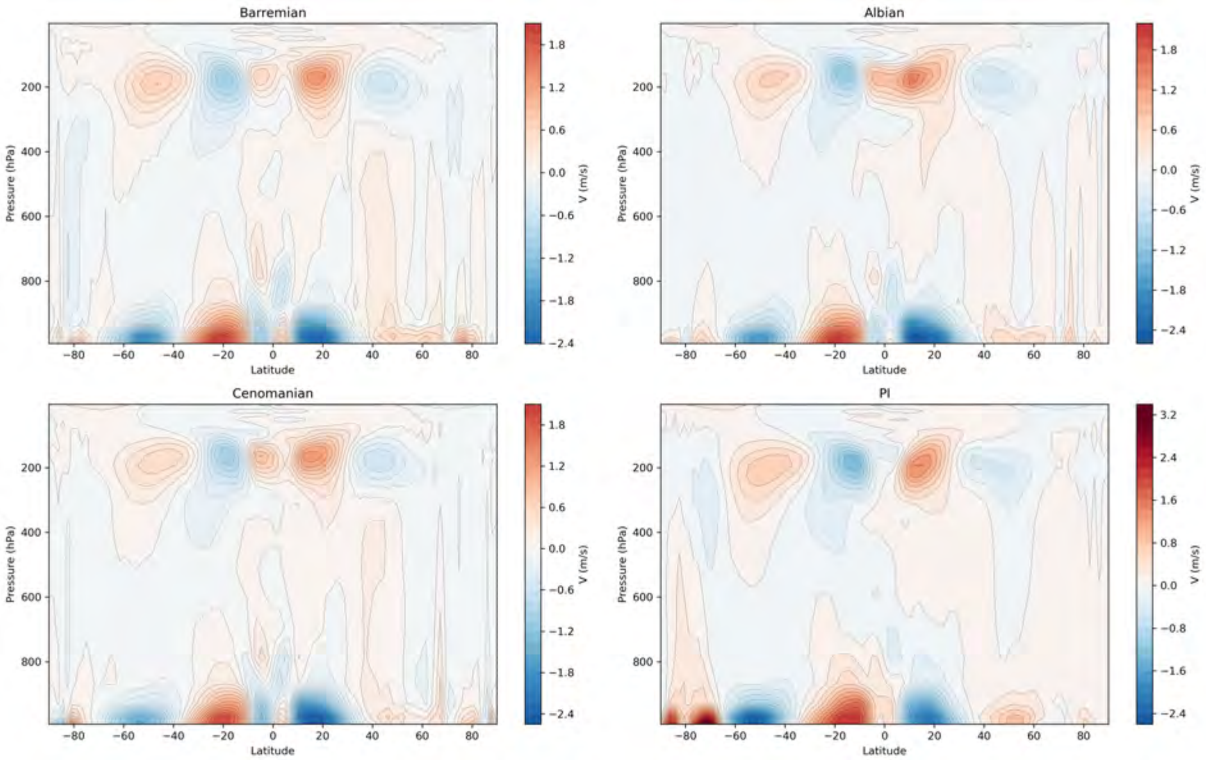

Figure 9: Meridional wind cells derived from simulated atmospheric meridional wind averaged per latitude, for the Barremian (~127 Ma), Albian (~106 Ma), Cenomanian (~96 Ma) and PI control (1850 CE).

Hemisphere landmasses observed on the continental layout. Across all three Cretaceous runs, northern snow persists on the northern most land. In the PI, however, the main snow cover is on Greenland and northern Canada. The Cretaceous snow-covered land has shifted southward. The sea ice field (Figure 11) shows a comparable hemispheric pattern to the land snow cover, although it is less extensive. In the Southern high latitudes, sea ice also decreases across the Cretaceous runs. In the Barremian, we find notable discontinuous sea ice fraction around the coast of Antarctica, more precisely near proto-Australia and at the 60°W longitude. The Albian shows less ice than the Barremian, though some patches are observable around proto-Australia and 60°W, and the Cenomanian shows close to no Southern sea ice, with only a small amount remaining near the same landmass. The PI control shows a strong band of Southern sea ice from 60°S and southward. Below 80°S the surface is the Antarctic continent and therefore carries no sea ice but has a high snow depth as shown earlier. In the Northern high latitudes, the Cretaceous stages show significant amount of sea ice fraction, with the Barremian having a lower peak than the other, due to the presence of more land in the pole (See appendix, Figure A.2).

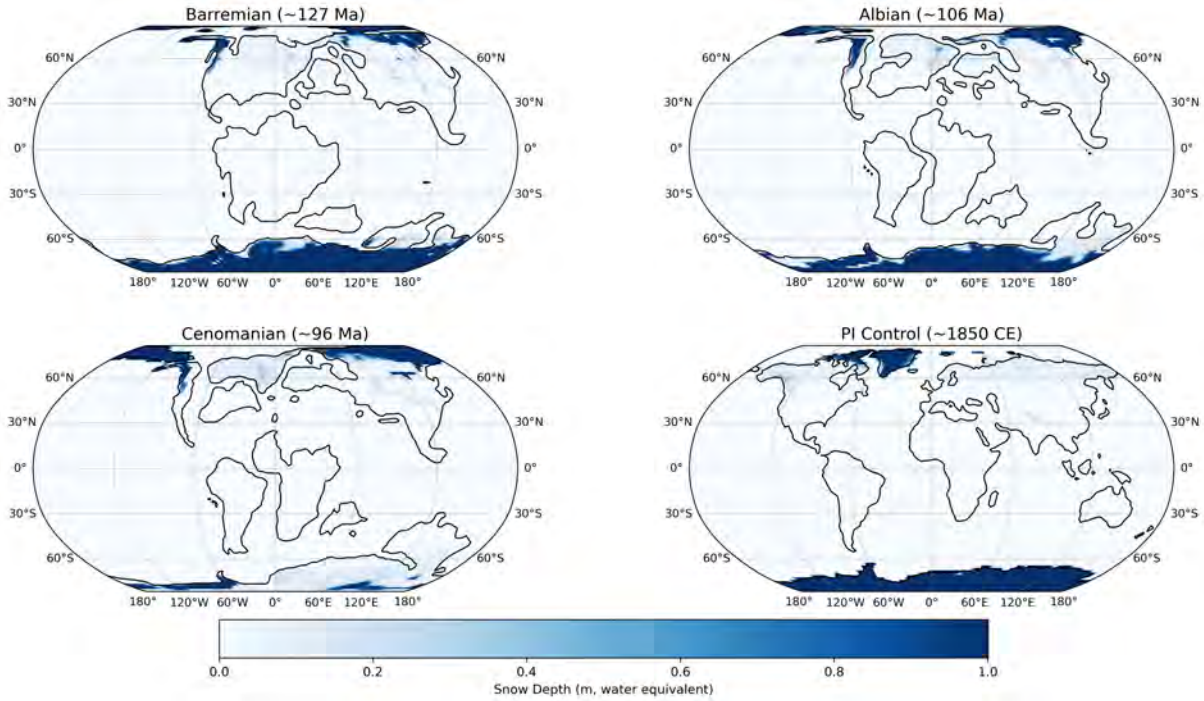

Figure 10: Simulated land snow coverage as water equivalent depth for the Barremian (~127 Ma), Albian (~106 Ma), Cenomanian (~96 Ma) and PI control (1850 CE).

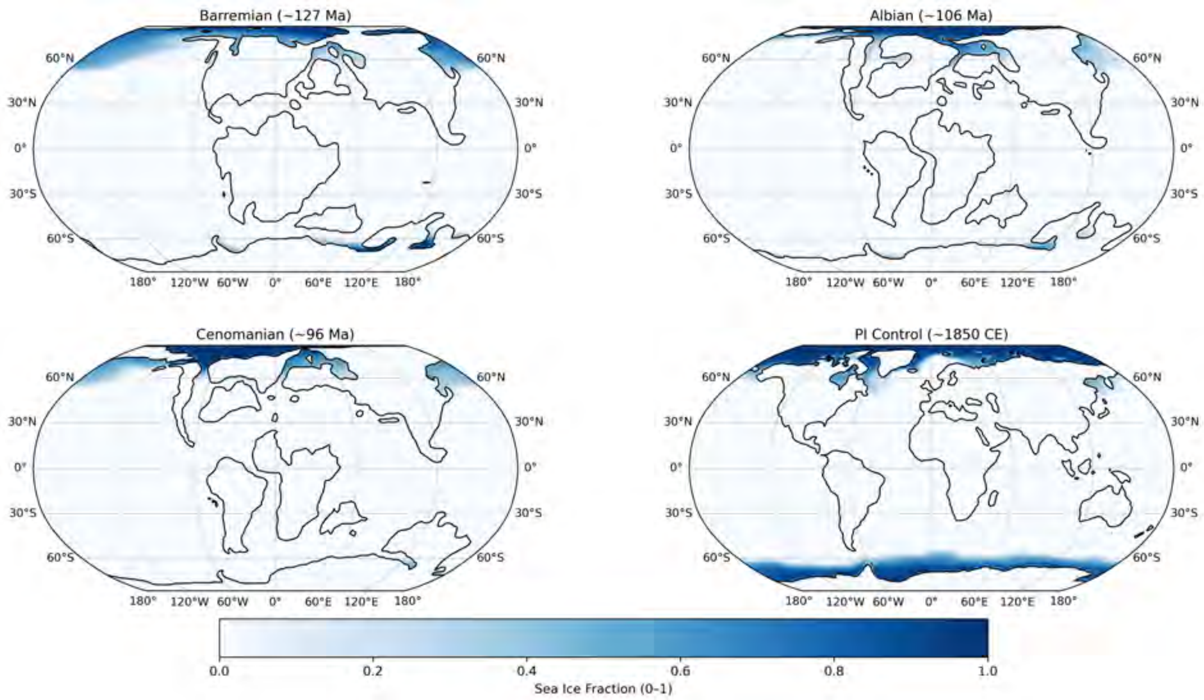

Figure 11: Simulated sea ice coverage for the Barremian (~127 Ma), Albian (~106 Ma), Cenomanian (~96 Ma) and PI control (1850 CE).

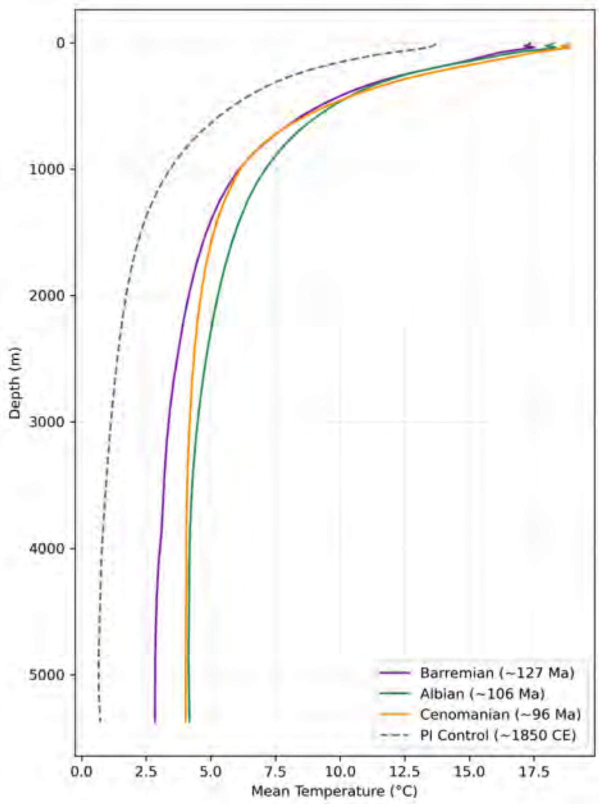

Figure 12: Simulated global mean oceanic temperature profile for the Barremian (∼127 Ma), Albian (∼106 Ma), Cenomanian (∼96 Ma) and PI control (1850 CE).

5 Ocean circulation

5.1 Oceanic temperatures

The global mean oceanic temperature profile (Figure 12) shows similar curves for the Barremian, the Albian and the pre-industrial simulations, whereas the Cenomanian curve shows a rapid decrease in temperature until 1000 metres deep at 6.2 °C, and temperatures decreasing only to 4.2 °C at the bottom. At the surface, the four runs share similar global distribution (Figure 13), with the Cretaceous stages showing higher mean oceanic temperature: 17.3 °C for the Barremian, 18.2 °C for the Albian and 18.8 °C for the Cenomanian, contrasting with the 13.7 °C of the pre-industrial (Table 3a).

Here we focus on the temperature of the surface ocean, the intermediate depth ocean (1000 metres) and the deeper ocean (3000 metres). In the Southern high latitudes, the Barremian shows cold oceanic surface temperatures around the coast of Antarctica, with the coldest patches around proto-Australia and at the 60°S latitude, where landmasses seem to have a high impact on the oceanic temperature. A gradual warming up toward the tropics is observed, and follows a similar “moustache-like” curve as the Atmospheric temperature, with a dip of ∼6 °C for the Barremian at the equator, going under the pre-industrial curve (Figure 14). The Albian shows a similar pattern overall, but has the

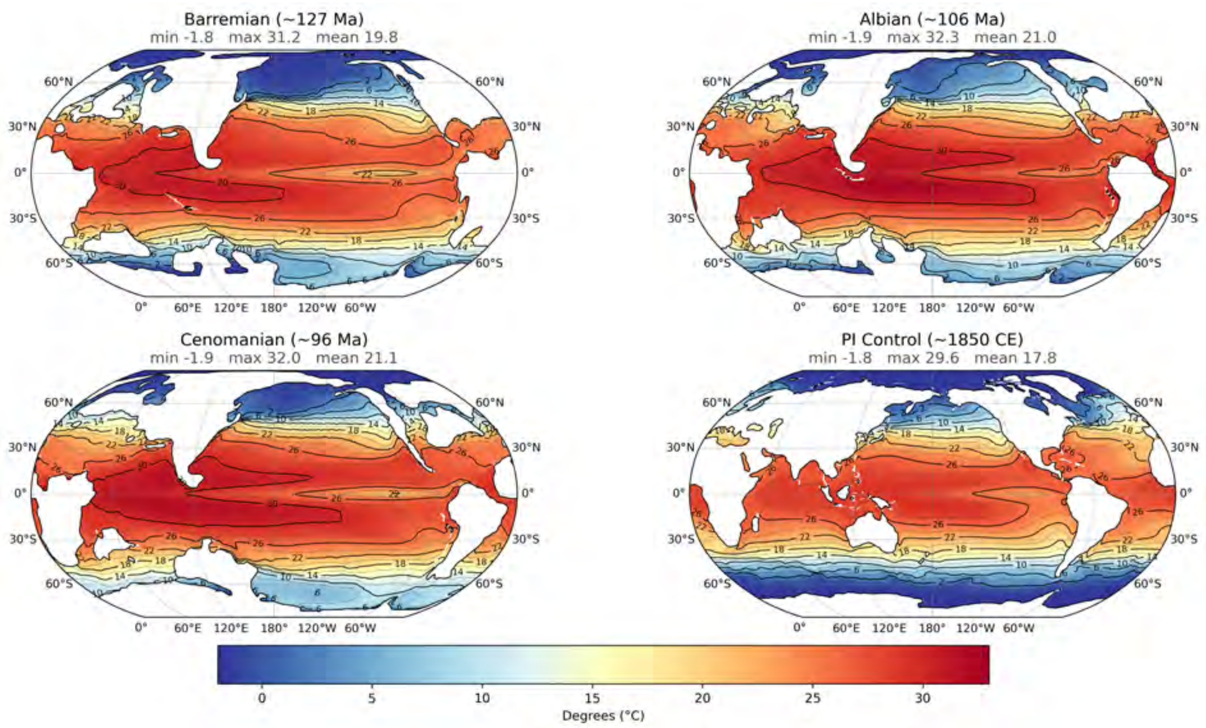

Figure 13: Simulated oceanic surface temperature for the Barremian (∼127 Ma), Albian (∼106 Ma), Cenomanian (∼96 Ma) and PI control (1850 CE).

(a) Global mean oceanic temperature (°C) by depth.

	Surface	1000 m	3000 m
Barremian	17.3	6.2	3.4
Albian	18.2	7.2	4.6
Cenomanian	18.8	6.2	4.2
pre-industrial	13.7	3.5	1.2

(b) Global oceanic temperature minimum and maximum (°C) by depth.

	Surface		1000 m		3000 m	
	Min	Max	Min	Max	Min	Max
Barremian	-1.8	31.2	-1.2	19.3	2.0	19.0
Albian	-1.9	32.3	3.3	27.6	3.4	21.7
Cenomanian	-1.9	32.0	-1.6	20.0	3.4	18.9
pre-industrial	-1.8	29.6	-1.2	16.0	-0.4	13.5

Table 3: Simulated global oceanic temperatures (°C) at surface, 1000 metres and 3000 metres depth levels. (a) Global mean values. (b) Global minimum and maximum values.

warmest peak at the equator, whereas the Cenomanian exhibits warmer Southern high latitudes oceanic temperatures. The PI, in contrast, has a much colder south circumpolar ocean. The Northern Hemisphere higher latitudes show similar characteristics for the four time slices. At 1000 metres deep, the temperature distribution is more uniform than at

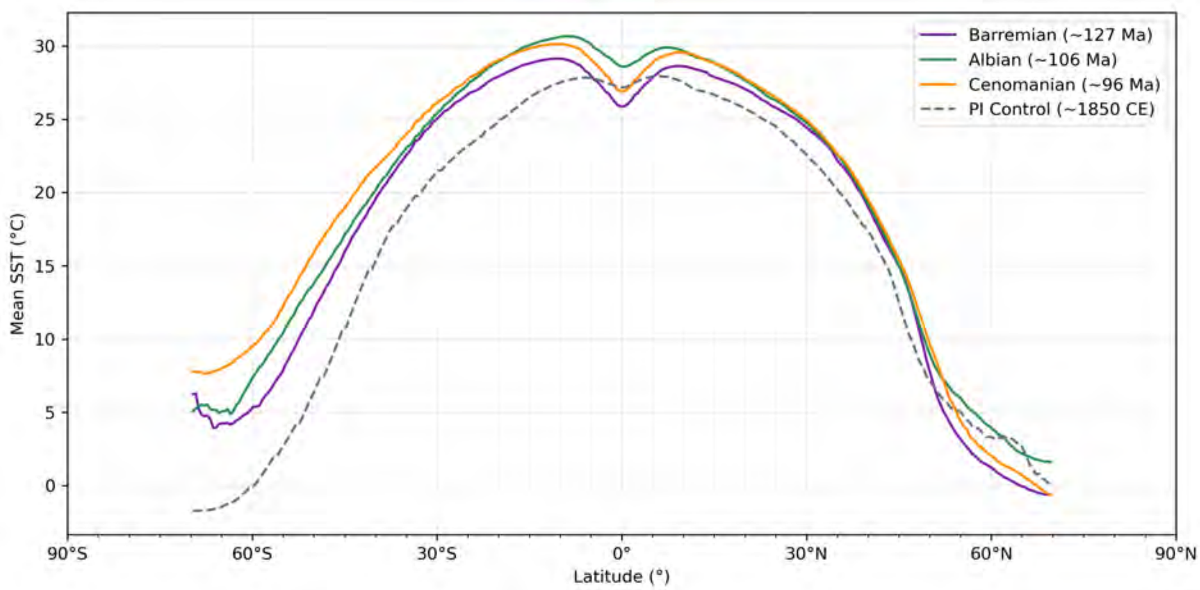

Figure 14: Simulated zonal-mean oceanic surface temperature for the Barremian (∼127 Ma), Albian (∼106 Ma), Cenomanian (∼96 Ma) and PI control (1850 CE).

the surface (Figure 15) with the highest global mean at the Albian (7.3 °C), the lowest for the PI (4.1 °C) and the Barremian and Cenomanian close to each other (around 6.3 °C). The Albian minimum is 3.3 °C, while the Barremian, Cenomanian and PI have sub-zero minima. The high latitudes for the Cretaceous stages show fairly similar temperature levels. The Barremian has a warmer band between Gondwana and Antarctica at 60°S that disappears with the continent's break-up in the Albian and Cenomanian. There is a patch of distinctively high-temperature water between Laurasia and Gondwana in the Barremian, that reaches temperatures of 20 °C and higher. The Albian has the warmest intermediate ocean between 45°S and 45°N, with what seems to be a "leak" of the warm proto-North Atlantic waters into the Pacific and the Tethys. The Cenomanian shows a more equilibrated temperature distribution, but still has a patch of warm water at the south of the Western Interior Seaway splitting North America. The PI has a much colder ocean overall, apart from the North Atlantic warm waters caused by the North Atlantic Current (Ruddiman, 2014) and the Mediterranean Sea. At 3000 metres deep, the Cretaceous time slices are far more equilibrated with a mean of 3.4 °C for the Barremian, 4.6 °C for the Albian, 4.2 °C for the Cenomanian, and 1.3 °C for the pre-industrial. The Barremian Pacific and Tethys show uniform temperatures between 3-4 °C, with warmer waters found between Gondwana and Antarctica, and between Gondwana and Laurasia, similar to temperatures at 1000 metres depth (Figure 16). The Albian, with its warmer mean temperature, shows colder warm waters in the proto-North Atlantic than

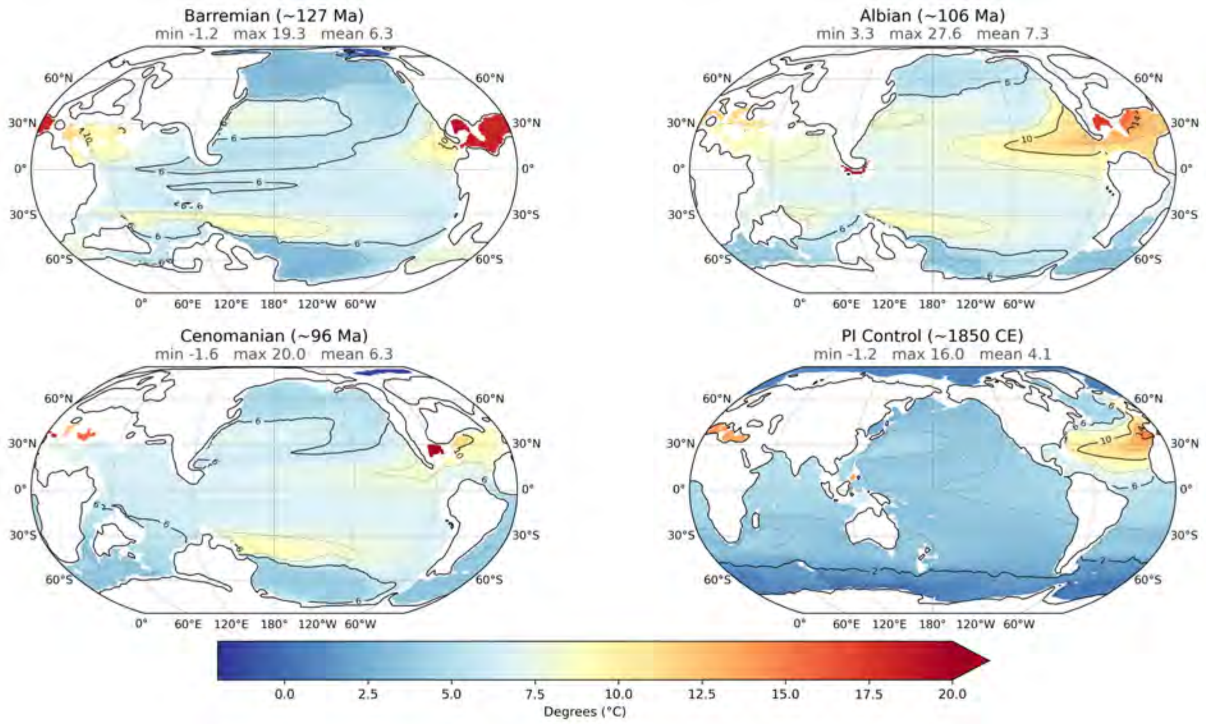

Figure 15: Simulated oceanic temperature at 1000 metres depth for the Barremian (~127 Ma), Albian (~106 Ma), Cenomanian (~96 Ma) and PI control (1850 CE).

the Barremian, apart from the patch in the Southern Western Interior Seaway, but shows warmer temperatures in the eastern Pacific Ocean in the Northern Hemisphere. Just south of the southern Asia tip, there is a warm-water patch at both 1000 metres and 3000 metres depth as well. The Cenomanian has equilibrated globally, apart from the same patch in the Southern Western Interior Seaway. The pre-industrial is colder globally, with a cold Antarctic circumpolar band, a cold Pacific, and a warmer Atlantic.

5.2 Precipitation, evaporation, and salinity of the oceans

At the equator, there is a wide precipitation band at the intertropical convergence zone, due to the convergence of the Northern and Southern trade winds, causing the air to rise and high precipitations (Fallot, 2021). The Cretaceous stages show a much stronger ITCZ precipitation area than the pre-industrial does (Figure 17). The Barremian shows strong evaporation in the subtropics (around 30°S and 30°N) with an asymmetry in favour of the Northern subtropic, present in the Cenomanian as well (Figure 18). A notable difference between the mid-Cretaceous and the pre-industrial is the presence of a large evaporation patch over the Tethys, that seems to be equilibrated in the zonal average of the PI. Moreover, the Cretaceous time slices have a precipitation-dominated band traversing the Pacific from eastern Asia at 30°N to North America at 60°N. This North Pacific precipitation band is smaller during the PI, where instead we have the subtropic evaporation band ranging from Western America to China.

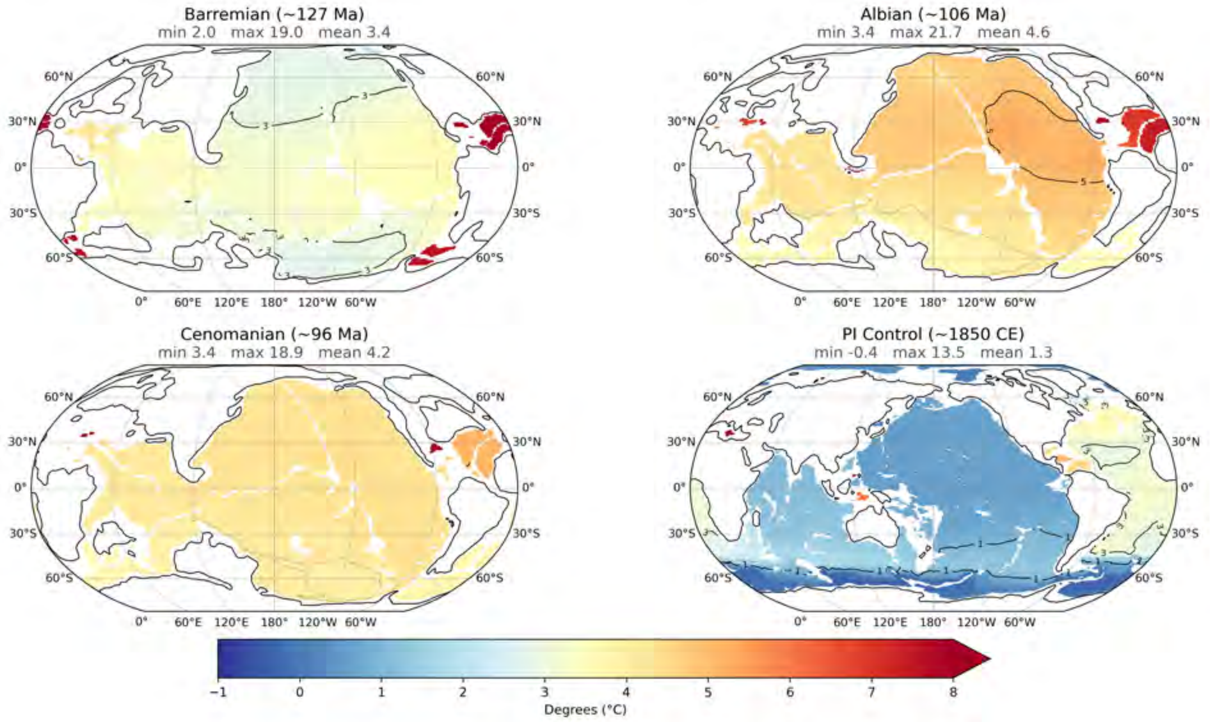

Figure 16: Simulated oceanic temperature at 3000 metres depth for the Barremian (∼127 Ma), Albian (∼106 Ma), Cenomanian (∼96 Ma) and PI control (1850 CE).

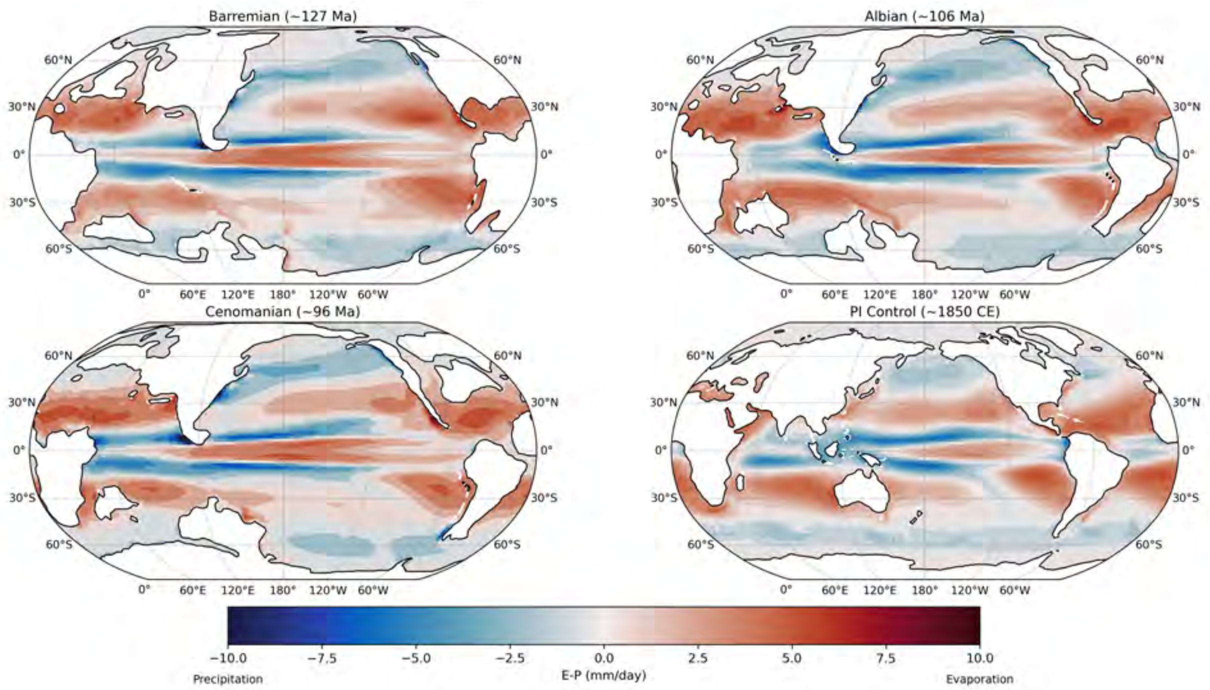

Figure 17: Simulated evaporation-minus-precipitation flux for the Barremian (∼127 Ma), Albian (∼106 Ma), Cenomanian (∼96 Ma) and PI control (1850 CE). Red is net evaporation (E > P) and blue is net precipitation (E < P).

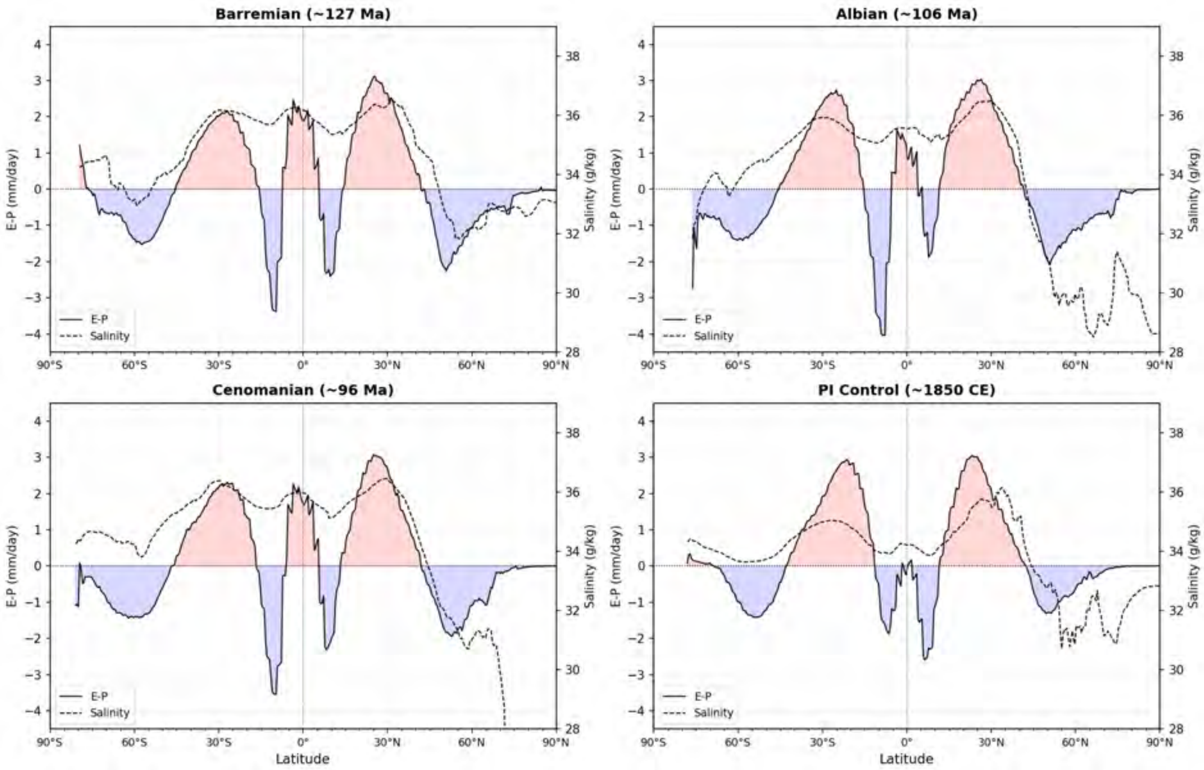

Figure 18: Simulated oceanic zonal average evaporation minus precipitation and oceanic surface salinity for the Barremian (∼127 Ma), Albian (∼106 Ma), Cenomanian (∼96 Ma) and PI control (1850 CE). Salinity clipped at 28 g/kg.

Evaporation and Precipitation have a high impact on ocean salinity, with net evaporation accompanied by a rise in salinity and precipitation accompanied by a decrease in salinity (Figure 18). However, the Albian and the Cenomanian Northern high latitudes do not follow this pattern, with the Albian dropping at around 50°N and the Cenomanian with a small zonal average dropping to a low 5 g/kg at the pole (Figure 19). These low salinity values are in enclosed areas of the ocean, such as the enclosed Arctic Ocean and the Western Interior Seaway (Figure 20). These extreme values show little concordance with precipitation nor evaporation, however. Another strong influence on Salinity is the continental run-off freshwater delivery to coastal regions. Here we see a strong link between regions of low salinity and freshwater run-off into the ocean (Figure 21), for example at the western tip of South Asia, or along the Coast of Antarctica at 60°S 60°E, for the Albian and the Cenomanian. The Cenomanian has a much stronger run-off in the Arctic Ocean (See appendix, Figure B.8). Overall, salinity is controlled by freshwater input, such as precipitation and continental run-off, as well as by evaporation and ice cover (Fallot, 2021). As depth increases, the range of salinity decreases. At 1000 metres depth, high-salinity waters are mainly confined between Gondwana and North America (Figure 22), with some flow into the Pacific during the Barremian, Albian and Cenomanian. This "leakage" in the Pacific follows the same pattern as the temperature outflow (Figure 15). The Cretaceous stages have a higher 1000 metres salinity overall in the Pacific:

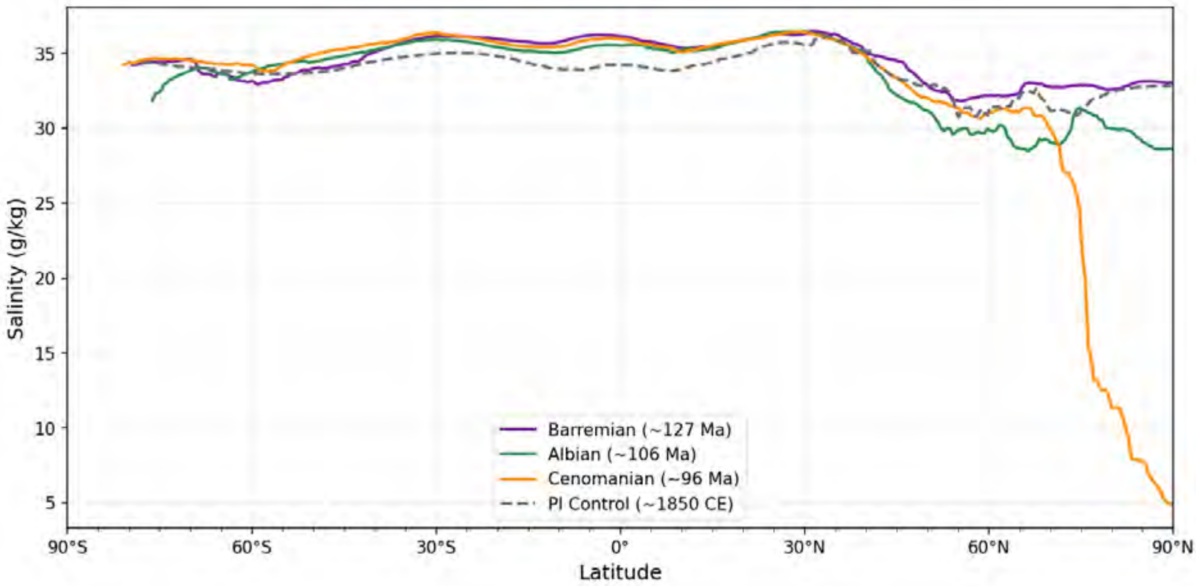

Figure 19: Simulated surface oceanic zonal-mean salinity for the Barremian (∼127 Ma), Albian (∼106 Ma), Cenomanian (∼96 Ma) and PI control (1850 CE).

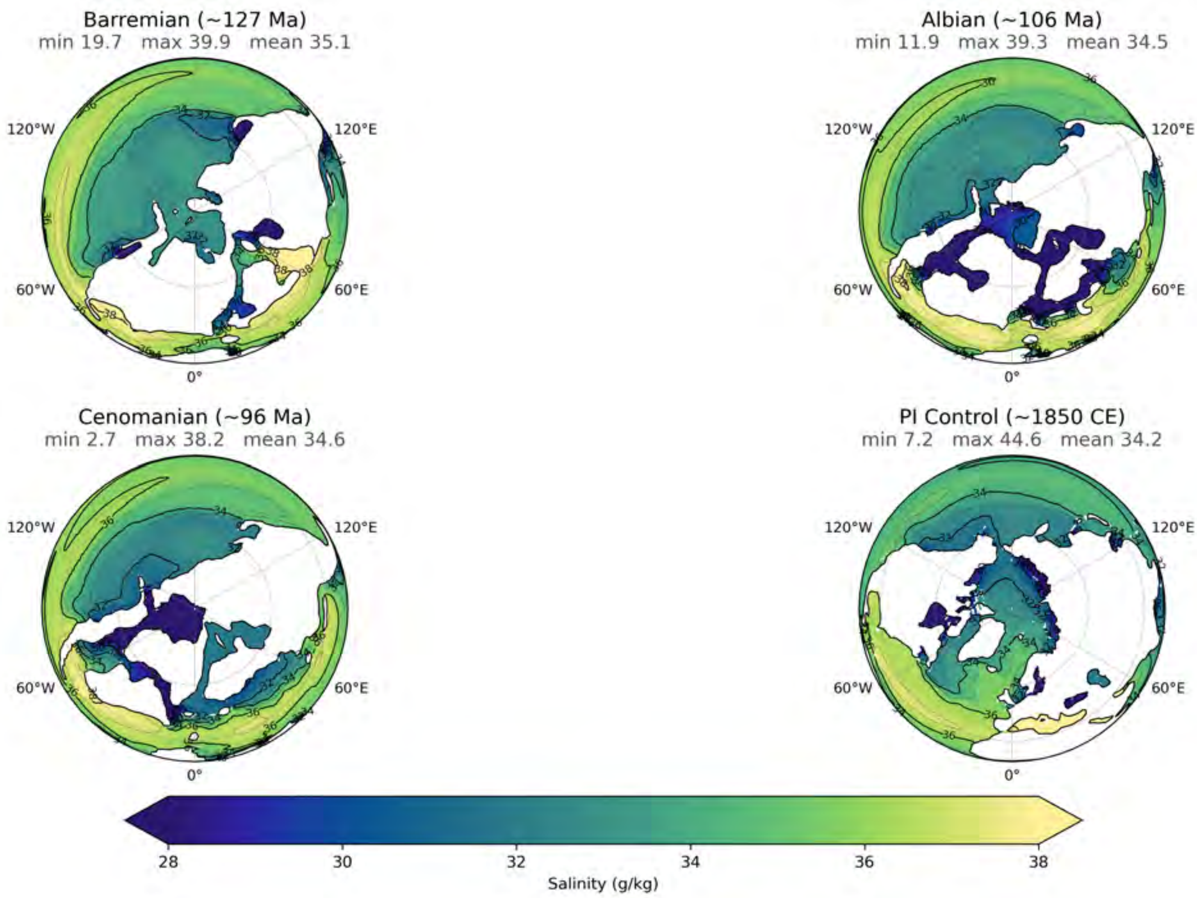

Figure 20: North Pole orthographic view of the surface salinity of the Barremian (∼127 Ma), Albian (∼106 Ma), Cenomanian (∼96 Ma) and PI control (1850 CE).

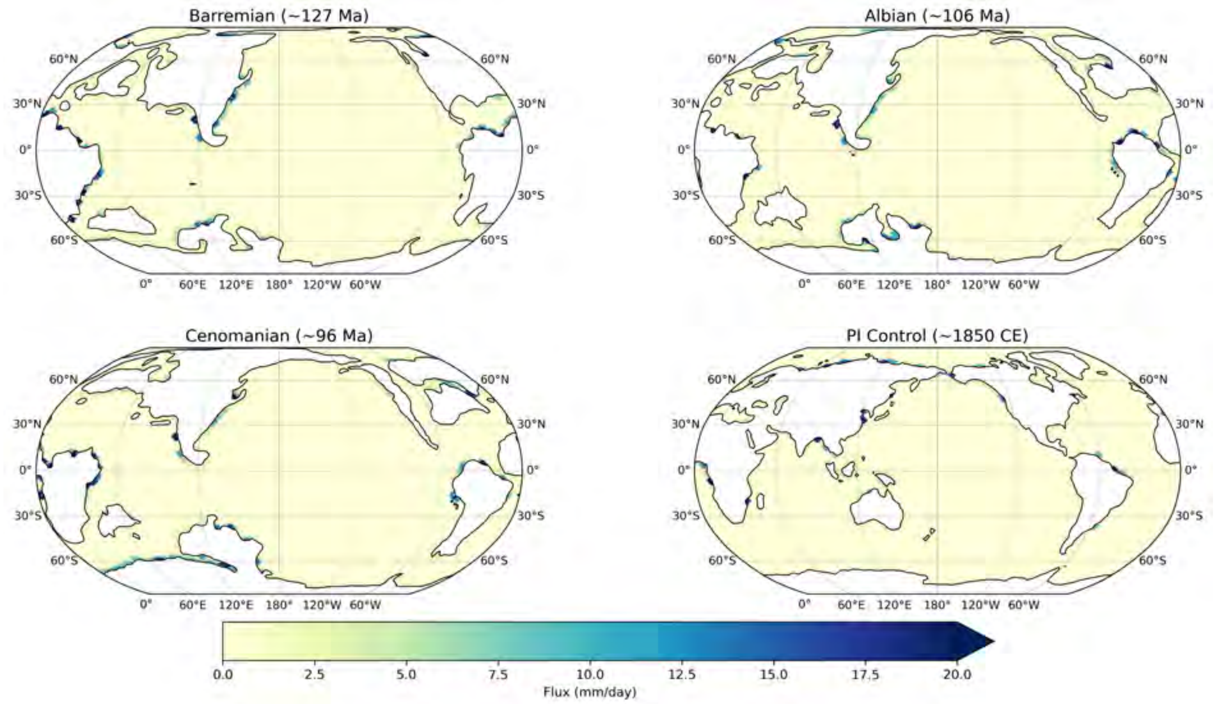

Figure 21: Simulated oceanic run-off freshwater flux for the Barremian (~127 Ma), Albian (~106 Ma), Cenomanian (~96 Ma) and PI control (1850 CE).

the Barremian have the least extensive "leakage" of salty waters from the proto-Atlantic and the Tethys, and displays a band of salty Pacific water between 30°N and 45°S. Low salinity waters are mostly located in the Northern Pacific and in the Southern Pacific, east of proto-Australia. The Albian has the strongest discharge of high salinity waters from the proto-Atlantic, with a lobe ranging nearly up to 180° longitude. The North Pacific has less salt than the Barremian, but there are more freshwater sources in the Southern Hemisphere, mainly between at 60°S, between 120°E and 60°W, between Antarctica and Gondwana. The Cenomanian has a less intensive saltwater outflow than the Albian, but displays saltier waters north-east of proto-Australia. Northern Pacific has fresher water than Albian, and the enclosed ocean between proto-Australia, Africa and South America have low salinity. The pre-industrial follows globally similar high salinity areas, where the highest salinity is in the North Atlantic and in the Mediterranean. The PI is generally less saline than the mid-Cretaceous simulated oceans at those depths, specifically in the Pacific and Indian Ocean. At a depth of 3000 metres, the distribution changes once more, showing a generally reduced salinity globally during the Cretaceous time slices and the pre-industrial period (Figure 23). There are still the high salinity patches between Gondwana and North America in the Barremian and the Albian. The Barremian shows lower salinity in southern high latitudes and northern high latitudes, with intermediate salinity from the subtropics to the equator. The Albian does not show this same distribution, but shows a stronger influence of high salinity "leakage" from the proto-Atlantic into the eastern Pacific. The Cenomanian has an overall uniform range, with a notable

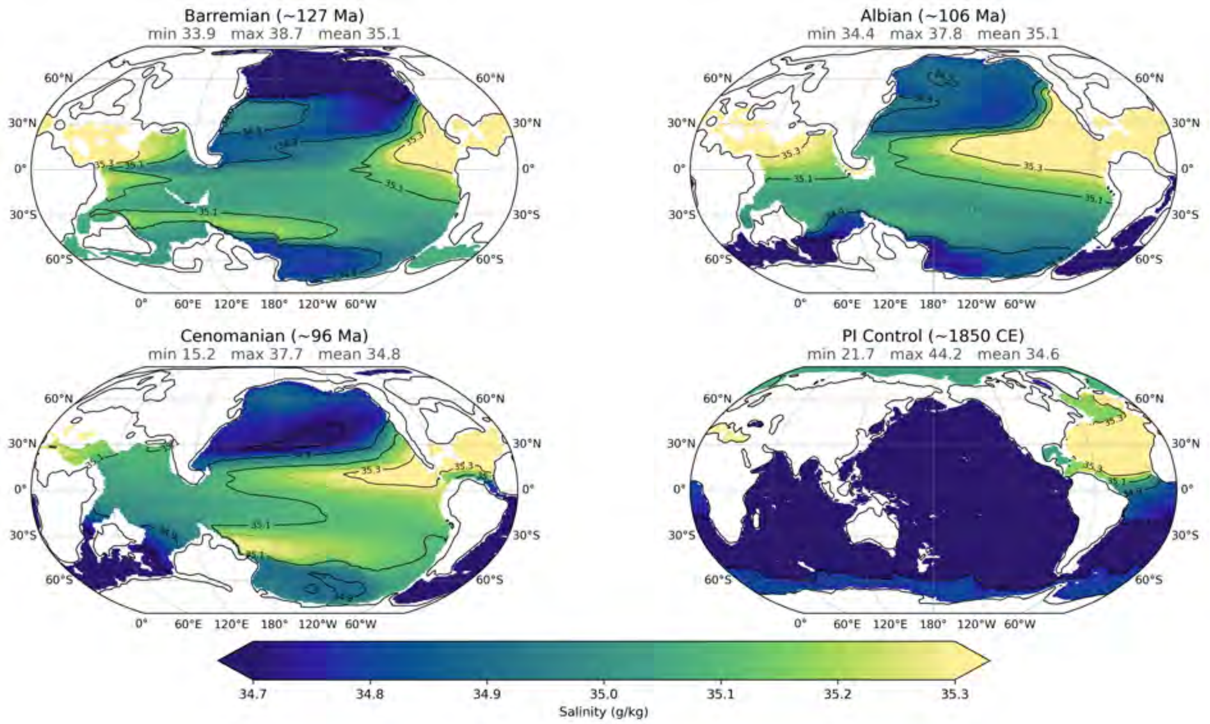

Figure 22: Simulated oceanic salinity at 1000 metres depth for the Barremian (∼127 Ma), Albian (∼106 Ma), Cenomanian (∼96 Ma) and PI control (1850 CE).

high salinity patch south of the Western Interior Seaway. The pre-industrial simulation has a much less saline Pacific Ocean, and intermediate salinity in the Atlantic and the Arctic Ocean.

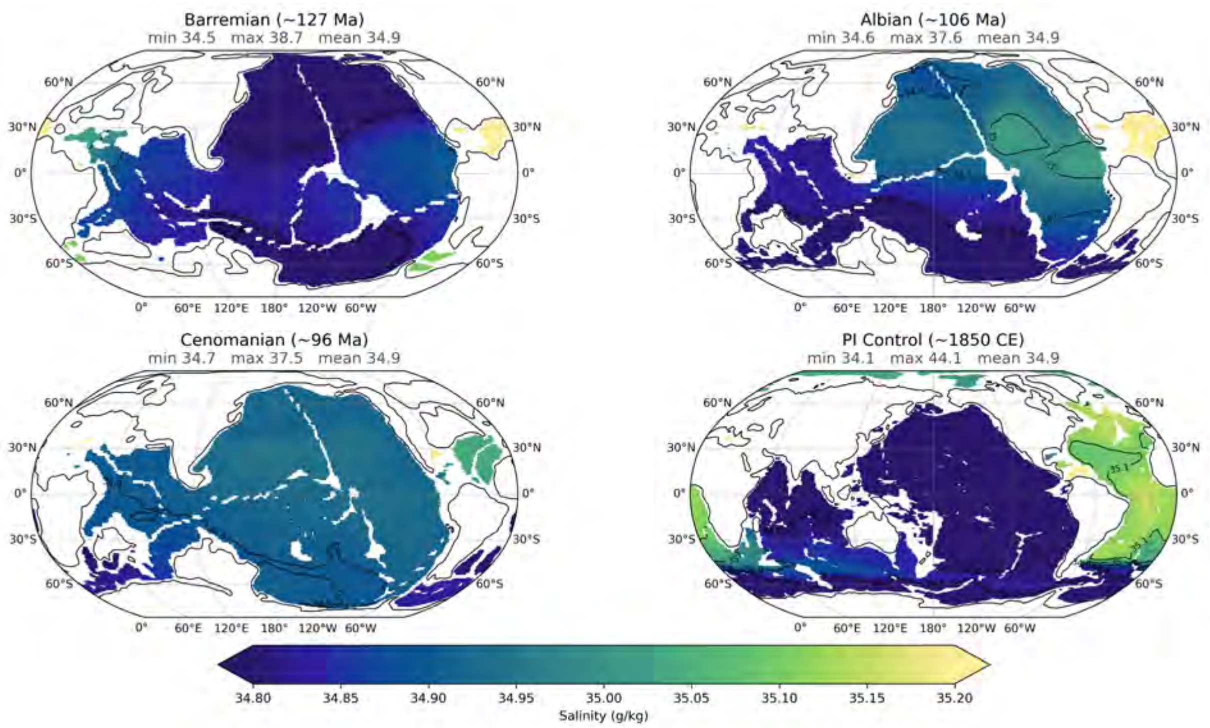

Figure 23: Simulated oceanic salinity at 3000 metres depth for the Barremian (∼127 Ma), Albian (∼106 Ma), Cenomanian (∼96 Ma) and PI control (1850 CE).

5.3 The Mixed layer depth of the oceans

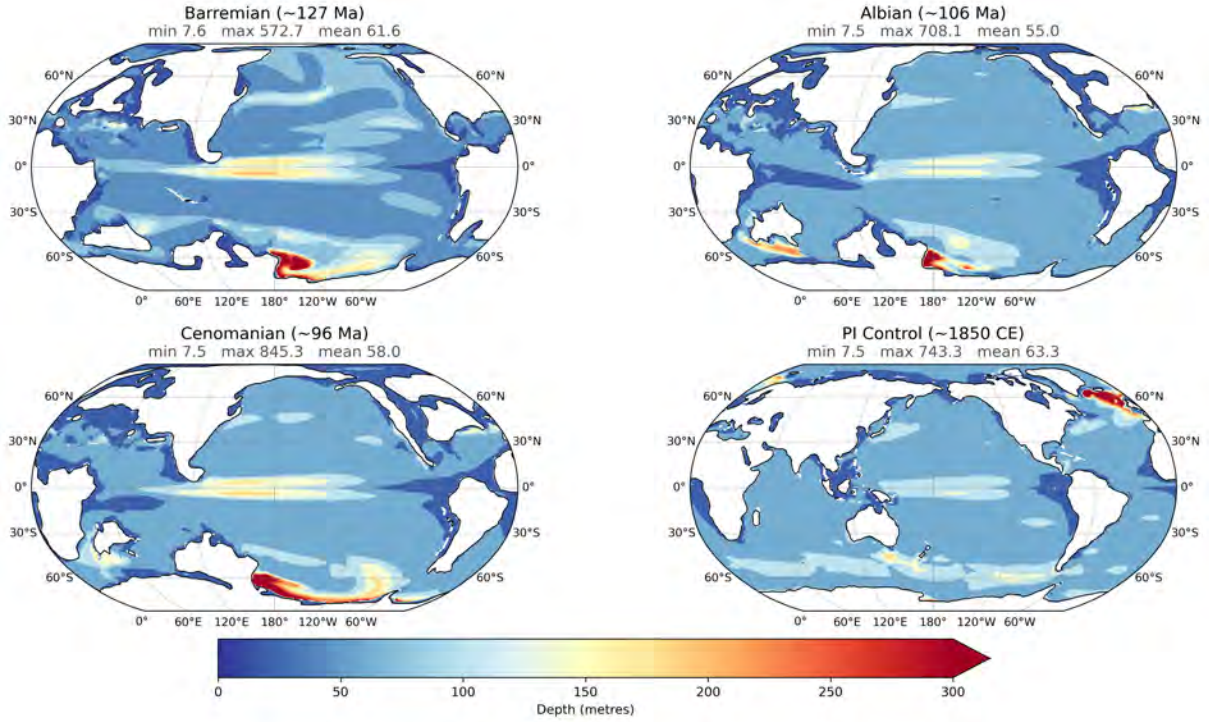

Figure 24: Simulated oceanic mixed layer depth for the Barremian (~127 Ma), Albian (~106 Ma), Cenomanian (~96 Ma) and PI control (1850 CE).

The mixed layer depth (MLD) shows the base of the ocean's mixed surface layer. Deep values indicate strong vertical mixing and are generally associated with deep-water formation. In the Cretaceous stages, there is an important deep mixed layer patch in the Southern Hemisphere, at the coast of Antarctica, 180° in longitude (Figure 24). This patch is the strongest in the Cenomanian and in the Barremian, and slightly weaker in the Albian. Another important deep mixed layer is found at the equator, particularly strong in the Barremian, weaker in the Albian and stronger again in the Cenomanian. The Barremian shows some smaller patches of MLD in the Northern Pacific, North of the Tethys and East of proto-India, although the most important one being on the coast of Antarctica. The Albian displays a weaker equatorial and Antarctic MLD (Figure 25), but has a strong MLD south of proto-India (60°S 60°E) and a notable patch at the south of North America. The Cenomanian shows a deep MLD at the equator again, although weaker than the Barremian. It also displays some patches south of proto-India (60°S 60°E) and, again, a patch at the south of North America. The most important mixed layer depth of the Cenomanian is on the coast of Antarctica, at the south of the Pacific Ocean. This deep MLD is not present in the pre-industrial simulation, where the deepest mixed layer is located in the North Atlantic, where there is the formation of the North Atlantic Deep Waters (Fallot, 2021). There are deep MLD patches south of Australia, at 180° at the coast of Antarctica and West of the southern tip of South America. The equatorial MLD observed in the Cretaceous stages is shallower during the pre-industrial. The Barremian,

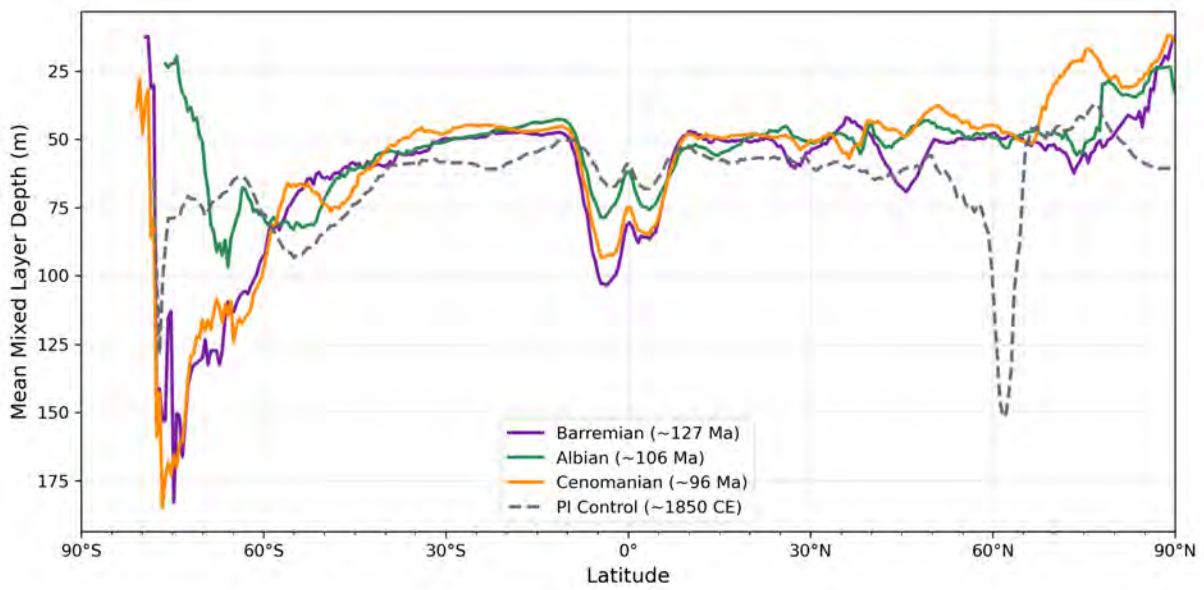

Figure 25: Zonal-mean oceanic mixed layer depth for the Barremian (~127 Ma), Albian (~106 Ma), Cenomanian (~96 Ma) and PI control (1850 CE).

the Albian and the Cenomanian show northward deepwater (~2000 metres and deeper) transport (Figure 26), consistent with the deep water being formed in the high latitudes of the Southern Hemisphere. This north travelling water rises at 30°N, at the same latitude where the zonal winds switch from eastern winds to western winds. The pre-industrial shows a stronger southward velocity band between 1000-4000 metres, with a northward velocity band at 4000 metres, from 50°S northward. The four simulations show an equatorial upwelling, consistently represented in the equatorial MLD (Figure 25), but the meridional velocity of these equatorial upwelling cells is higher for the Cretaceous stages (See appendix: Figure B.13). Between 30°N and 40°N, there is another upwelling band, showing stronger and deeper water reworking for the Cretaceous than the pre-industrial. The Cretaceous stages show a strong northward signal in the high northern latitudes, reaching deep ocean in the Barremian, and diminishing from the Albian to the Cenomanian.

5.4 Oceanic gyres

The barotropic stream function variable represents the pattern and intensity of horizontal oceanic circulation, isolating main gyres and showing the direction of the water flow. The main difference between the pre-industrial and the Cretaceous stages is the absence of the strong eastward Antarctic Circumpolar Current in the Cretaceous (Figure 27). The Cretaceous stages show similar global distribution between them, with a wide counter-clockwise North Pacific subpolar gyre, a North Pacific clockwise gyre (similar to the PI) and a strong counterclockwise Southern Pacific gyre, ranging from 60°E to 60°W in the Barremian. The Equator has alternating currents and countercurrents that extend from

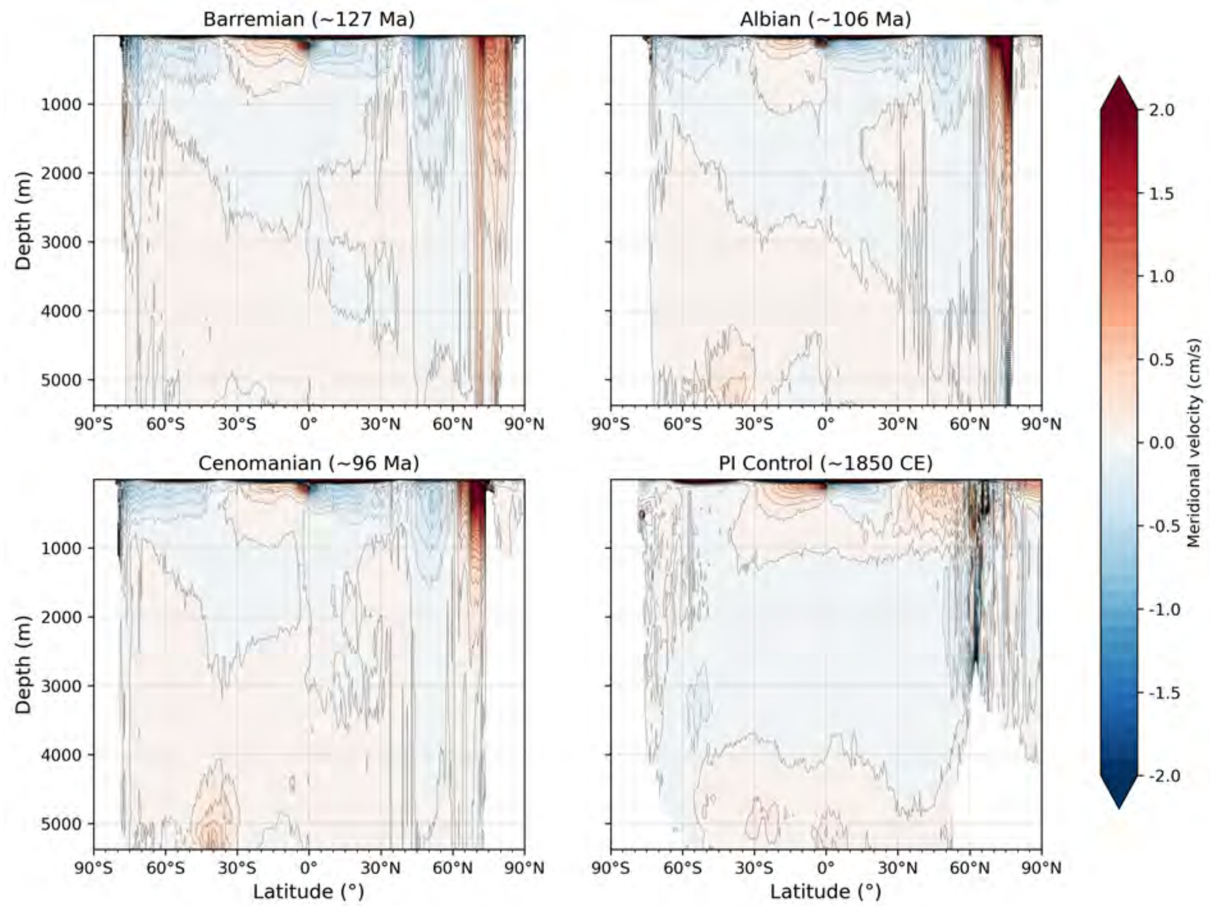

Figure 26: Zonal-mean oceanic meridional velocity per depth for the Barremian (∼127 Ma), Albian (∼106 Ma), Cenomanian (∼96 Ma) and PI control (1850 CE).

the Western Tethys to the Eastern Pacific, whereas the PI equatorial currents are closed off to the West by Australia.

The North Pacific Subpolar Gyre shows diminishing strength from the Barremian to the Cenomanian (Figure 28). The South Subpolar gyre weakens from the Barremian to the Albian (from ∼100 Sv to a bit less than ∼50 Sv), but gets stronger in the Cenomanian again (up to ∼60 Sv). The effect of the north movement of proto-Australia that gradually blocks off the South Pacific, can clearly be observed around 30°S, with a reduction of the gyre's intensity. The PI doesn't display as strong of a North Pacific Subpolar gyre, but instead shows a strong North Atlantic gyre, and, overall, has gyres in the Atlantic that are nonexistent in the Cretaceous.

5.5 Oceanic ideal age

The ideal age represents how long water has been isolated from the surface and informs on the deep-water ventilation and circulation, where old water indicates poorly ventilated water. The Cretaceous stages appear to have a much older ideal age globally (Figure 29), with the Albian having the oldest and the Cenomanian the youngest average at depth. All

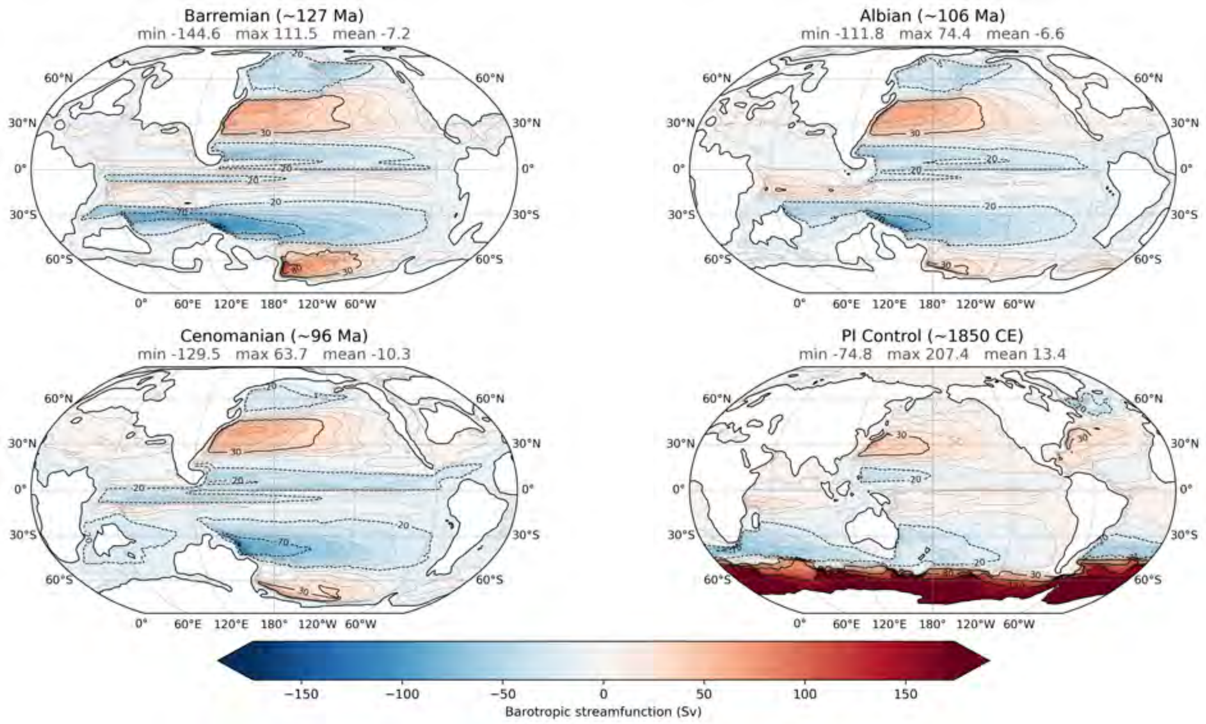

Figure 27: Simulated oceanic barotropic stream function with a contour interval of 10 Sv, for the Barremian (∼127 Ma), Albian (∼106 Ma), Cenomanian (∼96 Ma) and PI control (1850 CE). The positive values (red) indicate a clockwise rotation, where the negative values (blue) suggest counterclockwise rotation.

four simulations show an inverted "S-curve" depth profile, although the intensity changes. In the Cretaceous at 4000 metres deep, an important feature at this depth is the presence of Oceanic Ridges, in the Pacific and the Tethys, dividing what can be called "reservoirs" of different aged waters (Figure 30). Moreover, there is a South to North gradient, with southern deep ocean younger, and ideal age increasing towards higher latitudes (Figure 31). Within this gradient, the youngest waters at 4000 metres are in the South Pacific and the Antarctic coast, from 60°S and southward ($<$ 250 years), while the rest of the Pacific sits at around 800 to 1500 years and ages towards higher latitudes. The Barremian holds the oldest water in the Northern Hemisphere, from roughly 40°N to the pole, reaching up to a zonal average of 1600 years. In the Albian, the eastern Pacific (between about 120°W and 60°W) is older across all latitudes, and the proto-North Atlantic shows the oldest water. The Cenomanian broadly resembles the Albian, but with younger water in the Southern Hemisphere and a comparable pattern in the north; the proto-North Atlantic remains old, though slightly less so than in the Albian. The pre-industrial control shows much weaker north-south contrast, with ideal ages generally below 750 years.

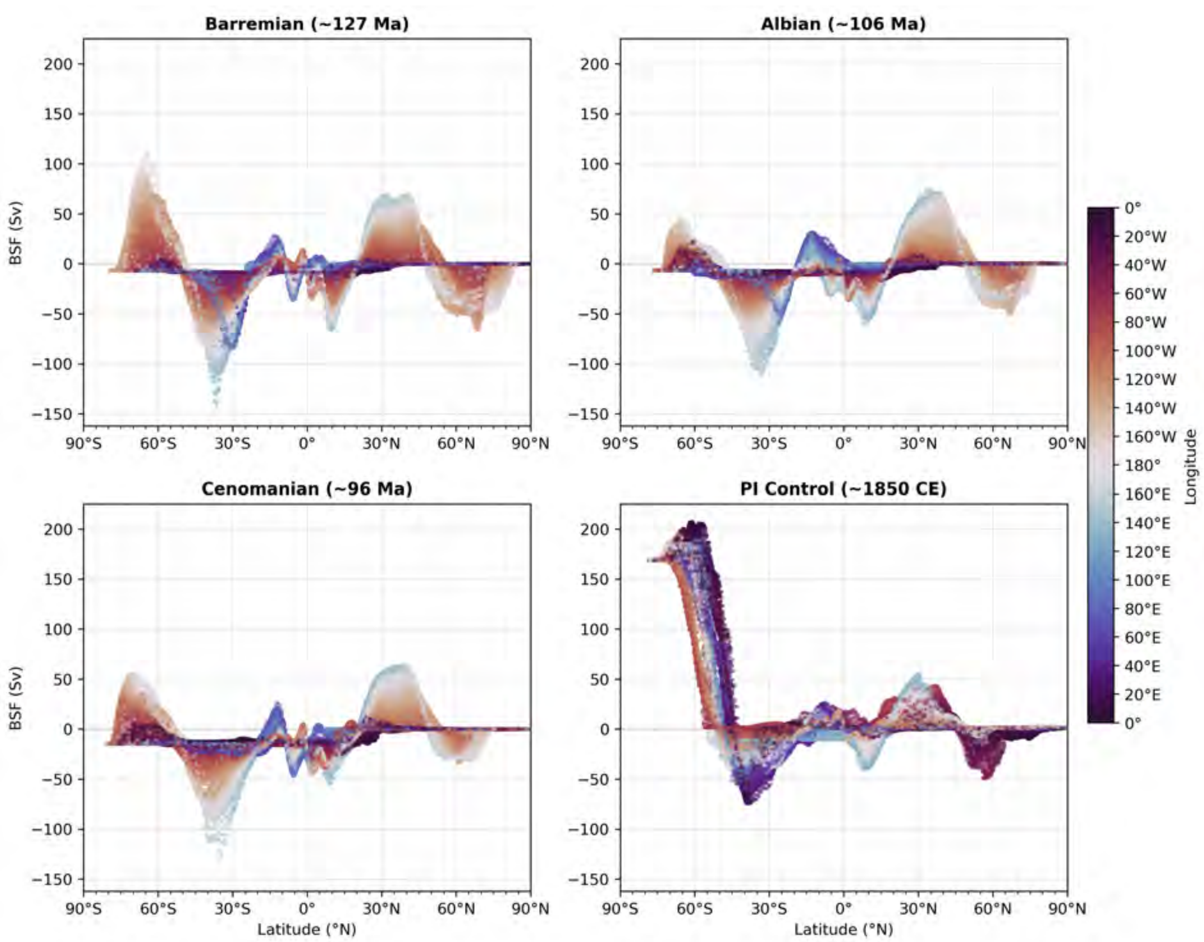

Figure 28: Simulated oceanic barotropic streamfunction as a function of latitude and longitude for the Barremian (∼127 Ma), Albian (∼106 Ma), Cenomanian (∼96 Ma) and PI control (1850 CE). Each point represents a single grid cell

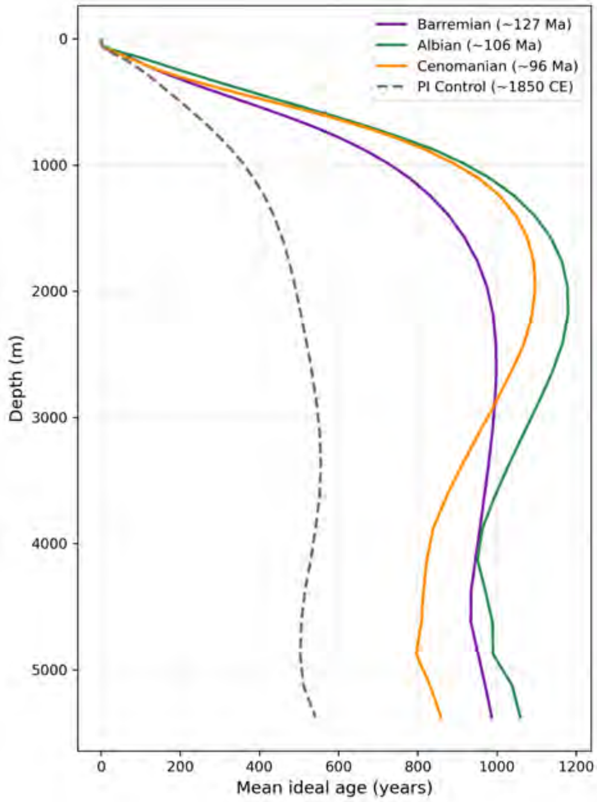

Figure 29: Simulated global mean oceanic ideal age profile for the Barremian (∼127 Ma), Albian (∼106 Ma), Cenomanian (∼96 Ma) and PI control (1850 CE).

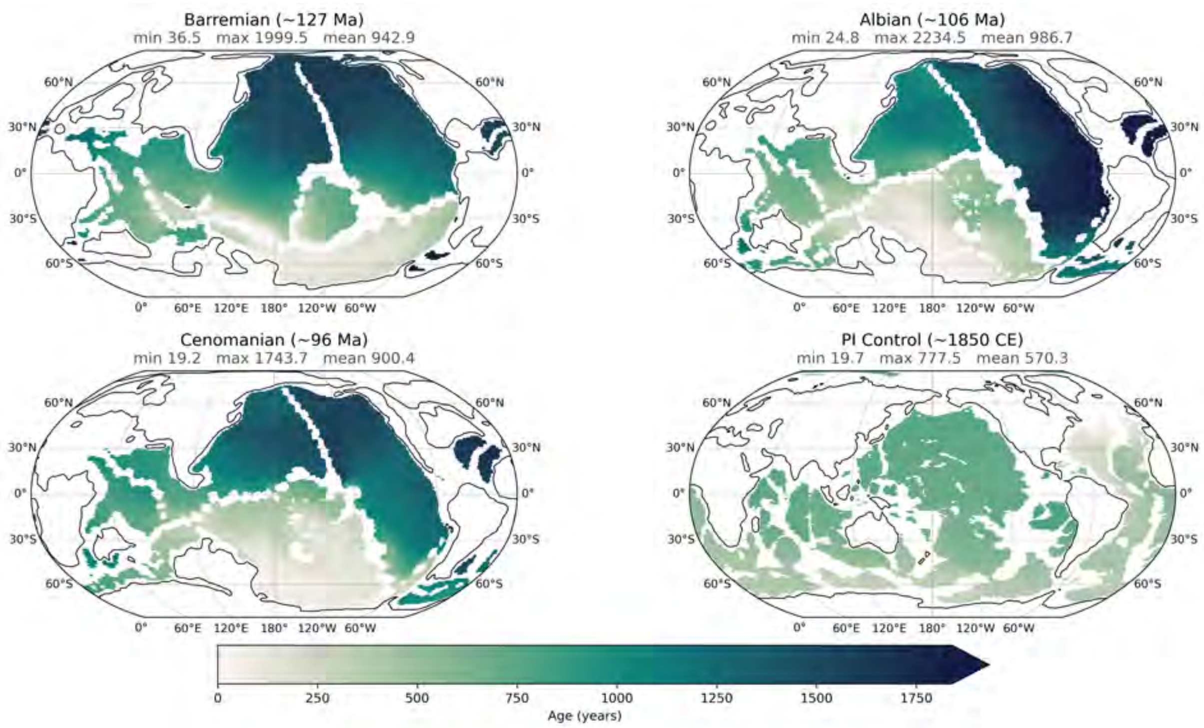

Figure 30: Simulated oceanic ideal age at 4000 metres depth for the Barremian (∼127 Ma), Albian (∼106 Ma), Cenomanian (∼96 Ma) and PI control (1850 CE).

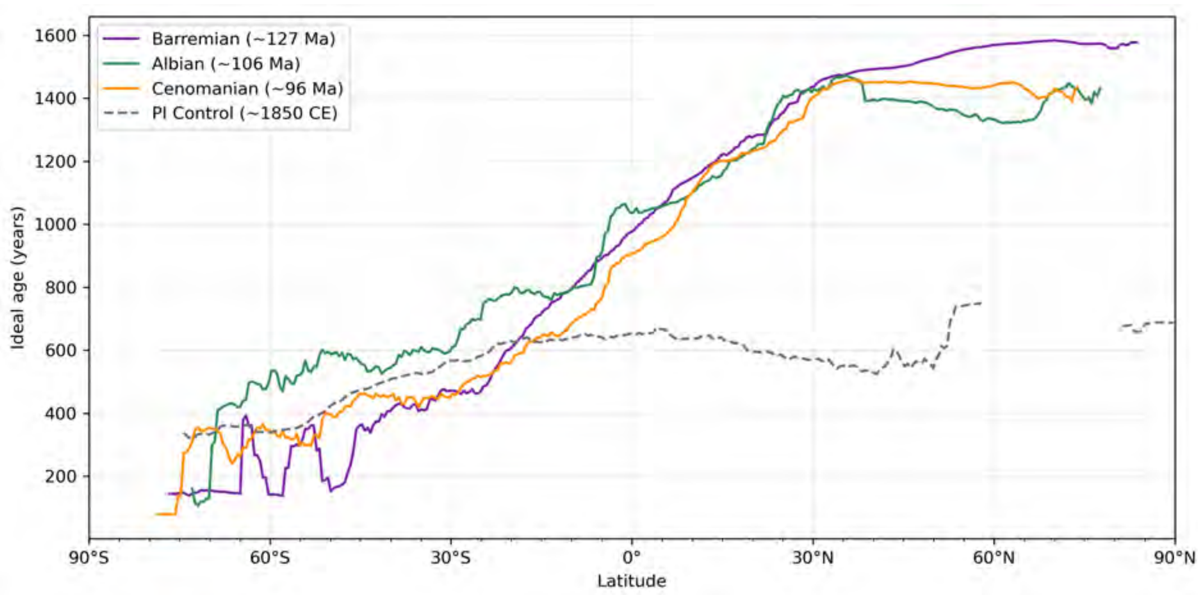

Figure 31: Simulated zonal-mean oceanic ideal age at 4000 metres depth for the Barremian (~127 Ma), Albian (~106 Ma), Cenomanian (~96 Ma) and PI control (1850 CE).

6 Discussion

The three Cretaceous stages simulated in this study, the Barremian, the Albian and the Cenomanian, share a fixed CO_2 concentration of 854 ppm. Because CO_2 is identical across these three runs, the variations in the simulated climate, such as surface air temperature or ocean circulation patterns, is due to the difference in palaeogeography and its feedbacks on the ocean and atmosphere. The inter-stage signal is therefore the cleanest basis for interpretation. As the PI run differs greatly from the Cretaceous stages not only in palaeogeography but also in CO_2 (854 versus 280 ppm), observed differences in simulated climate between these runs are therefore due to palaeogeography and greenhouse warming forcing on the atmosphere, ocean, and land cover feedbacks. The discussion below draws the atmospheric and oceanic results together along several connected threads. Three variables strongly influence the Cretaceous climate: palaeogeography distribution, CO_2 forcing and oceanic circulation (Barron et al., 1995; Lunt et al., 2016). The fixed CO_2 means that changes in the three Cretaceous time slices are palaeogeographical and oceanic. For the simulated periods, the continental configuration is an important driver of inter-stage changes. The break-up of Gondwana, the evolution of North America and Eurasia and even the northward migration of proto-Australia show strong impact on the global distribution of the climate. For instance, with the opening of the Western Interior Seaway, warm temperatures are seen in higher latitudes in the Albian (Figure 3), a result also found in other studies (Donnadieu et al., 2006). The reworking of oceanic seaways across the Barremian, Albian and Cenomanian, with North America shifting westwards, isolates the Arctic Ocean in our simulations, impacting its salinity and temperatures, while the broad Pacific Ocean of the Cretaceous stages allows wide oceanic circulation at the equator. The Cretaceous Arctic Ocean illustrates a perfect example of the palaeogeographic controls on a more enclosed level. During the Cretaceous, the Arctic Ocean is largely isolated, and the simulations show low-level salinity, dropping to ~ 5 g/kg at the pole in the Cenomanian (Figure 19). These low values are not explained by the local evaporation and precipitation relationship, suggesting that another process comes into action here, such as the limited exchange with the open ocean that may let freshwater from precipitation and continental run-off (stronger during the Cenomanian) accumulate rather than being diluted away.

One main mismatch of the model with the proxies is the simulated temperatures at the poles. Proxies estimate much warmer temperatures for the Barremian, Albian and Cenomanian and the absence of sea ice, and this is not supported by the simulations. Furthermore, the simulated pole-to-equator temperature gradient is much stronger than the proxies suggest, with the models not being able to warm the poles sufficiently. In this case, it is likely due to CO_2 levels not being sufficiently high to warm the poles. There is, however, a known behaviour in climatic models that tends not to produce high enough poles, hypothesised to result from polar land-cover configuration (as darker vegetation strongly affects albedo), high-altitude cloud parametrisation, or a model underestimation of polar warming in response to CO_2 concentration(Ladant et al., 2020; O'Brien et al., 2017; Scotese et al., 2021). The analysis run in this thesis, however, cannot distinguish them. Despite these temperature divergences with the proxy data, the simulations still show a warming trend from the Barremian to the Cenomanian, suggesting that palaeogeographical controls are, at least in part, responsible for the mid-Cretaceous warming, even though the biggest factor would be CO_2 (Ladant et al., 2020; Lunt et al., 2016). The sea ice and cold poles at 854 ppm CO_2 concentration are therefore due to a simulation limitation, producing polar sea ice and snow coverage that contradicts proxy evidence for ice-free poles (Barron & Washington, 1985; O'Brien et al., 2017). The global mean temperatures from Scotese et al. (2021) indicates temperatures of ∼19.5 °C, ∼21 °C and ∼24 °C for the Barremian, Albian and Cenomanian respectively, whereas the simulated temperatures tend to be colder: 16 °C, 17.5 °C and 17.8 °C. Those considerably lower global atmospheric temperatures are a result of processes discusses above: colder polar temperatures and CO_2 levels.

The Cretaceous stages show intriguing equatorial differences with the pre-industrial: the meridional wind circulation in the Barremian, the Albian and the Cenomanian show a small anti-Hadley at the equator (Figure 9), flowing in the opposite direction to the surrounding Hadley cells. The wide Pacific has a long uninterrupted equatorial band with no continental barriers to decelerate the trade winds, meaning the equatorial easterlies are stronger over the Pacific than the pre-industrial (Figure 7). Those stronger winds in the mid-Cretaceous equatorial latitudes drive Ekman transport poleward, producing stronger upwelling at the equator, consistent with the surface meridional velocities of the oceans and the dip in sea surface temperature at the equator (Figure 14). This low altitude reversed cell at the equator, consistent with by the temperature dip, suggests an arid equator belt over the Pacific with positive E-P during the mid-Cretaceous (Figure 18). This is consistent with Adam et al. (2023), who show that equatorial precipitation diminution and anti-Hadley circulation are features of wide ocean climates with reduced tropics-to-poles temperature gradients. The authors observed that such conditions were characteristic of the Cretaceous in their HadCM3L simulations.

In the pre-industrial, the deepest mixed layers, and therefore the main sites of deep-water formation, sit in the North Atlantic, consistent with the formation of North Atlantic Deep Water, while a closed Antarctic Circumpolar Current isolates the Southern Ocean (Figure 27). In the three mid-Cretaceous time slices, this pattern is displaced southward: the deepest mixed layers are found along the Antarctic coast (Figure 24), meaning that deep water formation shifted to the southern high latitudes, highly supported by the simulated ideal age. The absence of the circumpolar current is likely due to the continental configuration, as the proto-Australia landmass leaves no continuous circumpolar oceanic band. In contrast, the broad Tethys-Pacific connection allows the equatorial waters to flow across the wide equatorial palaeocurrent, a circulation closed off to the west by Australia in the pre-industrial. The decrease in the Northern Hemisphere Subpolar Gyre intensity across the mid-Cretaceous is thought to cause a decrease in poleward ocean heat transport (Gianchandani et al., 2023). An interesting feature found across multiple components, such as oceanic temperatures at depth, evaporation and salinity, is the flow of the proto-North Atlantic warm, salty waters into the Eastern Pacific in the Barremian, the Albian and the Cenomanian. In the pre-industrial, the Pacific Ocean is much more enclosed and the circulation with the Northern Atlantic is cut off.

The ideal age variable is consistent with this circulation change in deep waters. The globally older mid-Cretaceous deep oceans contrast with the pre-industrial, indicating reduced ventilation of the deep ocean circulation overall. It should be noted that the pre-industrial simulation may have been run for a shorter duration, possibly around 800 years, explaining the difference in ideal age. However, as CESM1.2 is a legacy model, much of the associated documentation is difficult to find, and the exact spin-up length could not be confirmed, meaning that the inter-stage comparison is the clean signal. At 4000 metres, the youngest waters of the mid-Cretaceous stages are found in the South Pacific and along the Antarctic coast, while the proto-North Atlantic produces the oldest water (Figure 30). This south-north age gradient explains the ventilation pattern associated with the shift in deep water formation, discussed above, where the southern high latitudes are well ventilated, and the northern waters are poorly ventilated in the mid-Cretaceous. A poorly ventilated deep ocean is more favourable to low oxygen levels, and the older deep mid-Cretaceous ocean shows settings favourable to the development of Oceanic Anoxic Events, which is consistent with the recurrent OAE of the mid-Cretaceous (Bottini & Erba, 2018; Wilson & Norris, 2001). Our mid-Cretaceous simulations show similar high salinity and isolated proto-Atlantic. Other studies have found that the continental reworking of the late Cretaceous, more precisely the opening of the Caribbean gateway and the development of a westward flow, is believed to explain the shift to a better ventilated ocean, less prone to OAEs (Donnadieu et al., 2016). Friedrich et al. (2008) identified high-salinity proto-Atlantic waters and the relative isolation of mid-Cretaceous basins as significant drivers of anoxia and black-shale deposition in the proto-North Atlantic. Our simulations are broadly consistent with this interpretation: the mid-Cretaceous stages show high salinity, restricted exchange in the proto-Atlantic (Figure 23) and reduced ventilation (Figure 30), conditions that would have favoured oxygen depletion. The subsequent shift toward a better-ventilated ocean, less prone to OAEs, has been attributed to the opening of the Caribbean gateway and the establishment of a westward flow during the late Cretaceous (Donnadieu et al., 2016).

Taken together, these results point to continental configuration as the primary control on the differences between the three mid-Cretaceous stages, and largely on the differences between the mid-Cretaceous and the pre-industrial period. Across the three mid-Cretaceous runs, the warming from the Barremian to the Cenomanian, the southward displacement of deep-water formation, the broad equatorial Tethys-Pacific circulation and the isolation of the Arctic all follow from the position of the continents and the configuration of ocean gateways rather than from a change in CO_2 forcing. The largest of these climate reorganisations thus involve the ocean, mirroring the hypothesis that stage-to-stage changes in the Cretaceous greenhouse are closely tied to shifts in ocean circulation (Lunt et al., 2016).

7 Conclusion

The thesis set out to evaluate the ocean circulation and climate of the mid-Cretaceous, asking why the period is of interest, how the climate compares with the present day, and how the simulations relate to the existing literature. These questions were investigated through a model-based comparison of three geological stages, the Barremian (∼127 Ma), the Albian (∼106 Ma) and the Cenomanian (∼96 Ma), against a pre-industrial control by using the CESM1.2 model (Renoult et al., Accepted), with the CO_2 concentration fixed at 854 ppm across the three Cretaceous runs. Because the greenhouse concentration is identical across these runs, the inter-stage differences result from non-CO_2 forcings.

The central finding is that the simulated mid-Cretaceous ocean operated with a circulation structure considerably different from the pre-industrial. Deep water formed at the southern high latitudes along the Antarctic coast rather than in the North Atlantic, no Antarctic Circumpolar Current developed in the absence of a continuous circumpolar band, and a broad equatorial flow connected the Tethys and the Pacific. This regime results from the position of the continents and the geometry of the ocean gateways, and it is consistent across the mixed layer depth, meridional velocity, barotropic stream function and ideal age fields, which all describe the same southern-sourced and wide-ocean circulation. The simulated mid-Cretaceous deep ocean is globally older and less ventilated than the pre-industrial, with a south-to-north age gradient. The saline and weakly ventilated proto-North Atlantic contrasts with well-ventilated southern waters. This suggests conditions favourable for the recurrent Oceanic Anoxic Events of the Cretaceous, since a restricted, poorly ventilated and saline basin is optimal for oxygen depletion and black-shale deposition (Donnadieu et al., 2016; Friedrich et al., 2008). The mid-Cretaceous stages wide equatorial Pacific show a low-altitude anti-Hadley cell between the two Hadley cells, with stronger equatorial easterlies, increased upwelling and a dip in equatorial sea surface temperature. Across the three mid-Cretaceous stages, the simulations also reproduce a warming from the Barremian to the Cenomanian that is consistent with the trend indicated by proxy reconstructions (O'Brien et al., 2017) despite the constant CO_2. However, the simulated poles remain too cold, retaining snow and sea ice at 854 ppm, which show the principal limit of the model's consistency with the proxy record.

The simulations presented here provide a foundation for several directions of further investigation. A first step would be to repeat the Cretaceous runs at a higher CO_2 concentration to test whether the polar temperature difference persists, which would help distinguish a genuine model limitation from an insufficiently strong greenhouse forcing. Extending the spin-up time, particularly for the pre-industrial control, would improve deep-ocean equilibration and allow a better comparison of the ideal age of the ocean. The ocean circulation could be evaluated more directly by computing the meridional overturning streamfunction, allowing a more complete analysis of the oceanic circulation. The link between the reduced deep-ocean ventilation found in these simulations and the occurrence of Oceanic Anoxic Events could be tested directly using a coupled biogeochemical model, rather than deduced from ideal age, salinity, and isolation. Finally, a more focused analysis of the observed equatorial anti-Hadley cell would help establish the mechanism linking the wide Pacific, equatorial upwelling and the simulated sea surface temperature dip.

Use of AI

A generative AI model was used for Python debugging, particularly with issues about subplot layout. LanguageTool was used as a grammar and spell checker.

References

Adam, O., Farnsworth, A., & Lunt, D. J. (2023). Modality of the Tropical Rain Belt across Models and Simulated Climates. *Journal of Climate*, *36*(5), 1331–1345. https://doi.org/10.1175/JCLI-D-22-0521.1

Barron, E. J., Fawcett, P. J., Peterson, W. H., Pollard, D., & Thompson, S. L. (1995). A "simulation" of Mid-Cretaceous climate. *Paleoceanography*, *10*(5), 953–962. https://doi.org/10.1029/95PA01624

Barron, E. J., & Washington, W. M. (1985). Warm Cretaceous Climates: High Atmospheric CO2 as a Plausible Mechanism. In *The Carbon Cycle and Atmospheric CO2: Natural Variations Archean to Present* (pp. 546–553). American Geophysical Union (AGU). https://doi.org/10.1029/GM032p0546

Bottini, C., & Erba, E. (2018). Mid-Cretaceous paleoenvironmental changes in the western Tethys. *Climate of the Past*, *14*(8), 1147–1163. https://doi.org/10.5194/cp-14-1147-2018

Cantrill, D. J., & Poole, I. (2012, November). *The Vegetation of Antarctica through Geological Time* (1st ed.). Cambridge University Press. https://doi.org/10.1017/CBO9781139024990

Donnadieu, Y., Pierrehumbert, R., Jacob, R., & Fluteau, F. (2006). Modelling the primary control of paleogeography on Cretaceous climate. *Earth and Planetary Science Letters*, *248*(1-2), 426–437. https://doi.org/10.1016/j.epsl.2006.06.007

Donnadieu, Y., Pucéat, E., Moiroud, M., Guillocheau, F., & Deconinck, J. F. (2016). A better-ventilated ocean triggered by Late Cretaceous changes in continental configuration. *Nature Communications*, *7*(1), 10316. https://doi.org/10.1038/ncomms10316

Fallot, J.-M. (2021). Cours de climatologie [Course document, Institut de Géographie et Durabilité, Université de Lausanne].

Friedrich, O., Erbacher, J., Moriya, K., Wilson, P. A., & Kuhnert, H. (2008). Warm saline intermediate waters in the Cretaceous tropical Atlantic Ocean. *Nature Geoscience*, *1*(7), 453–457. https://doi.org/10.1038/ngeo217

Gianchandani, K., Maor, S., Adam, O., Farnsworth, A., Gildor, H., Lunt, D. J., & Paldor, N. (2023). Effects of paleogeographic changes and CO2 variability on northern mid-latitudinal temperature gradients in the Cretaceous. *Nature Communications*, *14*(1), 5193. https://doi.org/10.1038/s41467-023-40905-7

Huber, B. T., Hodell, D. A., & Hamilton, C. P. (1995). Middle–Late Cretaceous climate of the southern high latitudes: Stable isotopic evidence for minimal equator-to-pole thermal gradients. *GSA Bulletin*, *107*(10), 1164–1191. https://doi.org/10.1130/0016-7606(1995)107<1164:MLCCOT>2.3.CO;2

International Chronostratigraphic Chart. (2026).

Ladant, J.-B., Poulsen, C. J., Fluteau, F., Tabor, C. R., MacLeod, K. G., Martin, E. E., Haynes, S. J., & Rostami, M. A. (2020). Paleogeographic controls on the evolution of Late Cretaceous ocean circulation. *Climate of the Past*, *16*(3), 973–1006. https://doi.org/10.5194/cp-16-973-2020

Loeb, N., & Gnegy, E. (2024). Ask a Climate Expert: How do I use netCDF files?

Lunt, D. J., Farnsworth, A., Loptson, C., Foster, G. L., Markwick, P., O'Brien, C. L., Pancost, R. D., Robinson, S. A., & Wrobel, N. (2016). Palaeogeographic controls on climate and proxy interpretation. *Climate of the Past*, *12*(5), 1181–1198. https://doi.org/10.5194/cp-12-1181-2016

Miall, A. D., & Catuneanu, O. (2019). The Western Interior Basin. In *The Sedimentary Basins of the United States and Canada* (pp. 401–443). Elsevier. https://doi.org/10.1016/B978-0-444-63895-3.00009-7

O'Brien, C. L., Robinson, S. A., Pancost, R. D., Sinninghe Damsté, J. S., Schouten, S., Lunt, D. J., Alsenz, H., Bornemann, A., Bottini, C., Brassell, S. C., Farnsworth, A., Forster, A., Huber, B. T., Inglis, G. N., Jenkyns, H. C., Linnert, C., Littler, K., Markwick, P., McAnena, A., … Wrobel, N. E. (2017). Cretaceous sea-surface temperature evolution: Constraints from TEX86 and planktonic foraminiferal oxygen isotopes. *Earth-Science Reviews*, *172*, 224–247. https://doi.org/10.1016/j.earscirev.2017.07.012

Renoult, M., de Boer, A., Berntell, E., & Jagdish Naik, T. (Accepted). Shaping the mid-Miocene warmth: A sensitivity study on paleogeography, CO2 and model physics.

Ruddiman, W. F. (2014). *Earth's climate: Past and future* (Third edition). W.H. Freeman and Company.

Scotese, C. R., Song, H., Mills, B. J., & Van Der Meer, D. G. (2021). Phanerozoic paleotemperatures: The earth's changing climate during the last 540 million years. *Earth-Science Reviews*, *215*, 103503. https://doi.org/10.1016/j.earscirev.2021.103503

Takashima, R., Nishi, H., Yamanaka, T., Tomosugi, T., Fernando, A. G., Tanabe, K., Moriya, K., Kawabe, F., & Hayashi, K. (2011). Prevailing oxic environments in the Pacific Ocean during the mid-Cretaceous Oceanic Anoxic Event 2. *Nature Communications*, *2*(1), 234. https://doi.org/10.1038/ncomms1233

Wilson, P. A., & Norris, R. D. (2001). Warm tropical ocean surface and global anoxia during the mid-Cretaceous period. *Nature*, *412*(6845), 425–429. https://doi.org/10.1038/35086553

A Supplementary Atmospheric Figures

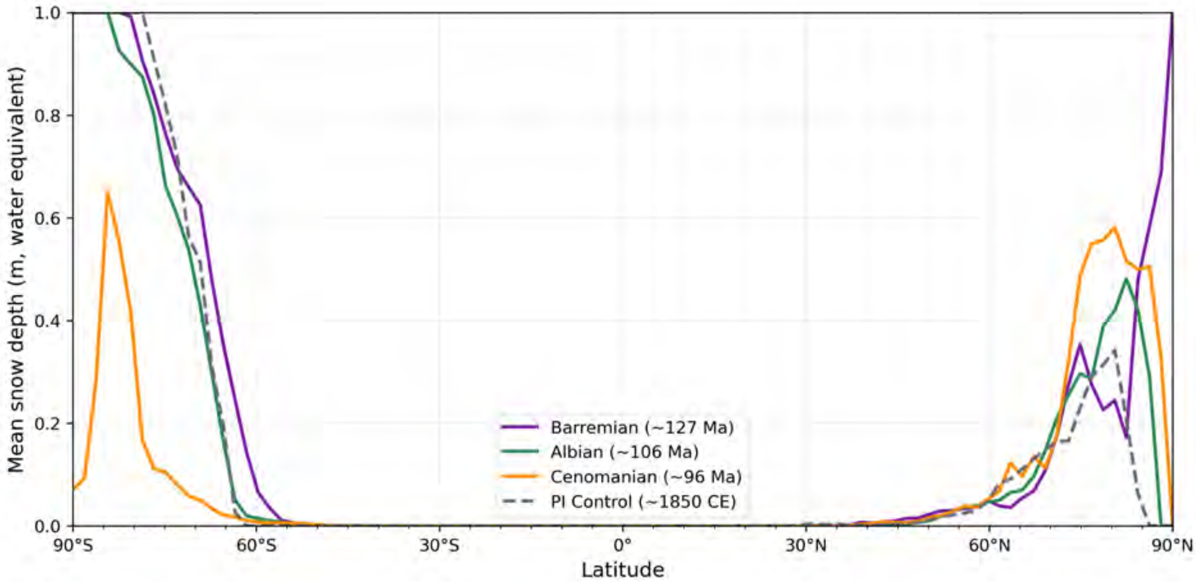

Figure A.1: Simulated land zonal mean snow coverage as water equivalent depth for the Barremian (∼127 Ma), Albian (∼106 Ma), Cenomanian (∼96 Ma) and PI control (1850 CE).

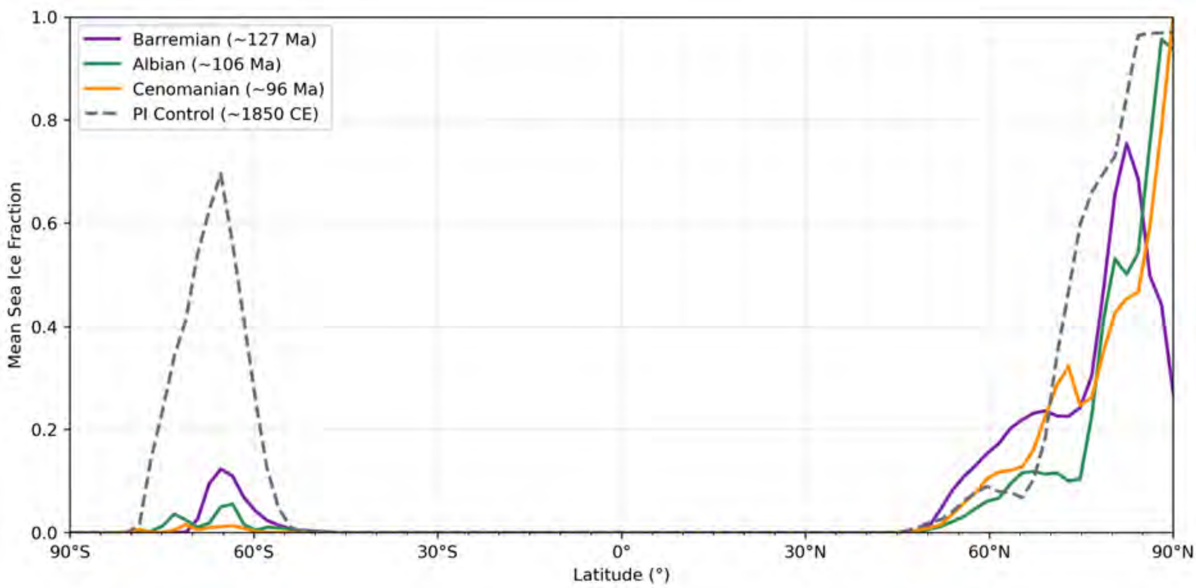

Figure A.2: Simulated zonal mean sea ice coverage for the Barremian (∼127 Ma), Albian (∼106 Ma), Cenomanian (∼96 Ma) and PI control (1850 CE).

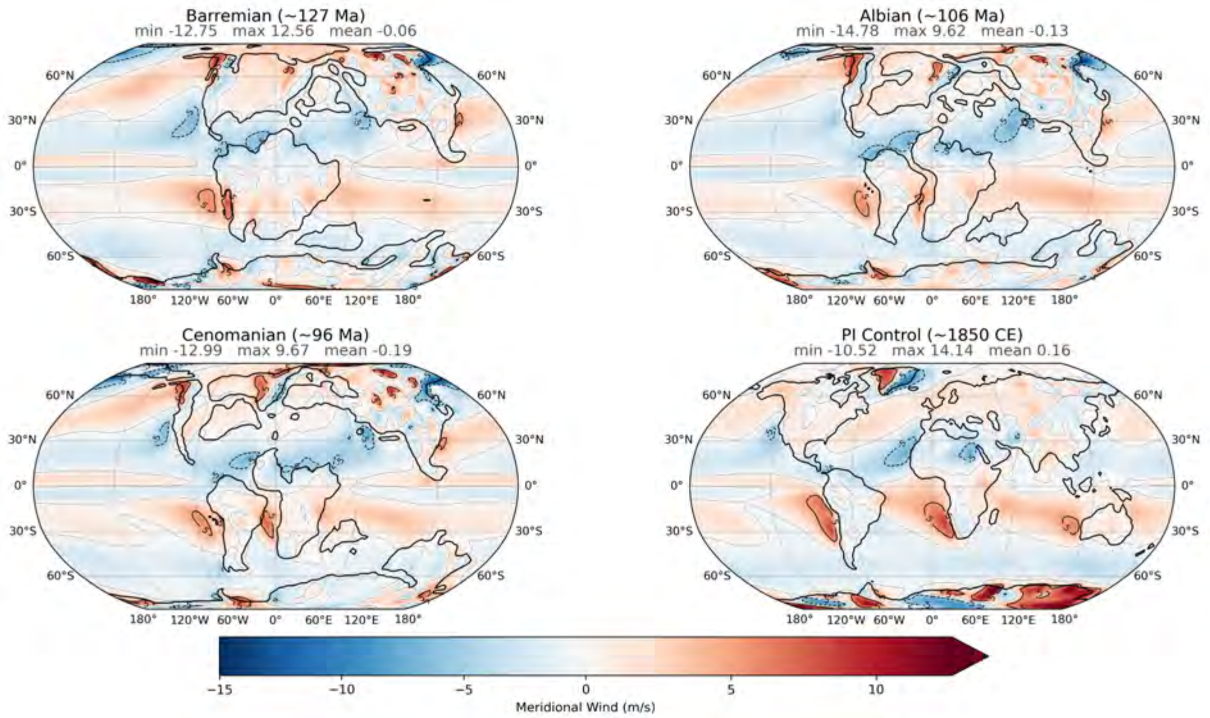

Figure A.3: Simulated atmospheric meridional winds for the Barremian (~127 Ma), Albian (~106 Ma), Cenomanian (~96 Ma) and PI control (1850 CE).

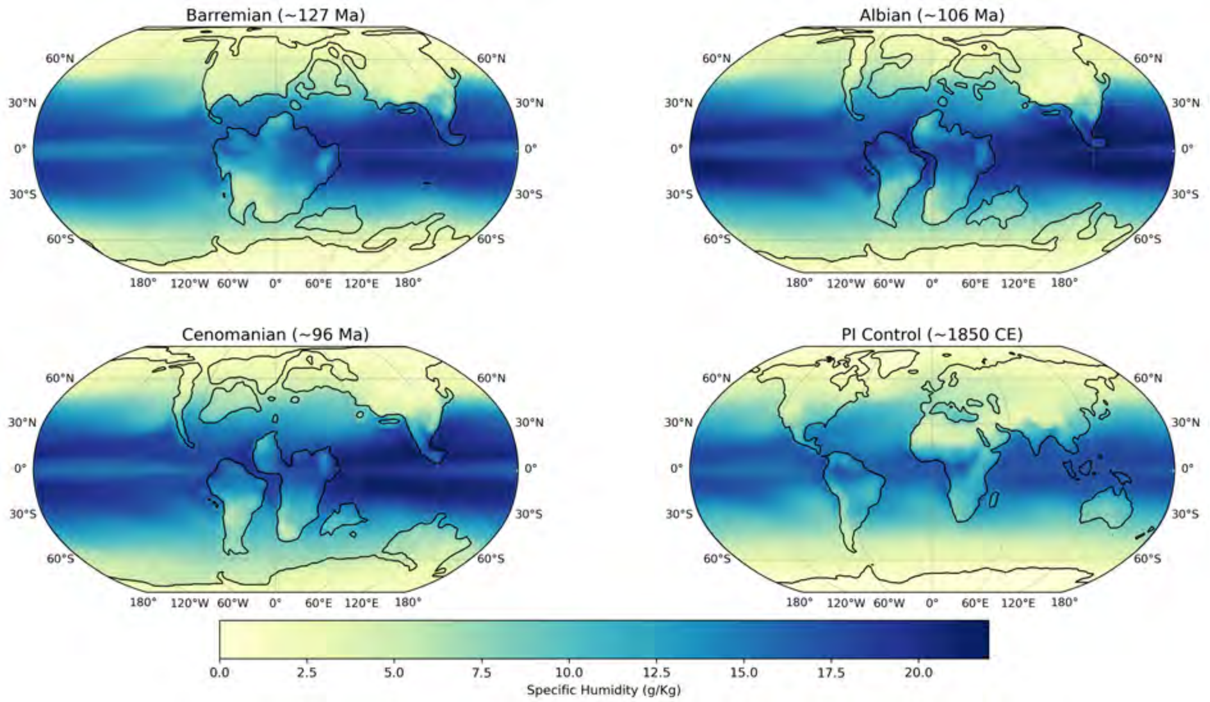

Figure A.4: Simulated atmospheric surface specific humidity for the Barremian (~127 Ma), Albian (~106 Ma), Cenomanian (~96 Ma) and PI control (1850 CE).

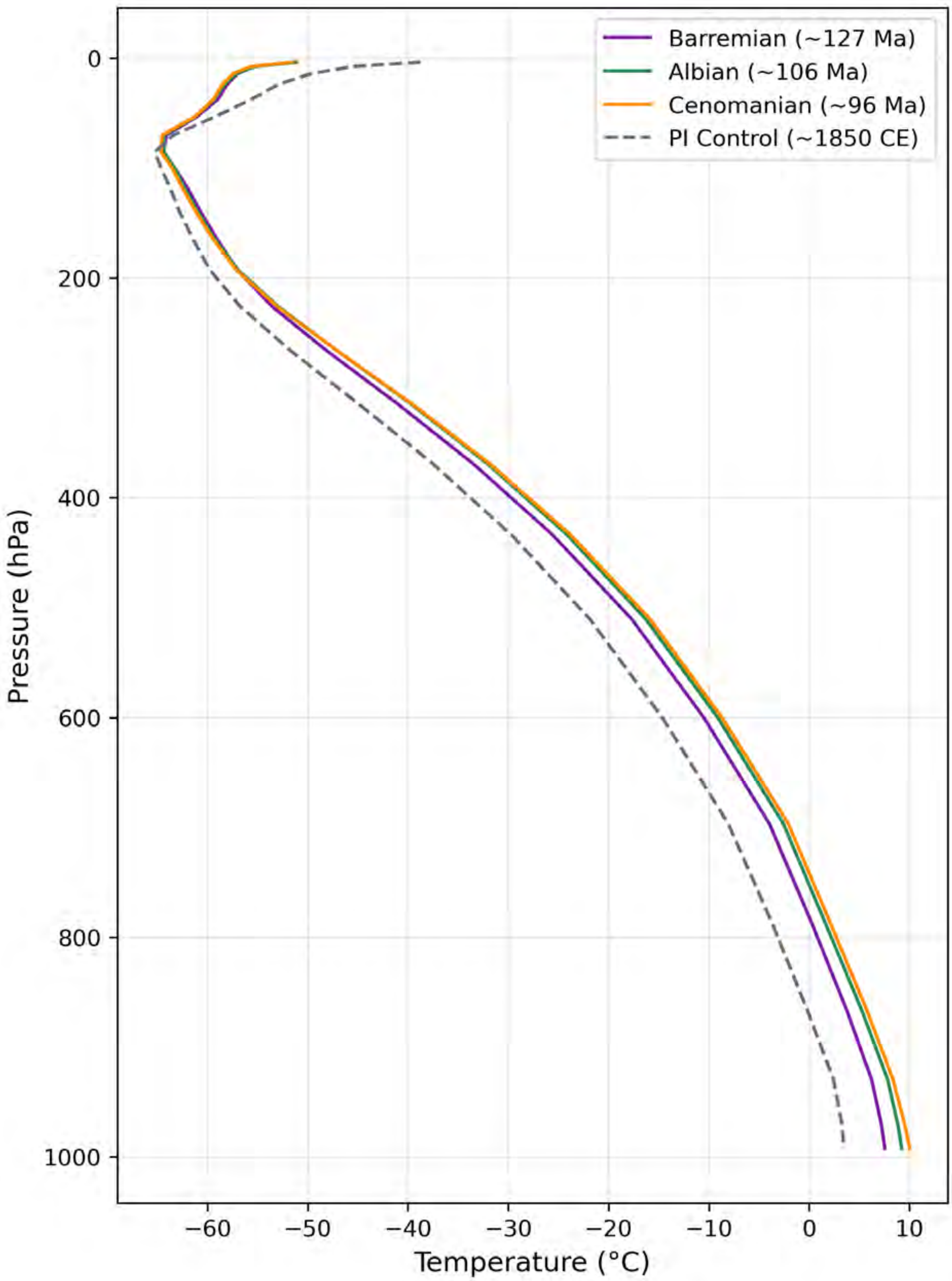

Figure A.5: Simulated atmospheric global temperatures profile by pressure for the Barremian (∼127 Ma), Albian (∼106 Ma), Cenomanian (∼96 Ma) and PI control (1850 CE)

B Supplementary Ocean Figures

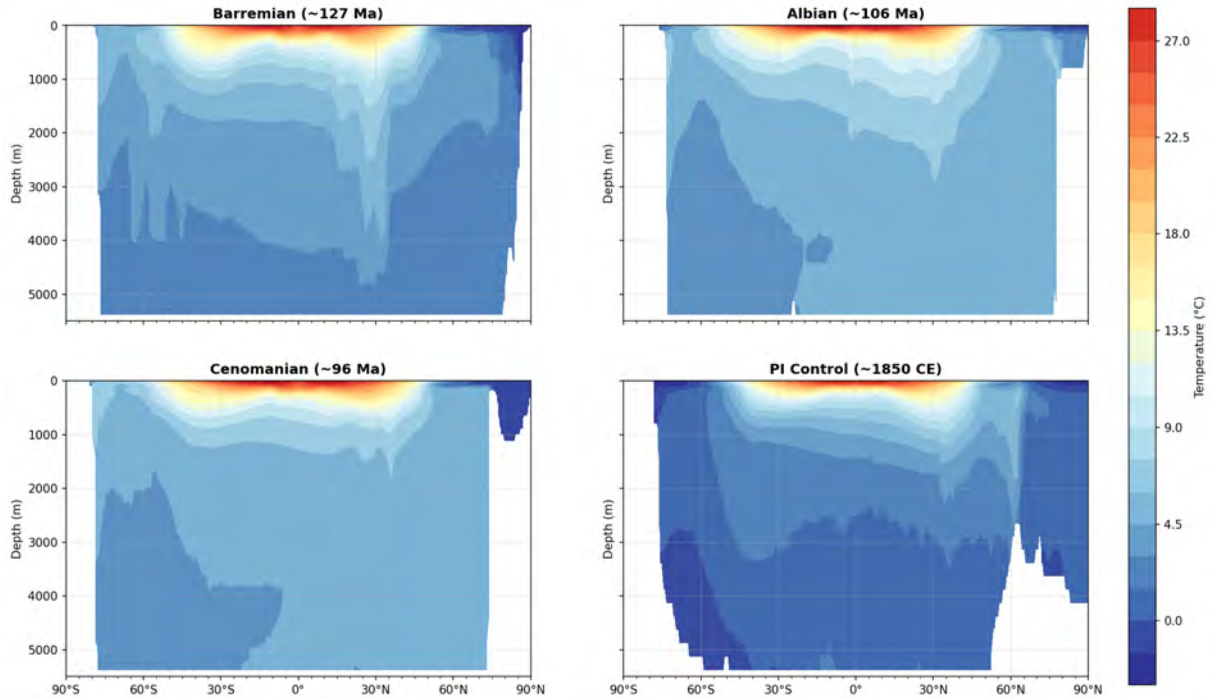

Figure B.1: Simulated oceanic zonal mean temperature as a function of latitude and depth for the Barremian (~127 Ma), Albian (~106 Ma), Cenomanian (~96 Ma) and PI control (1850 CE).

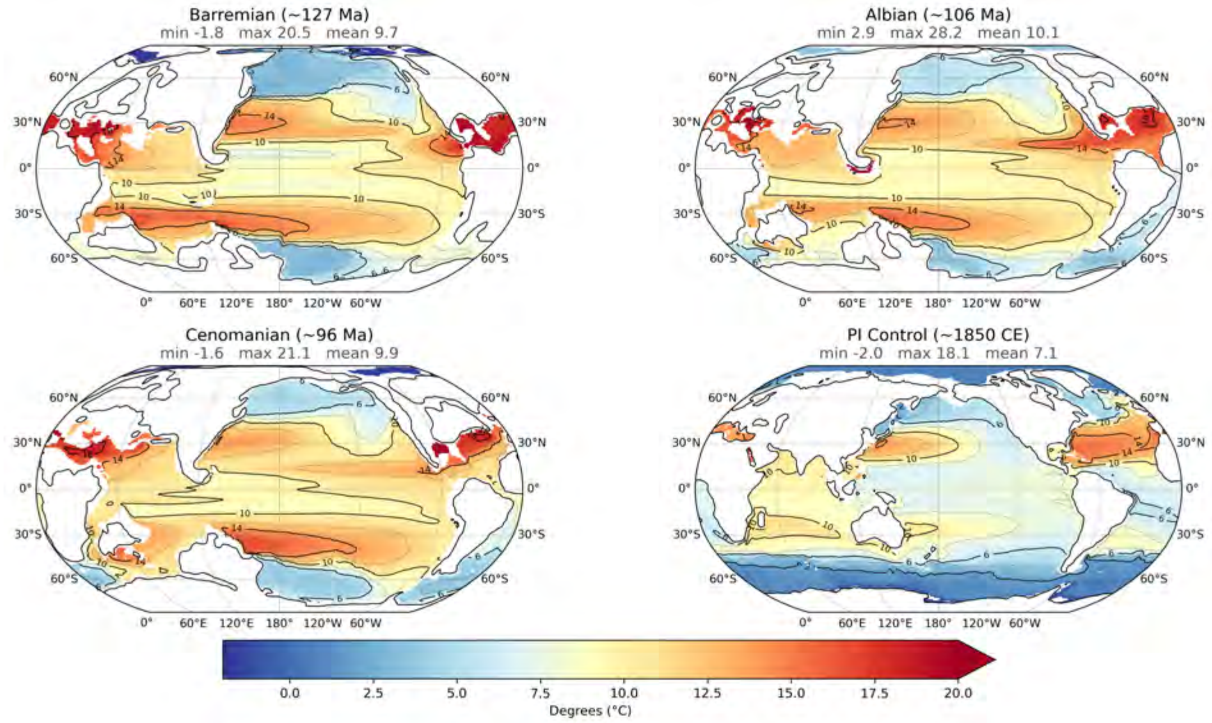

Figure B.2: Simulated oceanic temperature at 500 metres depth for the Barremian (~127 Ma), Albian (~106 Ma), Cenomanian (~96 Ma) and PI control (1850 CE).

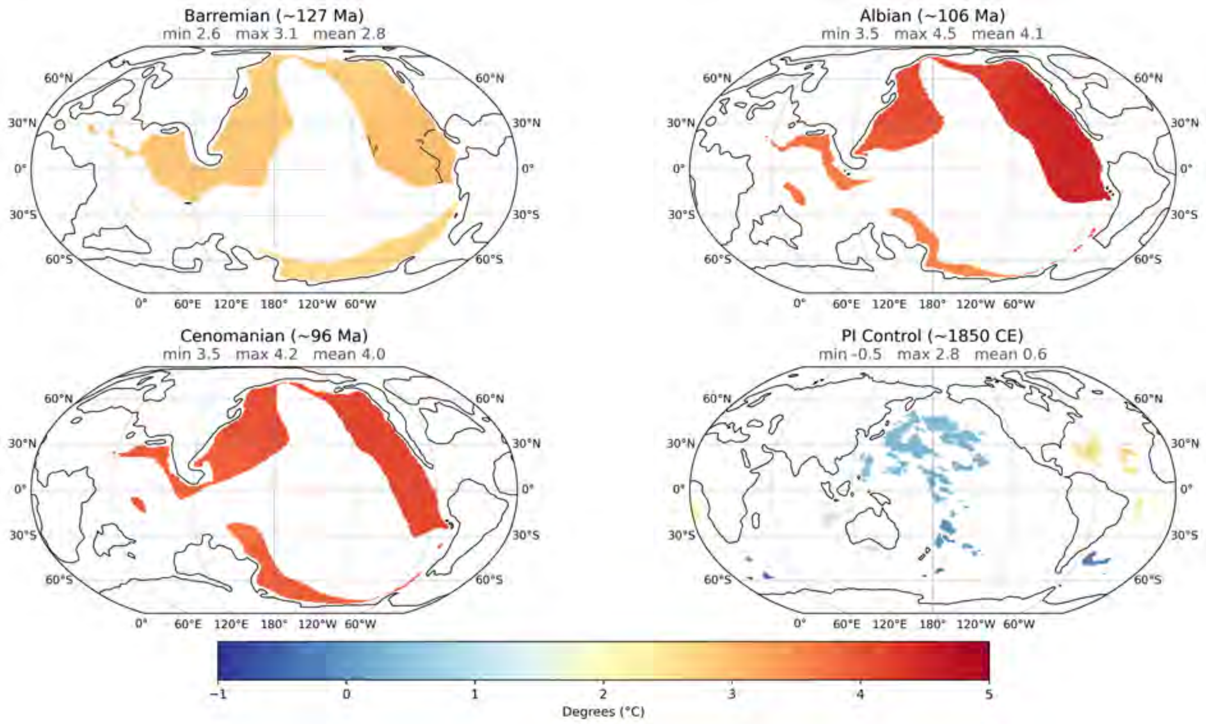

Figure B.3: Simulated oceanic temperature at 5000 metres depth for the Barremian (∼127 Ma), Albian (∼106 Ma), Cenomanian (∼96 Ma) and PI control (1850 CE).

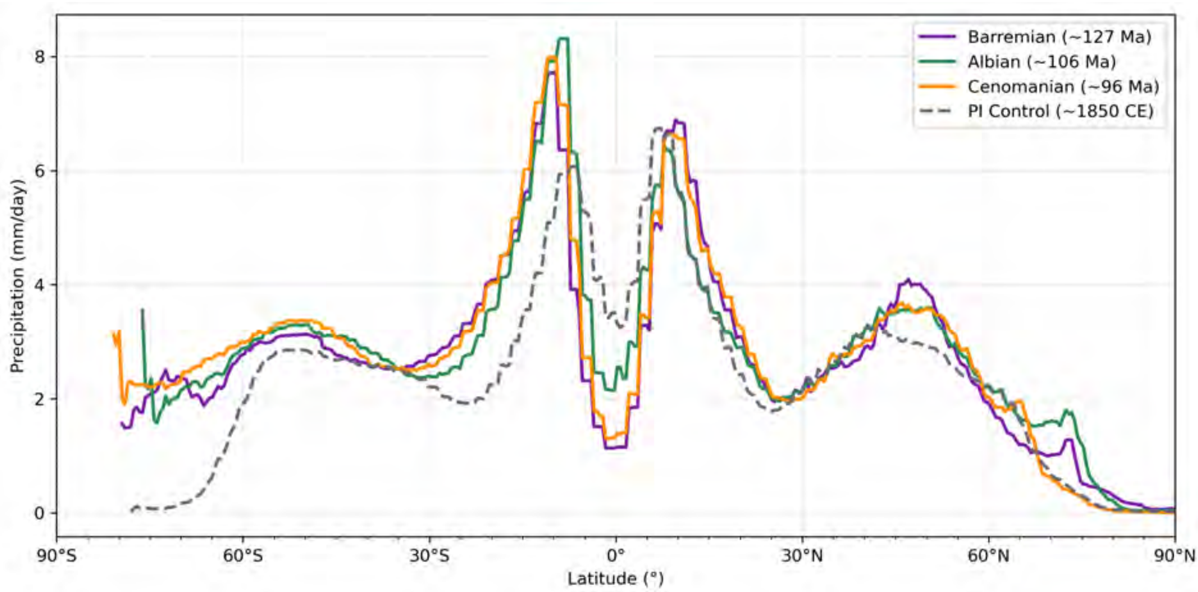

Figure B.4: Simulated oceanic zonal mean precipitation for the Barremian (∼127 Ma), Albian (∼106 Ma), Cenomanian (∼96 Ma) and PI control (1850 CE).

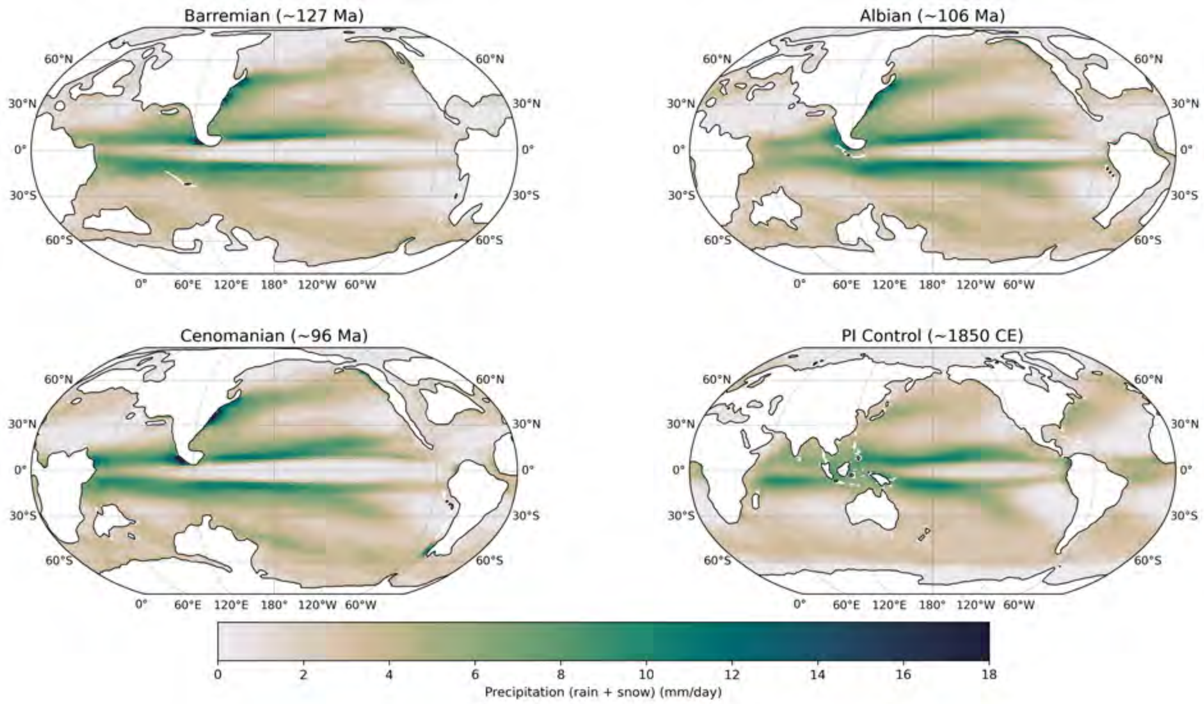

Figure B.5: Simulated oceanic precipitation for the Barremian (∼127 Ma), Albian (∼106 Ma), Cenomanian (∼96 Ma) and PI control (1850 CE)

.

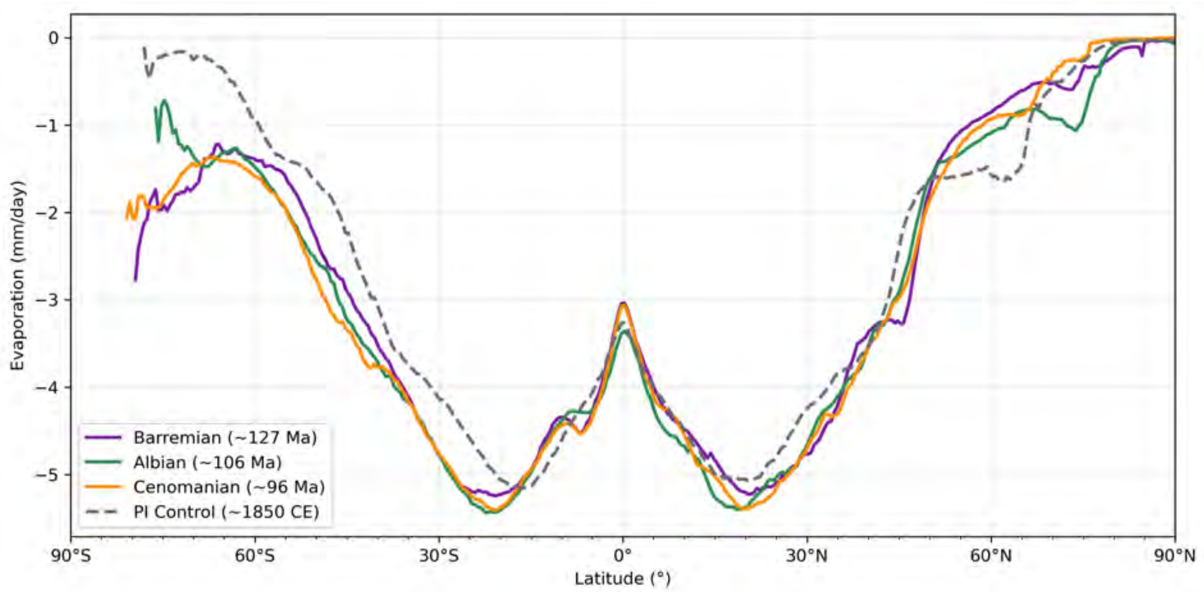

Figure B.6: Simulated oceanic zonal mean evaporation for the Barremian (∼127 Ma), Albian (∼106 Ma), Cenomanian (∼96 Ma) and PI control (1850 CE).

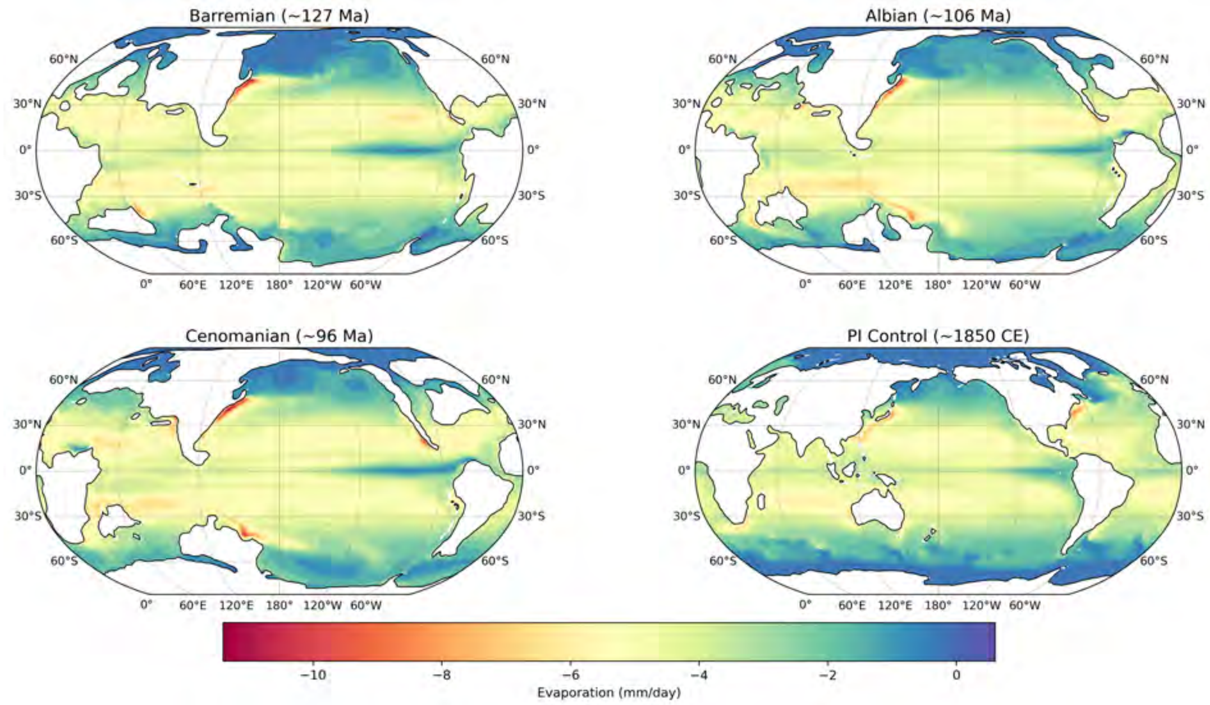

Figure B.7: Simulated oceanic evaporation for the Barremian (~127 Ma), Albian (~106 Ma), Cenomanian (~96 Ma) and PI control (1850 CE).

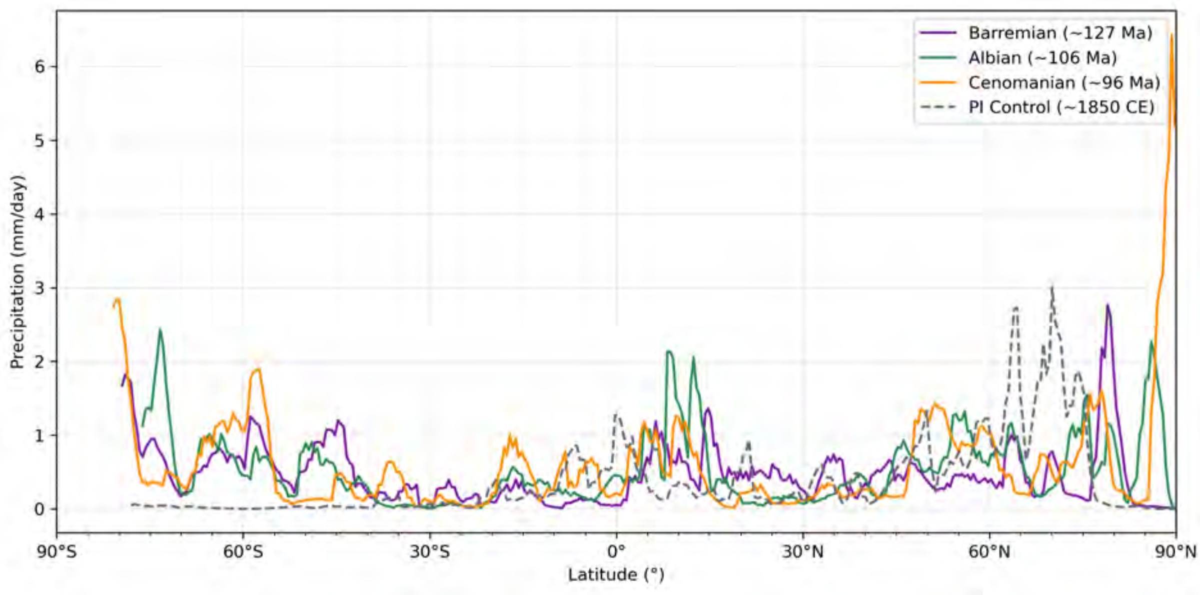

Figure B.8: Simulated oceanic zonal mean run-off for the Barremian (~127 Ma), Albian (~106 Ma), Cenomanian (~96 Ma) and PI control (1850 CE).

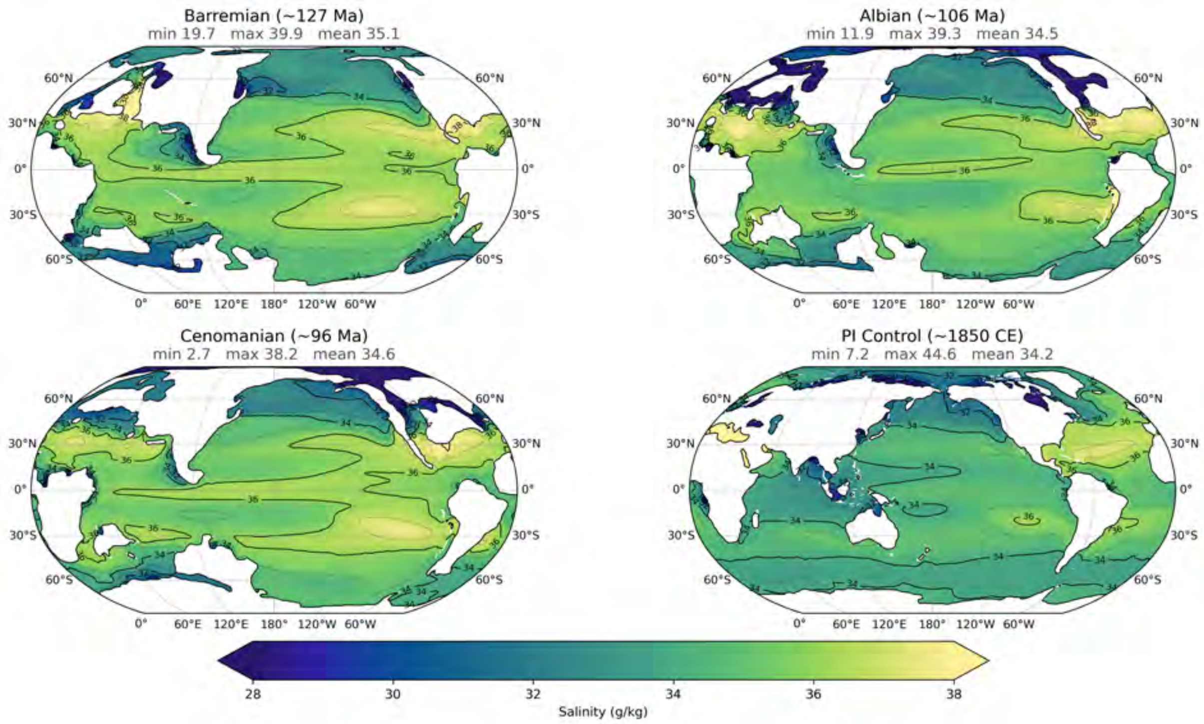

Figure B.9: Simulated oceanic surface salinity for the Barremian (∼127 Ma), Albian (∼106 Ma), Cenomanian (∼96 Ma) and PI control (1850 CE)

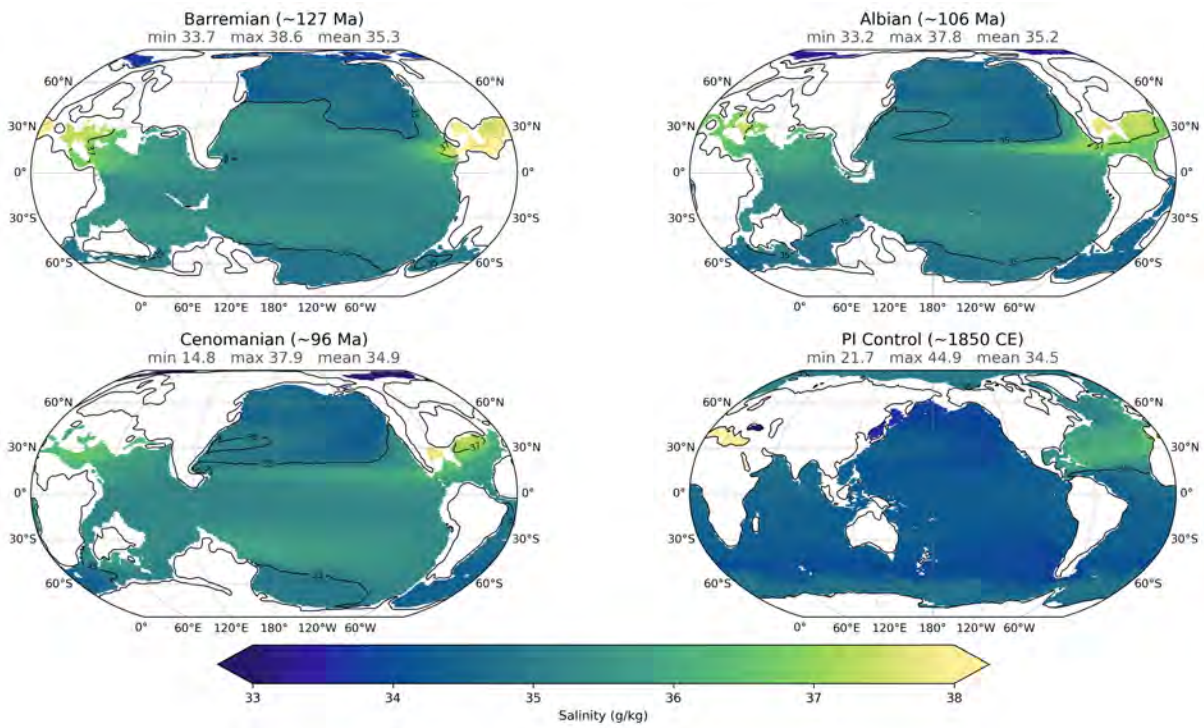

Figure B.10: Simulated oceanic salinity at 500 metres depth for the Barremian (∼127 Ma), Albian (∼106 Ma), Cenomanian (∼96 Ma) and PI control (1850 CE)

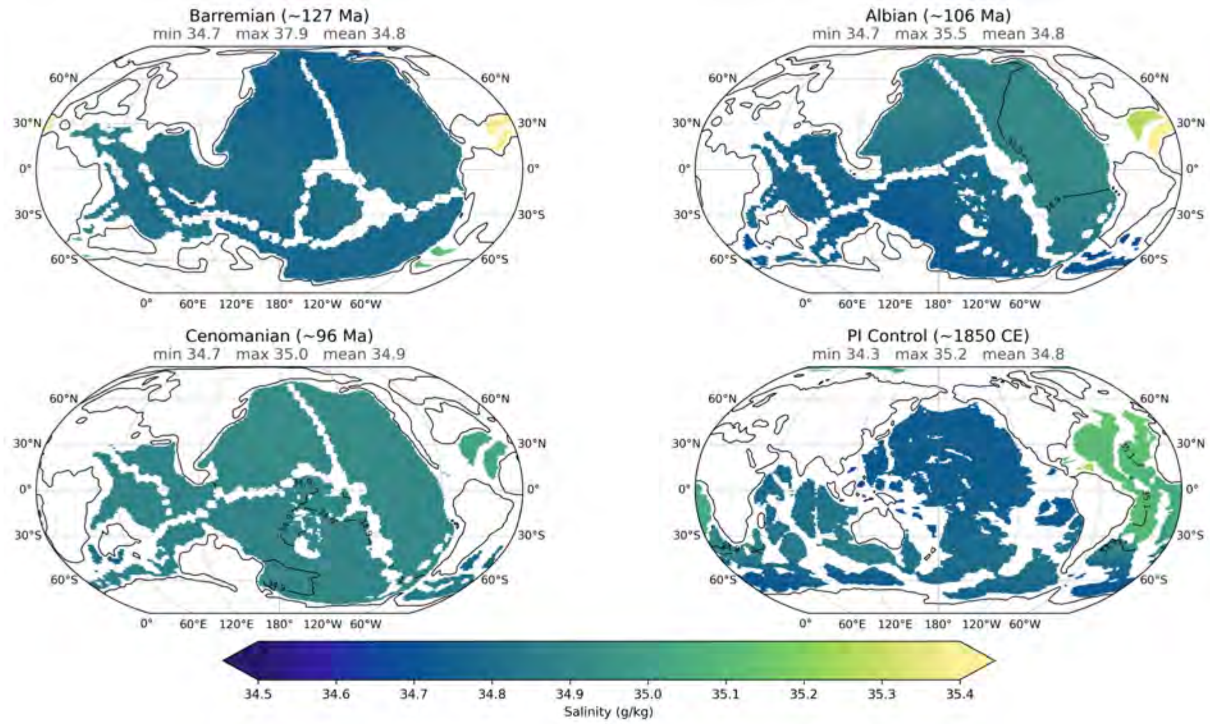

Figure B.11: Simulated oceanic salinity at 4000 metres depth for the Barremian (∼127 Ma), Albian (∼106 Ma), Cenomanian (∼96 Ma) and PI control (1850 CE).

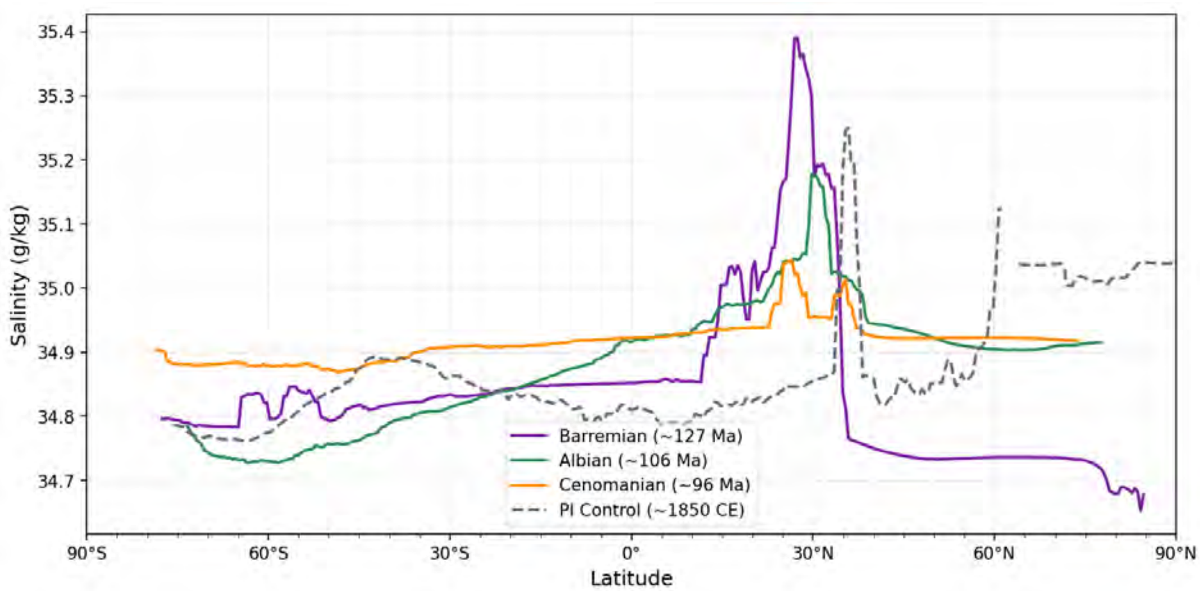

Figure B.12: Simulated oceanic zonal mean salinity at 3000 metres depth for the Barremian (∼127 Ma), Albian (∼106 Ma), Cenomanian (∼96 Ma) and PI control (1850 CE).

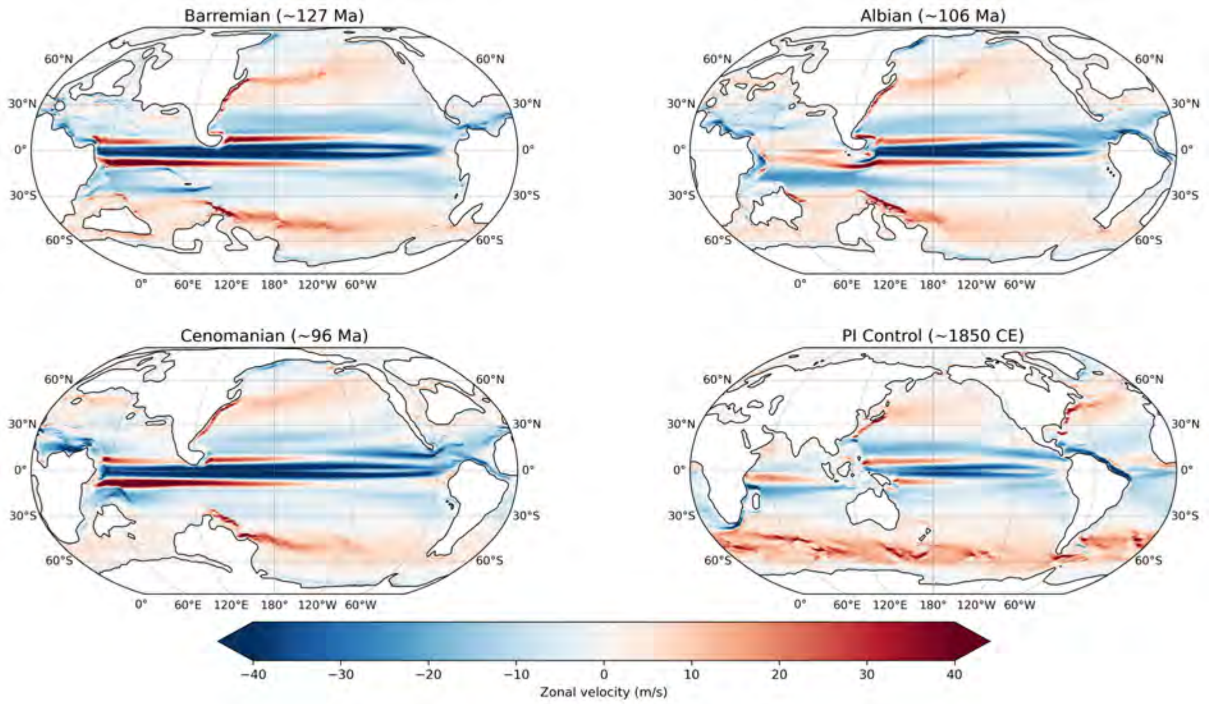

Figure B.13: Simulated oceanic surface zonal velocity for the Barremian (∼127 Ma), Albian (∼106 Ma), Cenomanian (∼96 Ma) and PI control (1850 CE).

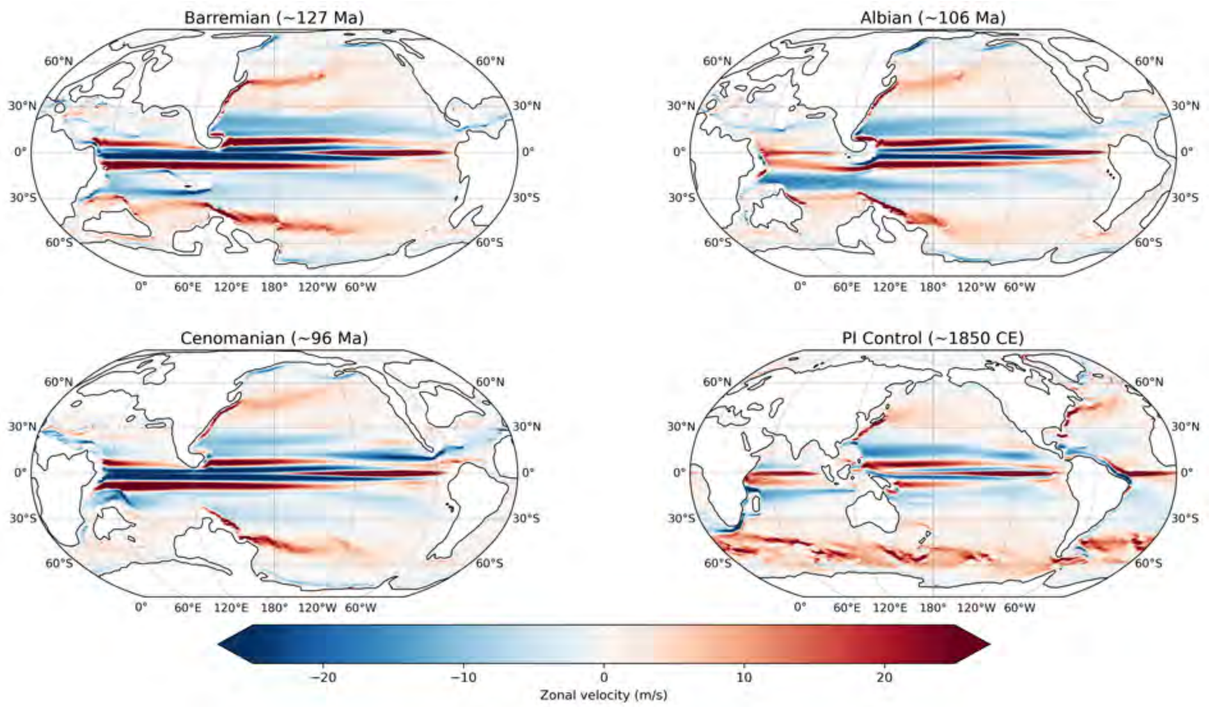

Figure B.14: Simulated oceanic zonal velocity at 100 metres depth for the Barremian (∼127 Ma), Albian (∼106 Ma), Cenomanian (∼96 Ma) and PI control (1850 CE).

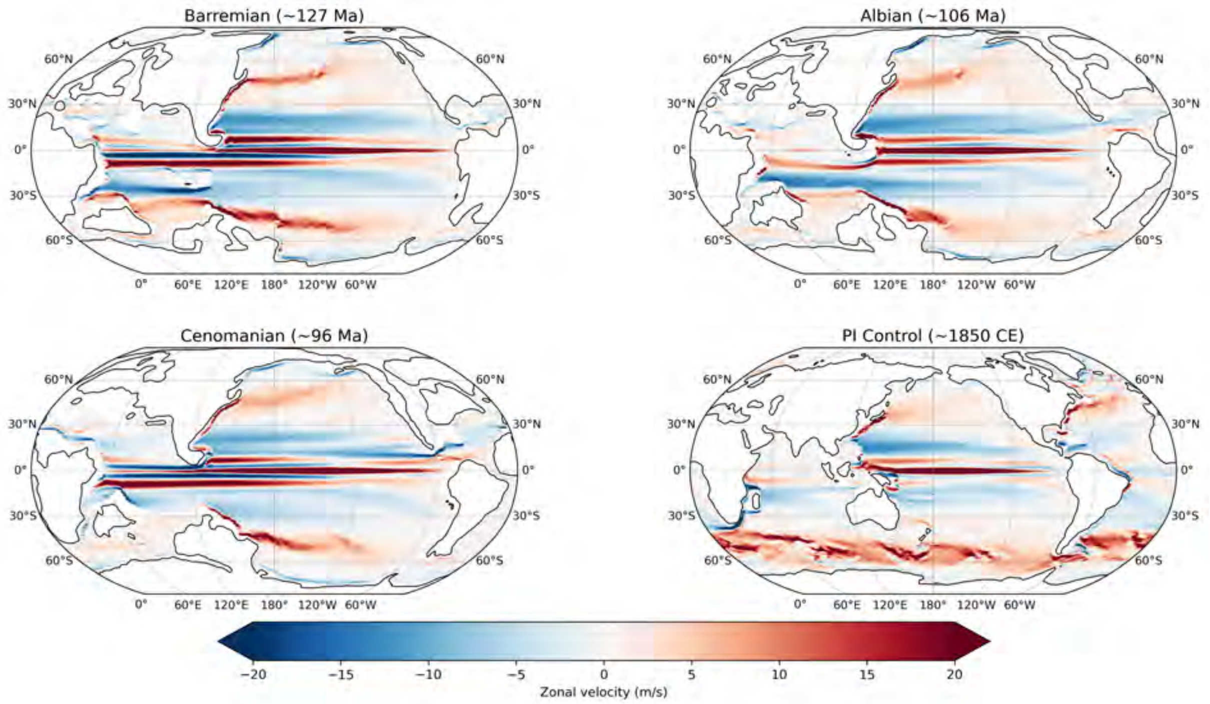

Figure B.15: Simulated oceanic zonal velocity at 200 metres depth for the Barremian (∼127 Ma), Albian (∼106 Ma), Cenomanian (∼96 Ma) and PI control (1850 CE).

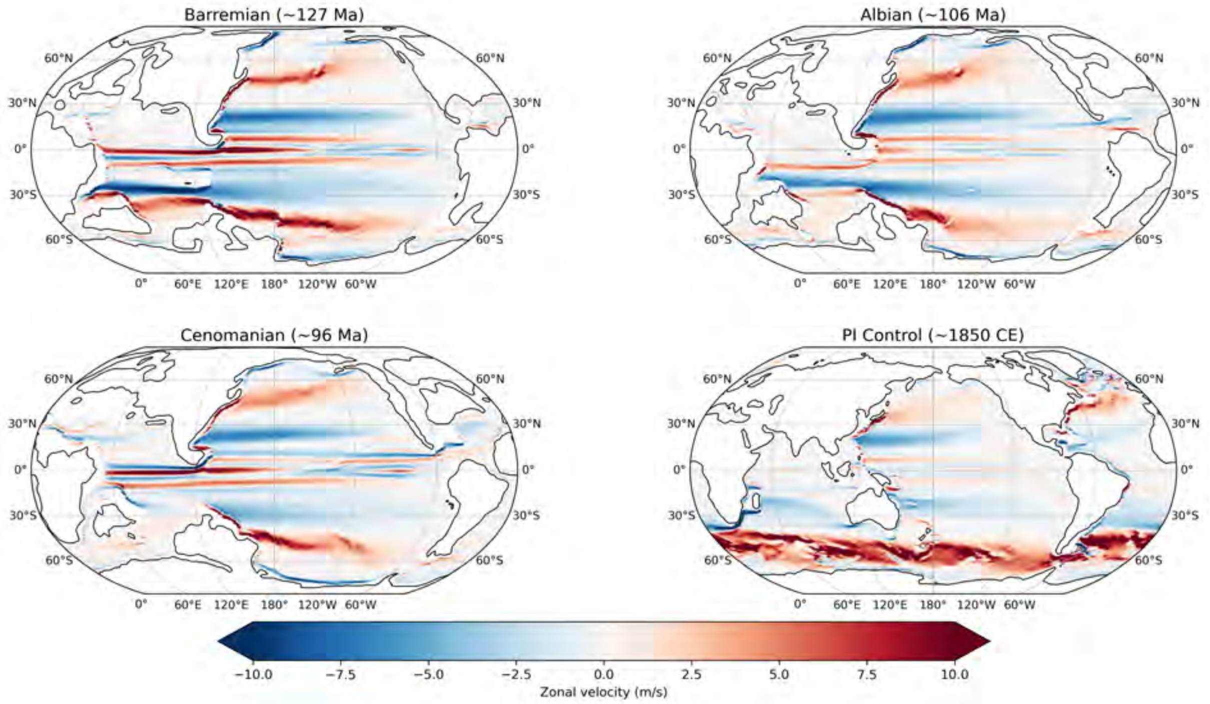

Figure B.16: Simulated oceanic zonal velocity at 500 metres depth for the Barremian (∼127 Ma), Albian (∼106 Ma), Cenomanian (∼96 Ma) and PI control (1850 CE).

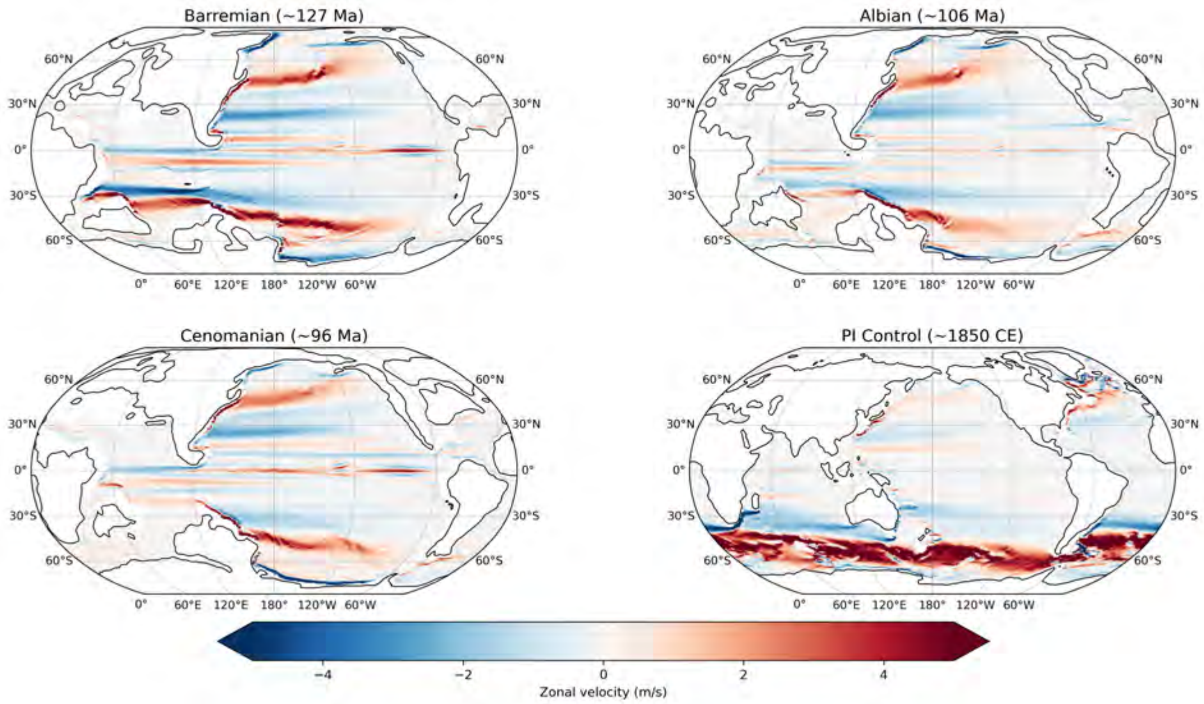

Figure B.17: Simulated oceanic zonal velocity at 1000 metres depth for the Barremian (∼127 Ma), Albian (∼106 Ma), Cenomanian (∼96 Ma) and PI control (1850 CE).

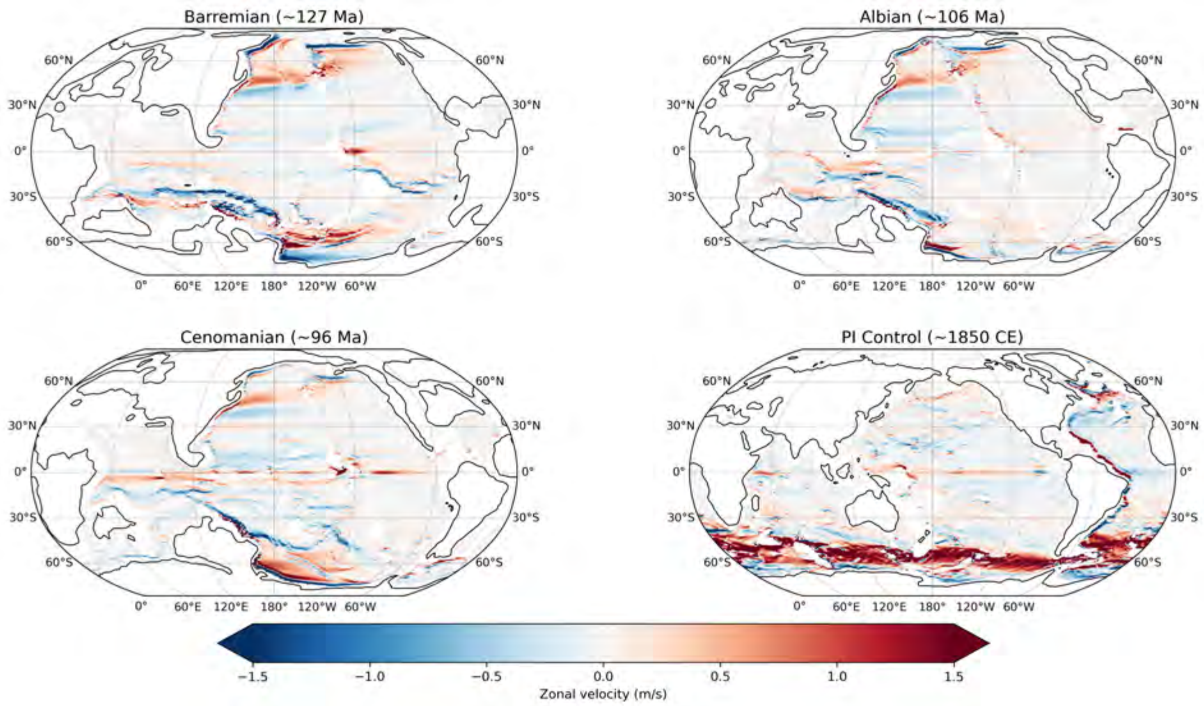

Figure B.18: Simulated oceanic zonal velocity at 3000 metres depth for the Barremian (∼127 Ma), Albian (∼106 Ma), Cenomanian (∼96 Ma) and PI control (1850 CE).

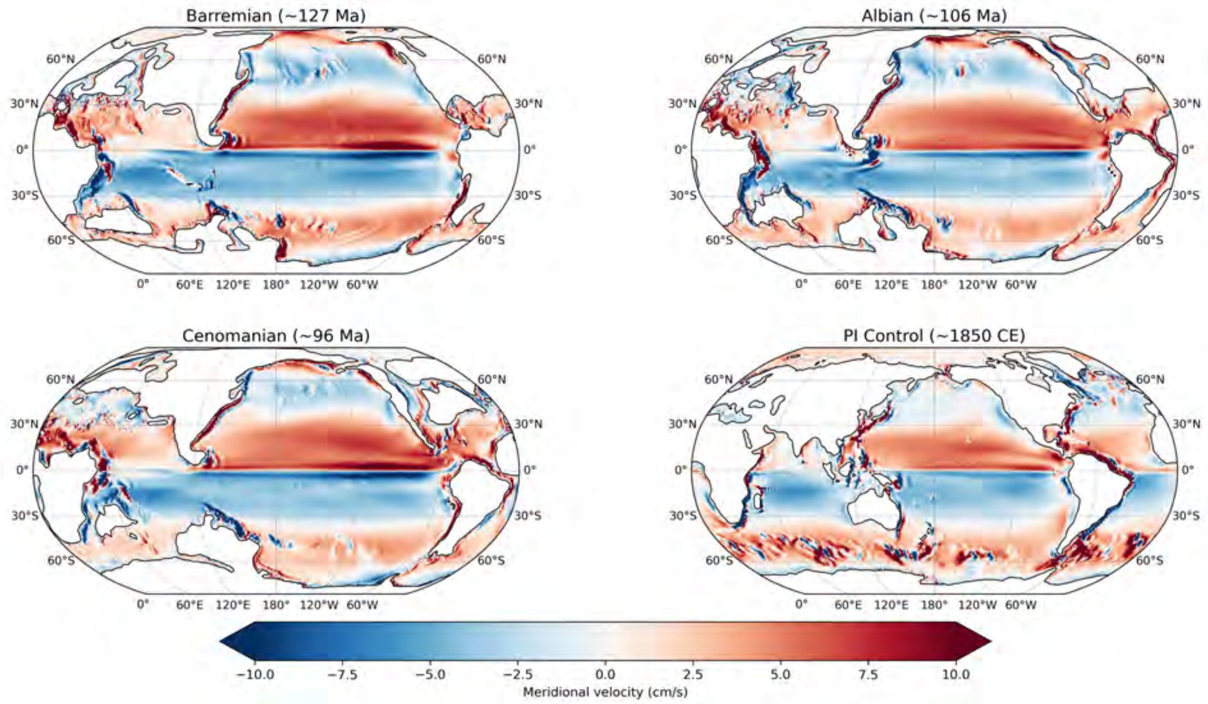

Figure B.19: Simulated oceanic surface meridional velocity for the Barremian (∼127 Ma), Albian (∼106 Ma), Cenomanian (∼96 Ma) and PI control (1850 CE).

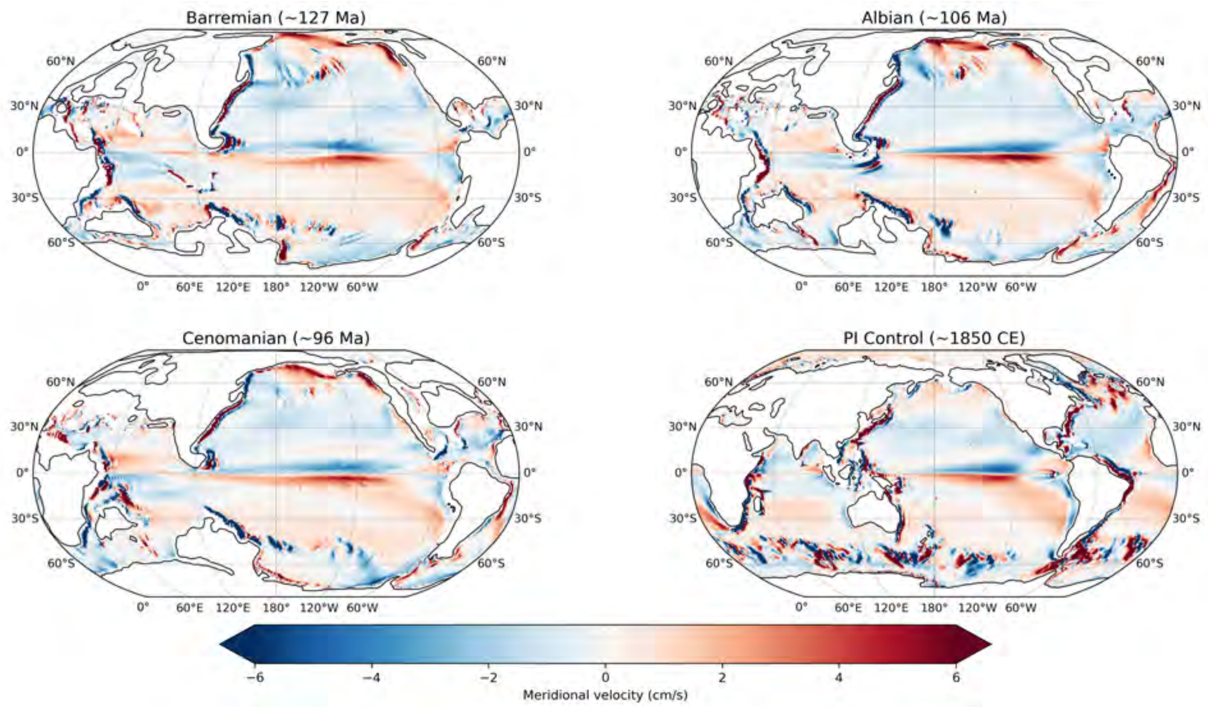

Figure B.20: Simulated oceanic meridional velocity at 100 metres depth for the Barremian (∼127 Ma), Albian (∼106 Ma), Cenomanian (∼96 Ma) and PI control (1850 CE).

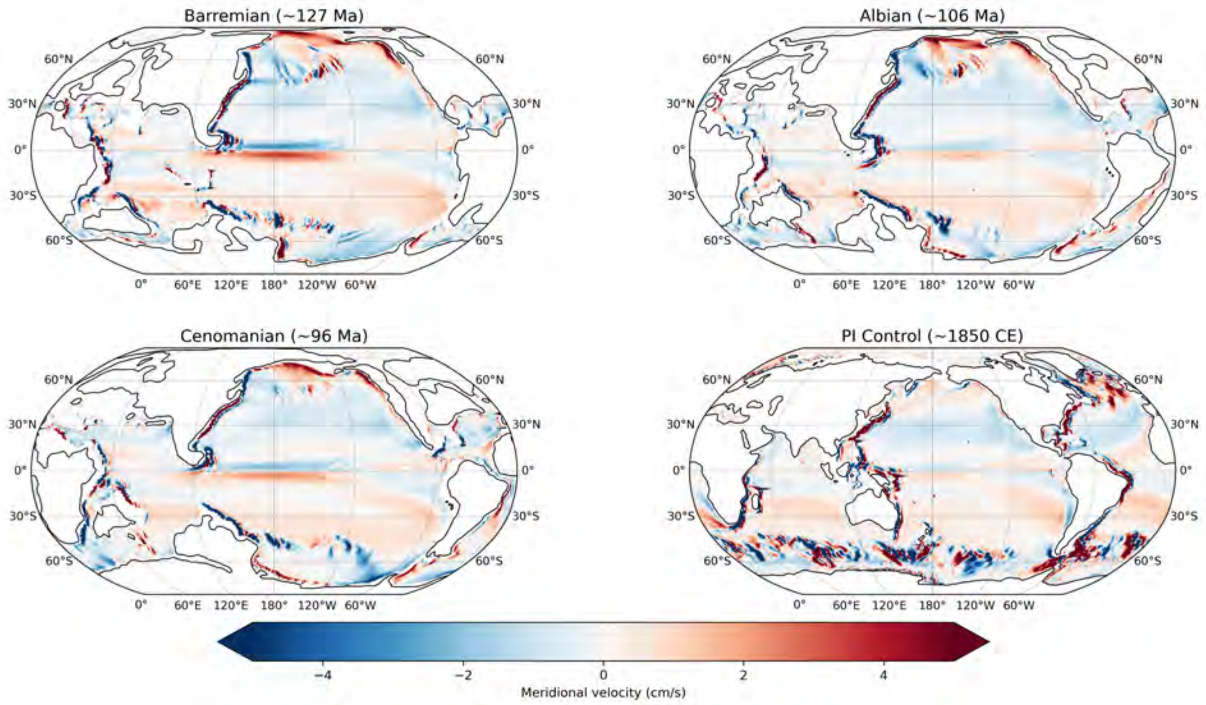

Figure B.21: Simulated oceanic meridional velocity at 200 metres depth for the Barremian (~127 Ma), Albian (~106 Ma), Cenomanian (~96 Ma) and PI control (1850 CE).

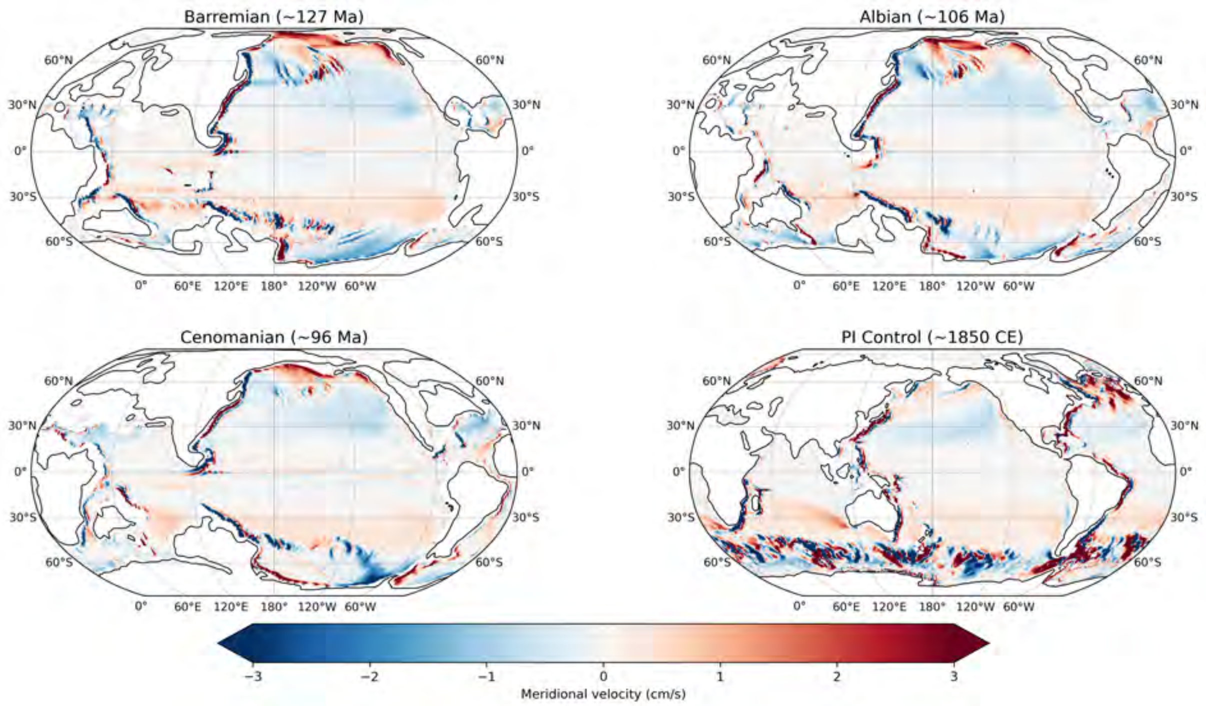

Figure B.22: Simulated oceanic meridional velocity at 500 metres depth for the Barremian (~127 Ma), Albian (~106 Ma), Cenomanian (~96 Ma) and PI control (1850 CE).

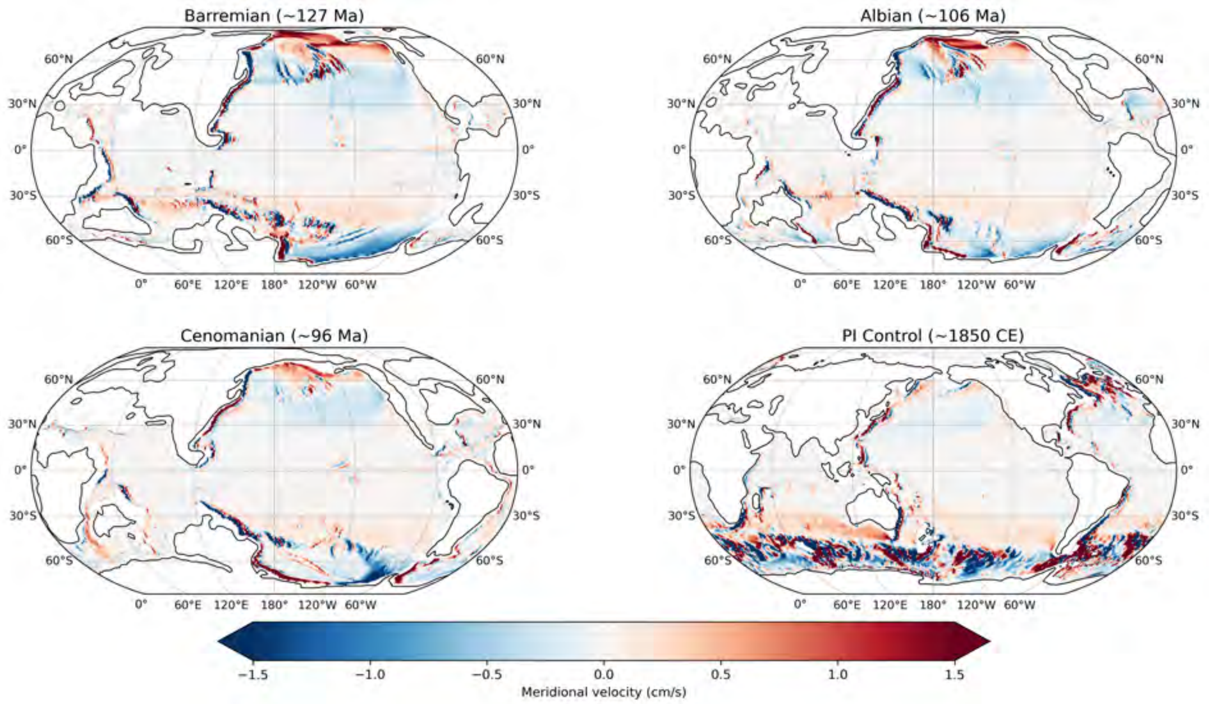

Figure B.23: Simulated oceanic meridional velocity at 1000 metres depth for the Barremian (∼127 Ma), Albian (∼106 Ma), Cenomanian (∼96 Ma) and PI control (1850 CE).

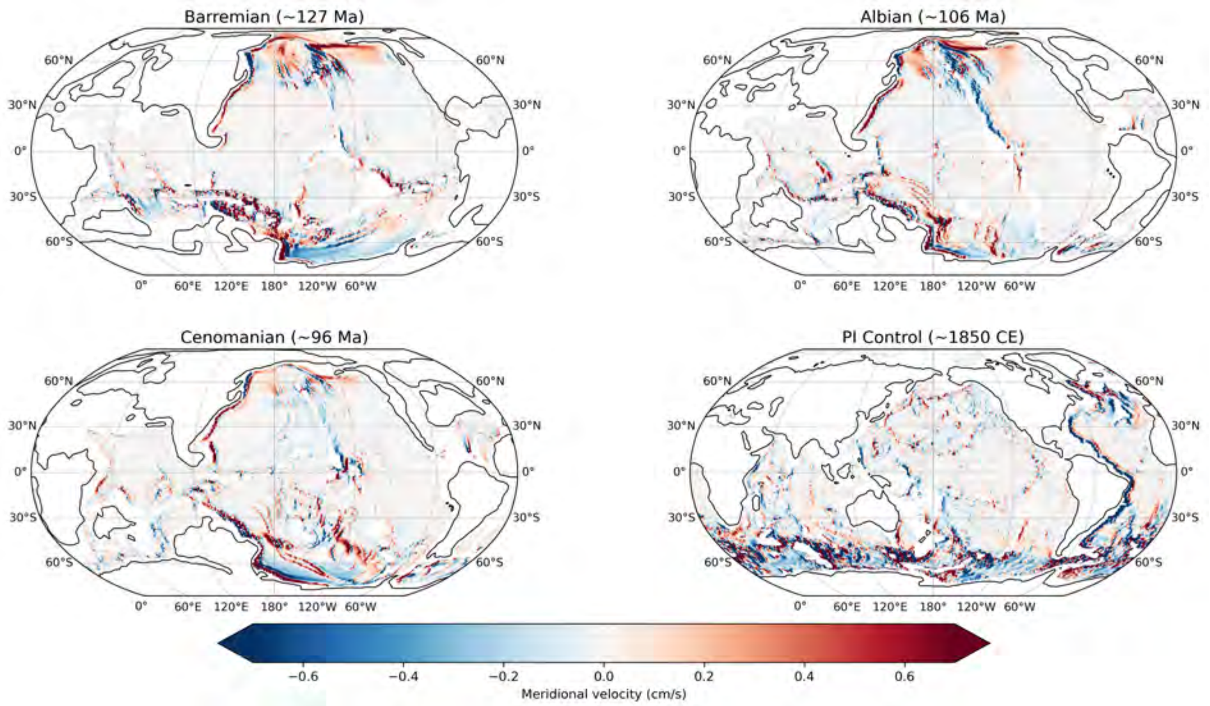

Figure B.24: Simulated oceanic meridional velocity at 3000 metres depth for the Barremian (∼127 Ma), Albian (∼106 Ma), Cenomanian (∼96 Ma) and PI control (1850 CE).

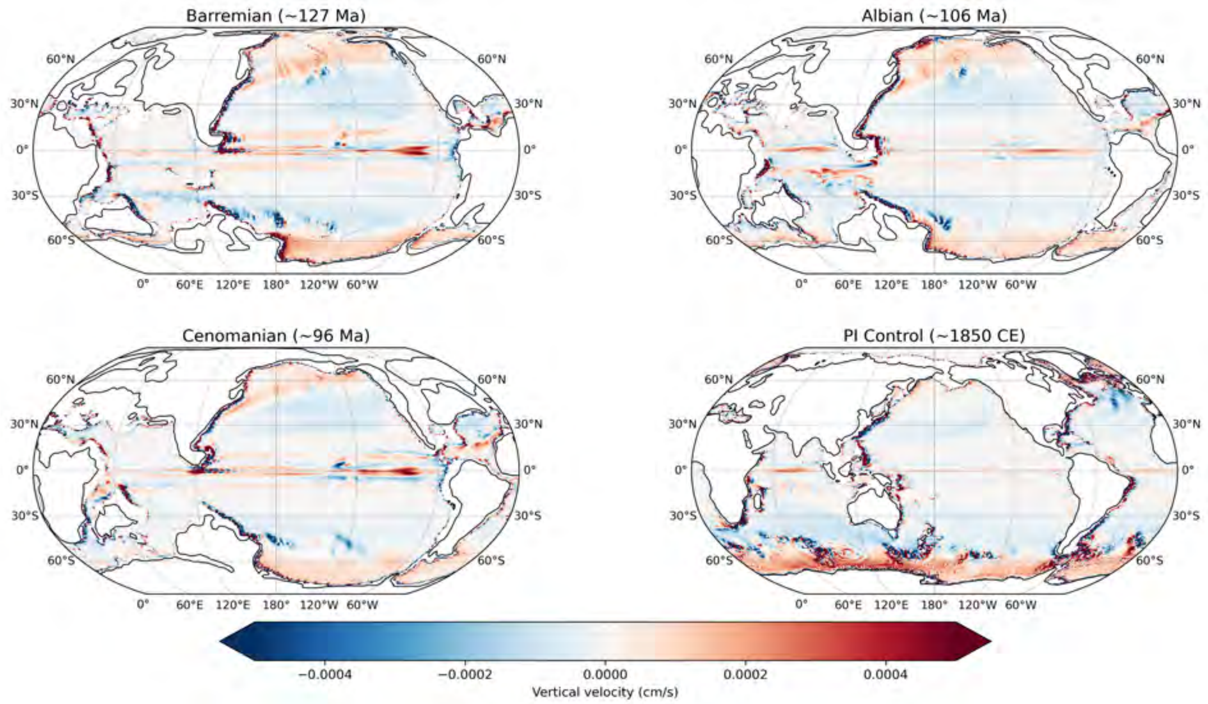

Figure B.25: Simulated oceanic vertical velocity at 500 metres depth for the Barremian (∼127 Ma), Albian (∼106 Ma), Cenomanian (∼96 Ma) and PI control (1850 CE).

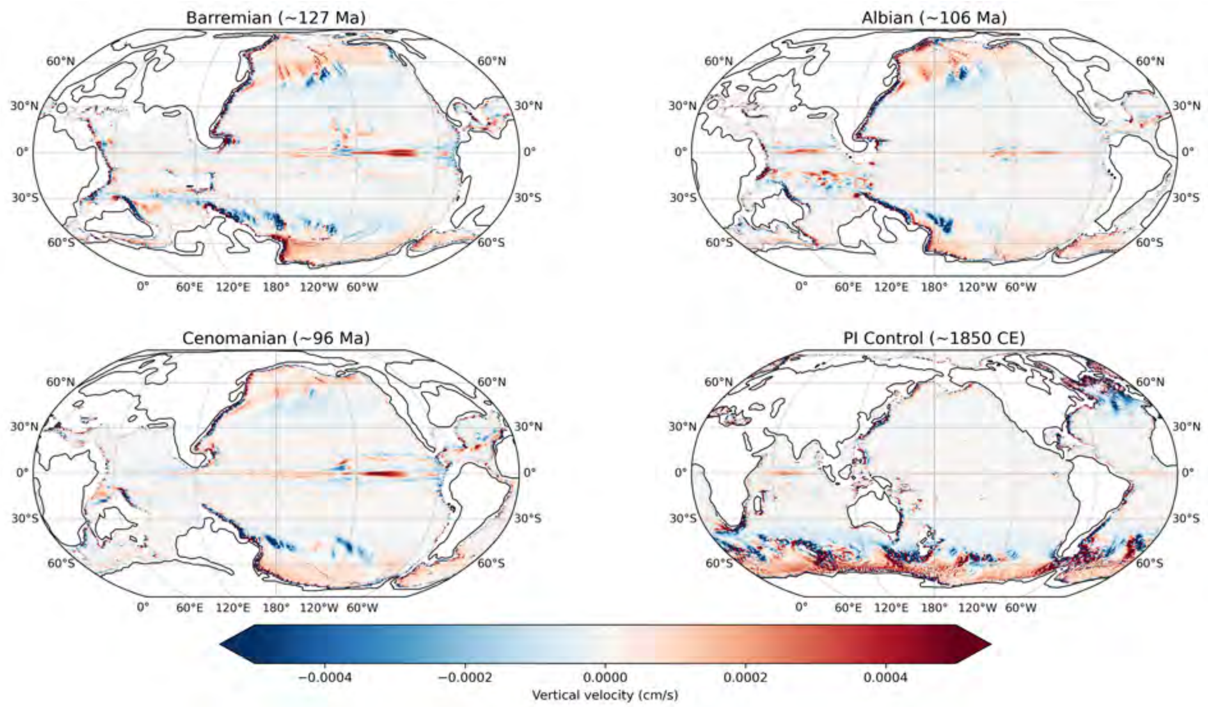

Figure B.26: Simulated oceanic vertical velocity at 1000 metres depth for the Barremian (∼127 Ma), Albian (∼106 Ma), Cenomanian (∼96 Ma) and PI control (1850 CE).

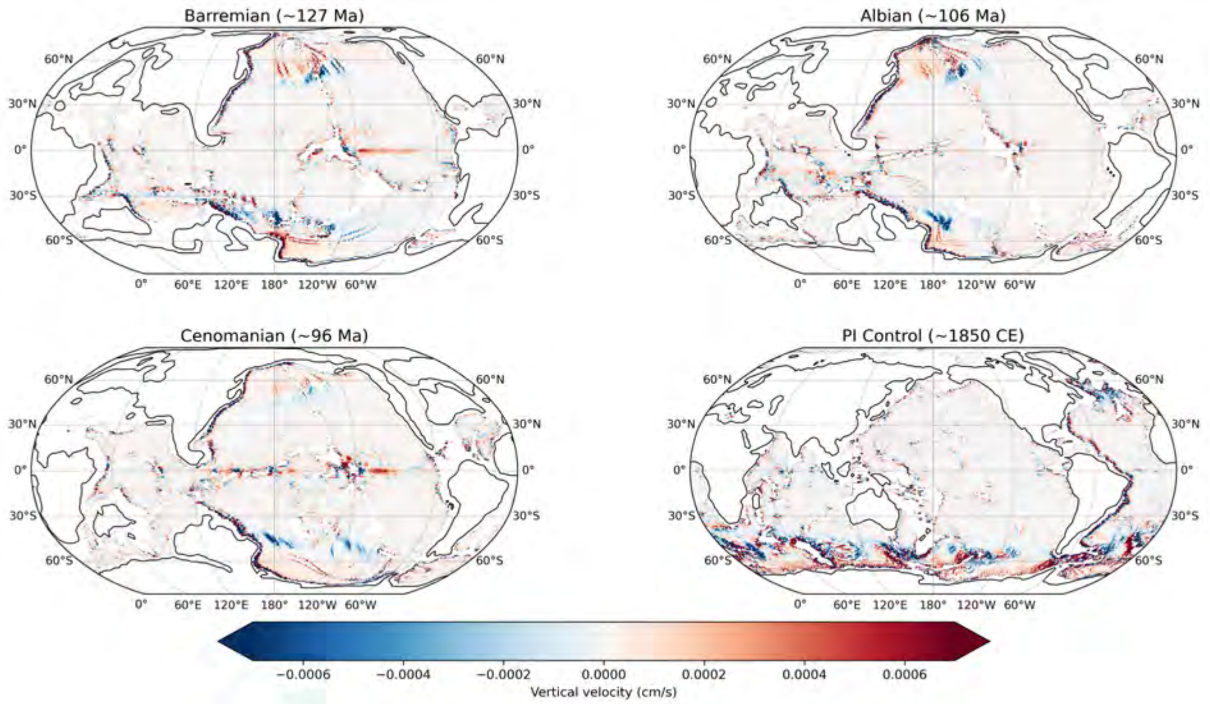

Figure B.27: Simulated oceanic vertical velocity at 3000 metres depth for the Barremian (∼127 Ma), Albian (∼106 Ma), Cenomanian (∼96 Ma) and PI control (1850 CE).

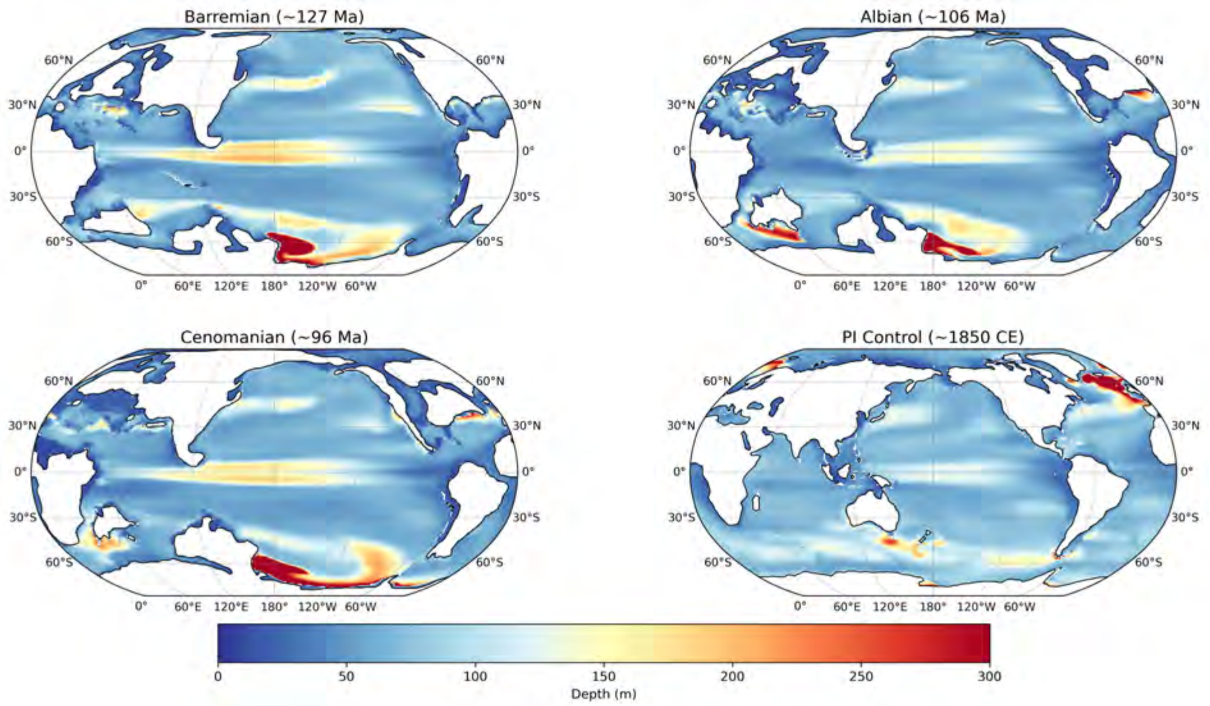

Figure B.28: Simulated oceanic maximum mixed layer depth for the Barremian (∼127 Ma), Albian (∼106 Ma), Cenomanian (∼96 Ma) and PI control (1850 CE).

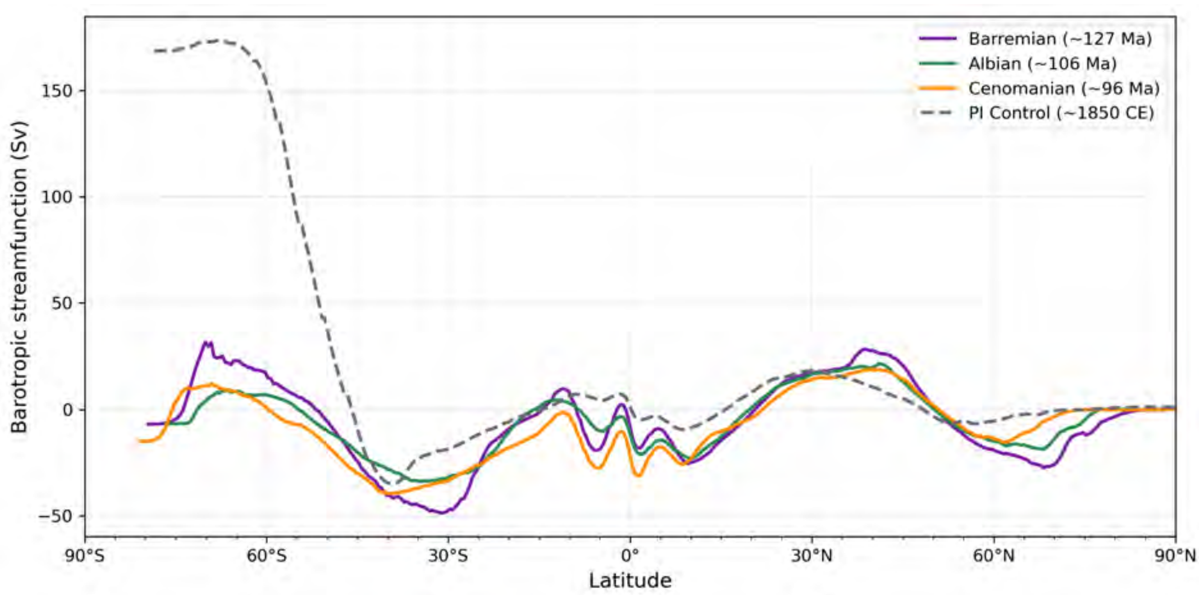

Figure B.29: Simulated oceanic zonal mean barotropic streamfunction for the Barremian (∼127 Ma), Albian (∼106 Ma), Cenomanian (∼96 Ma) and PI control (1850 CE).

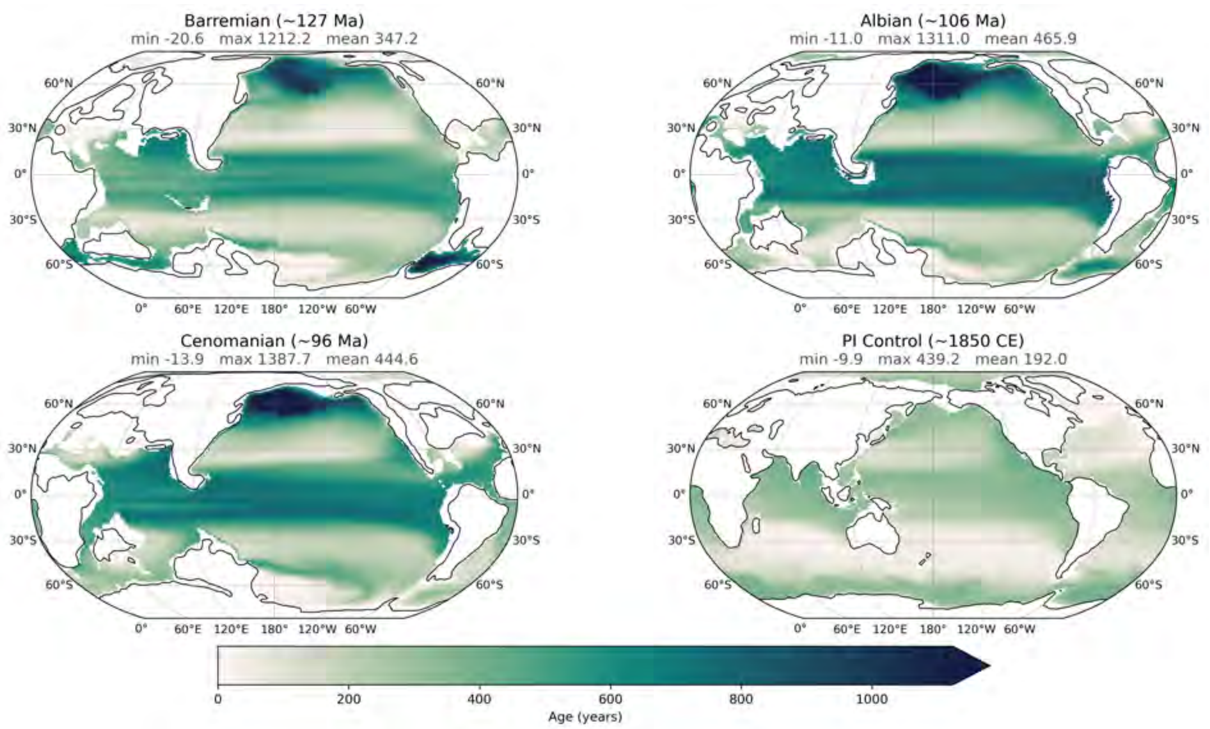

Figure B.30: Simulated oceanic ideal age at 500 metres depth for the Barremian (∼127 Ma), Albian (∼106 Ma), Cenomanian (∼96 Ma) and PI control (1850 CE).

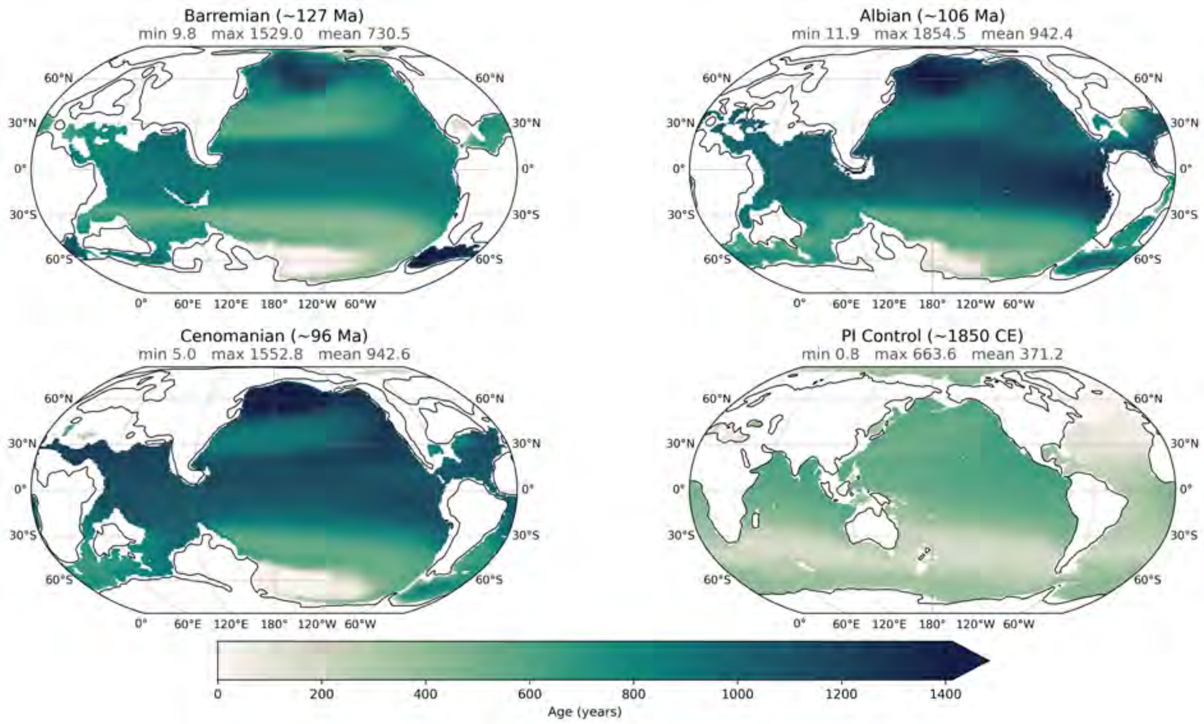

Figure B.31: Simulated oceanic ideal age at 1000 metres depth for the Barremian (∼127 Ma), Albian (∼106 Ma), Cenomanian (∼96 Ma) and PI control (1850 CE).

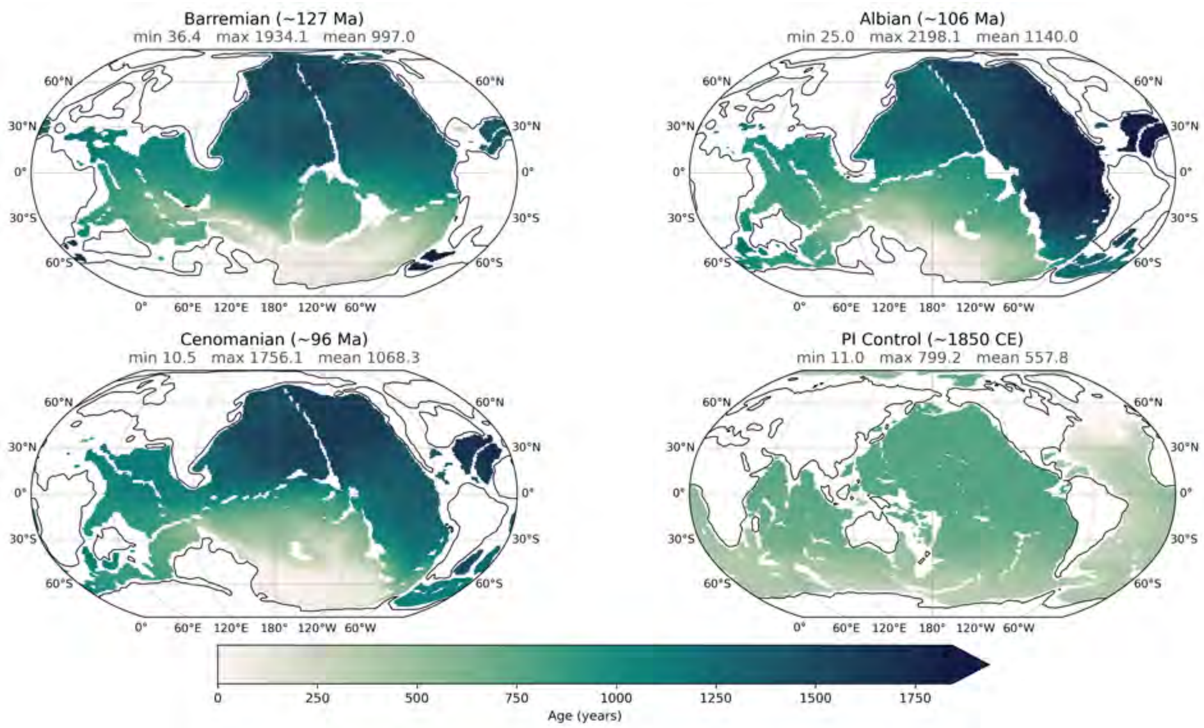

Figure B.32: Simulated oceanic ideal age at 3000 metres depth for the Barremian (∼127 Ma), Albian (∼106 Ma), Cenomanian (∼96 Ma) and PI control (1850 CE).